8-30-2011

Acoustic bandgap sensors for hot-spot damage monitoring

Ryan Schnalzer

Ryan Schnalzer
Candidate

Civil Engineering
Department

This thesis is approved, and it is acceptable in quality and form for publication:

Approved by the Thesis Committee:

Dr. Mahmoud Reda Taha , Chairperson

Dr. Walter Gerstle

Dr. Timothy Ross

Acoustic Bandgap Sensors for Hot-Spot Damage Monitoring

by

Ryan Thomas Schnalzer

B.S., University of New Mexico, 2006

THESIS

Submitted in Partial Fulfillment of the

Requirements for the Degree of

Master of Science

Civil Engineering

The University of New Mexico

Albuquerque, New Mexico

July, 2011

Dedication

To my grandfather whose selfless, warm-hearted character will be ever-present in my life because of the foundation he has provided - and been - for the family based on generosity, kindness, and faith. His sacrifices have allowed me the opportunity of higher education, an opportunity that he did not share. You are my hero and I can only hope to one day be compared to you.

Acknowledgments

Firstly, I would like to thank my advisor Dr. Taha for his support and providing me with the opportunity to advance my education.

I would like to acknowledge my committee for their contributions in time and advice to enhance this work. I would also like to extend this thanks to Dr. Leseman, Dr. El-Kady, and Dr. Olsson for their guidance at the early stages of the project.

Thank you to my fellow students for providing confidence and general help. Each project becomes more of a collaborative effort and is bettered by the culture that has been created by the students. Thank you also to the office staff and faculty for everything that you have helped me with throughout these years.

Finally, thank you to my family who has been there with me patiently through the hard times and always providing me comfort and simple presence. Thank you to my mom, dad, and sisters, aunt uncle, and grandparents for all the little things that allow me to do what I do.

Acoustic Bandgap Sensors for Hot-Spot Damage Monitoring

by

Ryan Thomas Schnalzer

ABSTRACT OF THESIS

Submitted in Partial Fulfillment of the
Requirements for the Degree of

Master of Science
Civil Engineering

The University of New Mexico

Albuquerque, New Mexico

July, 2011

Acoustic Bandgap Sensors for Hot-Spot Damage Monitoring

by

Ryan Thomas Schnalzer

B.S., University of New Mexico, 2006

M.S., Civil Engineering, University of New Mexico, 2011

Abstract

This research presents a novel, mechanically tunable sensor that utilizes the acoustic response of a polymer based acoustic bandgap (ABG) material to identify and quantify damage in material substrates. Acoustic bandgap (ABG) sensors are the mechanical analogues of semi-conductors by which a periodic array of differing acoustic impedances causes an acoustic bandgap. This is comparable to the periodic array of electronic potentials that cause an electronic bandgap in semi-conductors. An ABG sensor is composed of a host matrix material with a periodic array of inclusions/scatterers made of a material with dissimilar acoustic impedance. ABG sensors offer advantages to structural health monitoring (SHM) applications. Such advantages include sensor scalability which enables macro to sub-micron damage detection and the non-intrusive attachment of the sensor to substrates.

The specific use of ABG sensors is proposed for areas of known damage already initiated (hot-spots) in critical components of a structure. This thesis examines the

proposed use of ABG materials as sensors by showing experimentally and analytically how ABG can be used to detect and quantify change in the strain field of the substrate underneath. A parametric experimental study examines specimens composed of two host materials of low and medium elasticity, one viscoelastic and one elastic respectively. Four volume fractions are also considered for both host material types. A finite element simulation is employed to verify the experimental observations of the acoustic bandgap sensors and to demonstrate the functionality of the sensor.

Contents

List of Figures

List of Tables

Glossary

a	Lattice Constant
C_l	Longitudinal Speed of Sound
Z	Acoustic Impedance
FF	Filling Fraction
d	Diameter of Inclusion
ρ	Density
r	Radius of Inclusion
λ	Wavelength
ω	Frequency

Chapter 1

Introduction

1.1 Overview

The purpose of this thesis is to examine the possible application of sensors made of acoustic bandgap materials for hot-spot damage monitoring. This work will address the need for micron and sub-micron scale damage detection in composite structures. This work also demonstrates experimentally and computationally the way in which ABG sensors work. The experiments are performed using twenty-two macrosized ABG material specimens that encompass four geometrical variables and two material property variables. The computational models use the finite element method to illustrate how an ABG is formed and will serve as a guide in determining the existence and frequency of occurrence.

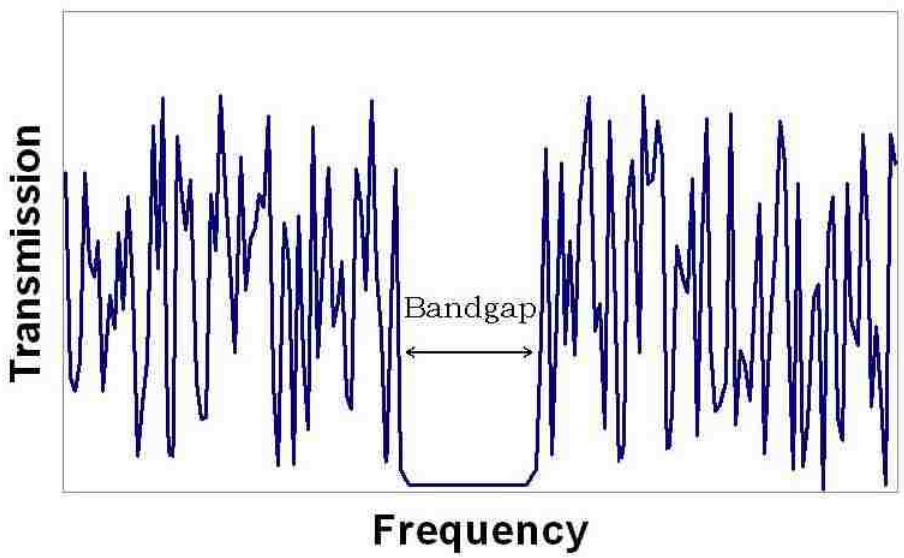

Figure 1.1: Graphic representation of acoustic bandgap phenomenon

1.2 Sensing by ABG

A major aspect of structural health monitoring (SHM) research targets the development of feasible sensing methods to detect damage in structures. This research proposes a new sensing technique to be used for monitoring damage in critical structural materials of known damage in structures utilizing mechanically tunable acoustic bandgap (ABG) materials. Acoustic bandgap is a physical phenomenon that occurs in periodic materials in which acoustic waves are prohibited from propagating in the material within a range of frequencies as illustrated in Figure 1.1. A 'gap' of transmission is present in the frequency domain. The premise of ABG sensors is to exploit the this acoustic bandgap to be used as a damage feature that can be related to damage type and severity.

ABG materials can be micro-manufactured by placement of a periodic array of scatterers/inclusions in a host matrix material. The scatterer material shall have highly mismatched acoustic impedance compared with the matrix material. Acoustic

impedance, Z, is summarized in Equation 1.1 where ρ is the density and C_l is the longitudinal wave speed in a material.

$$Z = \rho C_l \tag{1.1}$$

The inclusions form a lattice or a crystal-like structure. A schematic representation of the proposed ABG sensor is shown in Figure 1.2. It is the differing impedance between the host material and the scatterers under the specified geometrical constraints that enables the creation of the bandgap through losses such as reflection.

An ABG sensor differs from many other sensing devices in that the acoustic signal does not travel through the substrate material where damage is present, but through the sensor itself. The concept of operation entails sending an acoustic pulse through one side of the sensor and receiving the pulse on the other side. The respective bandgap that occurs can therefore act as a damage feature which is indicative of healthy or damaged behavior due to the condition of the substrate with which the sensor is adhered. If a local damage underneath the sensor takes place, it is inferred that the sensor will observe such strain and thus cause a change in the highly functional periodicity of the structure. Due to the scalable quality of this phononic occurrence with the periodic spacing, ABG sensing has great potential for very high sensitivity with low periodic spacing dimensions. The sensitivity is therefore currently limited only by manufacturing constraints. In addition, changes in the periodicity of the sensor are directly correlated with the damage size in the substrate material; accordingly strain values in the substrate translate to amplified strain values in the sensor due to the relative nature of strain with respect to total dimension.

strain occurrences within the sensor are an amplified value of the true strain of the substrate under testing since strain is a normalized quantity with respect to the dimensions of the structure undergoing strain. So the sensitivity level capabilities

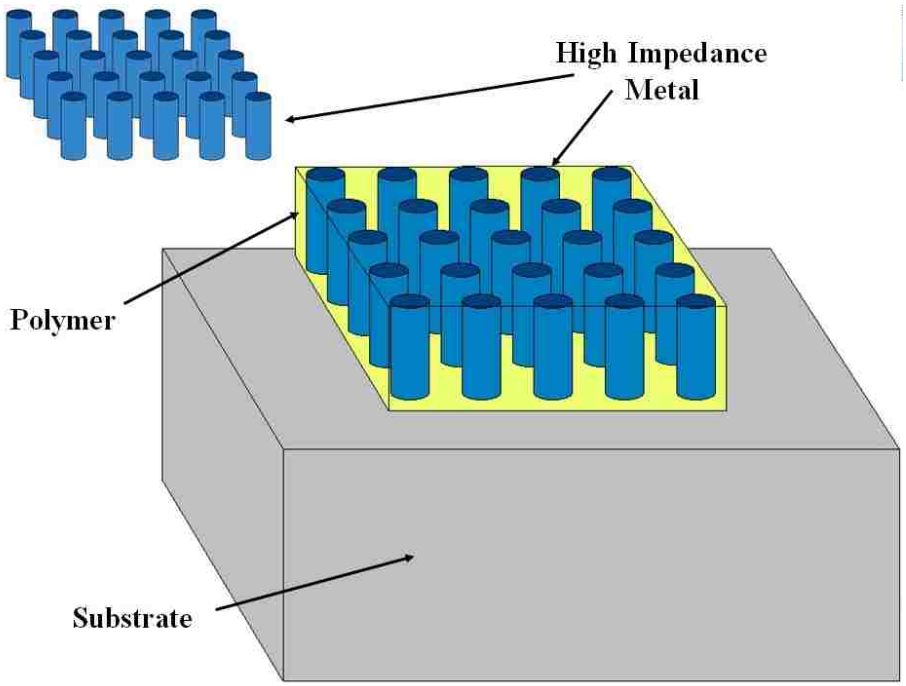

Figure 1.2: 3D Schematic representation of an ABG sensor

are amplified.

This thesis will examine the feasibility of using an ABG sensor to detect damage in a substrate adhered to the ABG sensor. It is considered that localized damage below the sensor, such as cracking or plastic strain in the substrate, will cause change in dimensions on the substrate surface, consequently affecting the less-stiff ABG sensor that is adhered to the deforming substrate. The resulting change in dimensions of the sensor causes irregular spacing in the highly critical periodicity of the sensor, instigating a change in the periodicity within a region of the sensor. The received signal will thereby represent this effect due to a change in behavior of the bandgap.

Traditional sensor outputs can sometimes present false positives, or assign readings of damage due to effects from different occurrences that offset the damage feature. Incidents that may incur false positives in ABG such as environmental effects

shall be considered and addressed. Such instances as temperature and humidity changes will produce a global change on the substrate allowing for a simple expansion or contraction of the sensor, leaving the periodicity consistent, but with greater spacings. Based on the concepts stated above, the methods outlined in this thesis will show the manner in which ABG sensors accomplish damage detection by first engineering a bandgap (demonstrating knowledge of bandgap occurrence by analytical and experimental matching). In addition, substrate damage is shown by the deterioration of the bandgap and uniform strains due to environmental (non-damaged) effects are demonstrated through a bandgap profile shift.

1.3 Motivation

Both commercial and military applications are influencing the need for structural health monitoring with most emphasis in composite structures. A desired movement from Time Based Maintenance (TBM) to Condition Based Maintenance (CBM) will enhance the efficiency of use throughout the lifespan of a structure [1]. The largest impact that SHM may have on composite structures may be in the aerospace industry. It is shown that fiber reinforced polymer composites are increasingly being used in aircraft structures. In addition, aging aircraft consisting of composite materials are producing rising costs in support, especially in the Department of Defense [1]. Current methodology in TBM requires inspection periods that result in wastes of time and money. Inspections can often be complex for the human examiner and it has consequently been estimated that fifteen percent of all aircraft accidents are due to human error during maintenance activity [2]. Many times this may be due to barely visible impact damage (BVID) or damage with no visible indication at all such as delaminations [3]. These problems are currently being addressed by research. Critical infrastructure and high value assets are moving towards becoming "smart"

or "intelligent" structures by implementing SHM systems so maintenance costs will no longer be wasted on inaccurate, time-based procedures. Instead, with the help of sensors, SHM will provide structures capable of monitoring themselves much in a way 'analogous to medical science' [2].

ABG sensors have a specific place in the realm of SHM. Structural health monitoring can be broken down into two categories of sensing abilities consisting of 1) Global Sensing and 2) Localized Sensing. Both components of SHM have different purposes and challenges, but have potential to work together in a system to monitor the structure as a whole. Specifically, localized sensors must achieve sensitivity to damage relative to the need, which can at times current technology cannot yet meet. In addition, the sensors must be able to differentiate actual damage from simple environmental effects due to fluctuating temperature or humidity. This thesis illustrates the potential of using ABG material sensors with high sensitivity and capability to differentiate between damage and other effects.

1.4 Structure of Thesis

The following chapters of this thesis are divided as follows: Chapter 2 covers literature pertaining to this project by first overviewing SHM, further detailing the need for SHM, and outlining current sensing techniques available for structures highlighting specifically composites in the aerospace industry. The second section of Chapter 2 will cover the state of the art on ABG materials addressing both the analytical and experimental research investigations.

Chapter 3 outlines the experimental methods performed consisting of the fabrication process for the ABG specimens and description of the experimental setup and testing methods. The last portion of Chapter 3 includes the experimental results and discussion. Chapter 4 goes over the analytical models that are used to simulate

ABG sensors. The results of the analytical methods are also found in Chapter 4 along with a discussion. Chapter 5 concludes the thesis with a summary of findings and how the results support the goals of this research.

Chapter 2

Literature Review

2.1 Structural Health Monitoring

Structural health monitoring is defined as the scientific process of nondestructively determining the fitness of an engineered component or system during operation by identifying the mechanical damage, the severity level of that damage as the component or system operates and the future performance of the component or system as damage accumulates. The components of SHM work together as a system in engineered structures much like a visit to the doctor's office. The pain or irregularity that is relayed to the doctor can be compared to recognition of damage occurrence. Recognition of damage in SHM, like pain indicated by the human nervous system (Fig 2.1), is obtained through various methods through the use of a damage feature, which will be described in more detail later in this chapter. Questions by the doctor about the patient's recent conditions and worsening of the pain is much like the process of diagnosis and prognosis. As structures gain 'intelligence', making the move to 'smart structures', the future of engineering will parallel medical science more than traditional engineering [2]. For this reason, there is an increasing amount of

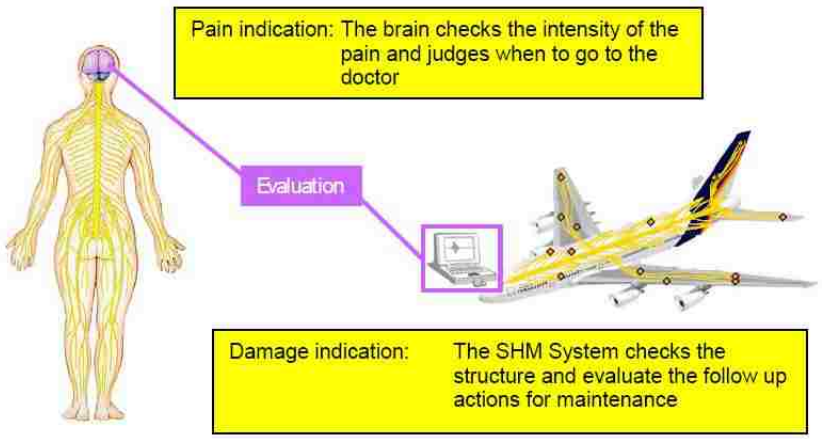

Figure 2.1: Linking nervous system to SHM [4]

research in this area to enhance monitoring ability and monitoring reliability in the preparation of a comfortable transition to smart structures.

2.1.1 Background

Structural health monitoring encompasses two components, diagnosis and prognosis, for in-service conditioning of structural components and systems. SHM differs from the well known process of nondestructive evaluation (NDE), which offers only the diagnosis element. Diagnosis for NDE is performed during off-line inspection in a practice called nondestructive testing (NDT), a subpart of NDE [5]. NDT is employed to determine damage or condition through nondestructive investigations such as Eddy current testing (ECT), an electromagnetic testing (ET) method or ultrasonic testing (UT) for example. Figure 2.2 represents the interaction between diagnosis and prognosis as a system that works together without the dependence of human interaction for complete systematic health monitoring. Smart sensing technologies can inform the system of irregularity to form a diagnosis. With knowledge based on material characterization and structural damage modeling of the compo-

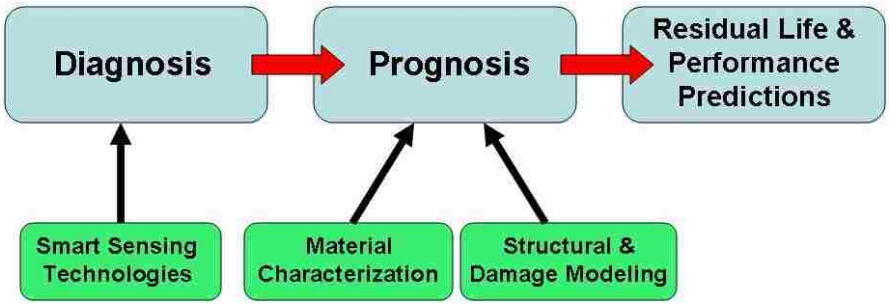

Figure 2.2: SHM process [2]

nents in question, the system can provide a prognosis to enhance the current state of the structural component and form predictions for the residual life. Smart materials, materials aware of their respective health, have thus thrived in research and were readily welcomed in the civil and aerospace industries [5]. In an introduction to the book Structural Health Monitoring, Balageas [5] outlines the benefits of SHM by:

I. Allowing for the efficient use of the structure through the minimization of downtime and the avoidance of catastrophic failures
II. Giving insight for improvements to the designer/constructor
III. Inducing drastic changes for the organization of maintenance services by aiming to replace scheduled maintenance activities by performance-based (PBM) or condition-based maintenance (CBM) and reducing maintenance labor mainly through avoidance of dismounting parts with no hidden defects. SHM also will help to reduce human involvement, labor, downtime, and human error thus improving safety and reliability

Structural health monitoring has shown great progress within the last decade with respect to the detection of damage in materials [6]. Traditionally, acoustic technology was highly used in NDE, dating back a half-century [7]. Before this, NDE was mainly limited to simple visual inspection to identify damage in large structures. SHM has, since its existence, had to deal with the complex challenge of finding a

way to combine global and local sensing techniques through inference of a damage feature [8]. Since damage cannot directly be measured, it is thus deduced through the use of damage features [8]. Damage features are physical indications that lead to measurable quantities to describe damage. Several techniques for detecting damage in materials have been addressed in a great deal of research such as acoustic emission (AE), optical fibers, the use of piezoelectrics, ultrasonic methods, Eddy currents, Lamb waves and several others [9], [1], [10]. The damage feature in Lamb wave detection, for example, are anomalies in the wave response signal at the detection point which can be quantified with complex algorithms to represent damage.

Although there are great challenges and complexities to overcome, SHM has received a great amount of attention over the last two decades due to demand from industry and tremendous interest from the scientific community. The first International Workshop on Structural Health Monitoring was held at Stanford, CA, USA in 1997 with 60 presenters from all over the world. This workshop was put on again in 1999 due to overwhelming recommendation from the research community and has been a yearly event since gaining more and more interest [11]. The heightened attention in this field has sparked tremendous leaps in the technological advancements in smart software, sensing and actuating, materials, computation, and signal processing relating to SHM [12], [6].

2.1.2 Structural Need for SHM

Engineering industry has a definite role for SHM once it has achieved maturity by overcoming challenges such as reliability and robustness. The aviation industry, for example, has justifiably had an interest in continuously monitoring the health of aircraft systems for identification of potential problems before they occur [13]. Goals to decrease maintenance costs in the aerospace industry aim to incorporate suit-

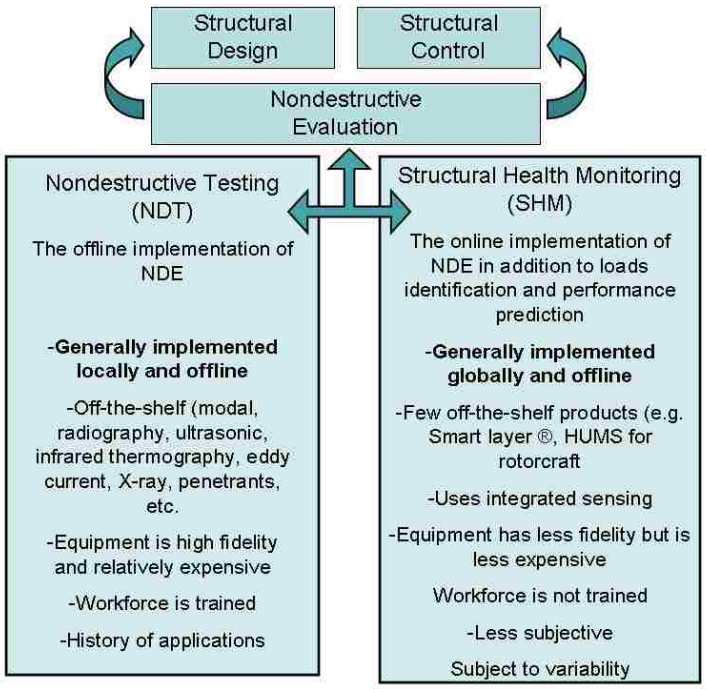

Figure 2.3: SHM and NDT working for efficiency [1]

able SHM technologies. Challenges then surface to obtain durable and reliable NDT methods for in-service operation [4]. Current practices for monitoring structural health in aerospace structures are time-based. Components of aircraft are evaluated using non-destructive testing (NDT) techniques every inspection period as dictated by the governing bodies such as the Federal Aviation Administration (FAA) or the Joint Airworthiness Authority (JAA) [2] [13]. For example, the F-16 requires 25 hours of maintenance per flight hour [1]. In CBM, health monitoring technologies determine when service or maintenance is needed based on the known condition of the structural component in question [1]. This process will eliminate unnecessary inspection intervals from TBM as well as indicate when service or maintenance is necessary, which could fall between inspection intervals with TBM, making the overall process more efficient and effective. Comparison of NDT vs. SHM is presented in Figure 2.3.

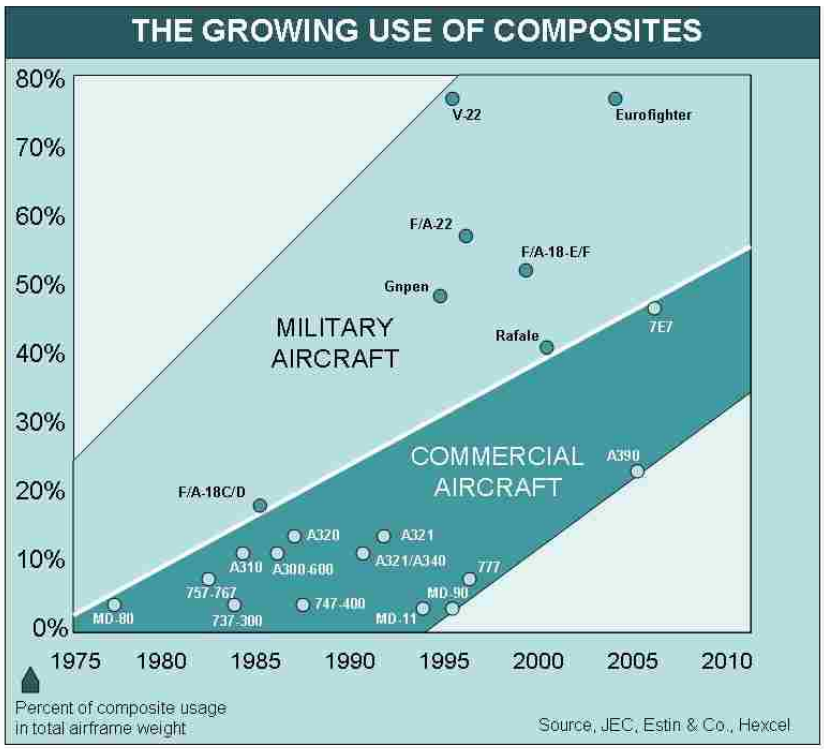

Figure 2.4: A pictorial summary showing the growing use of composites in major aircraft (JEC, Estin & Co, Hexcel)

2.1.3 SHM in Composite Materials

A composite material is made up of two or more composite or homogeneous materials that result in a material which possess unique properties dependent on the geometrical design and individual properties of the constituent materials. Examples include structural composites consisting of laminar composites and sandwich panels, fiber reinforced polymer (FRP) composites, and particulate composites [14]. Composites have been in development and operation in the military for about fifty years. The transition from metals to composites that is currently being seen is similar to the conversion from wood to metal in the 1920's [15].

SHM will be essential to ensuring the safety of the composite structures due to

changes such as:

1) The building of composite structures on a greater scale

2) The building of composite structures through relatively new, automated techniques rather than time-tested traditional methods by hand

3) The fact that inspection and maintenance requirements will be driven by different types of failure than what it is currently for metals (fatigue and corrosion performance)

Techniques and requirements for metals are based on centuries of experience, development, and operation and are therefore well accepted and understood. Certification requirements by the FAA and JAA take a different approach as composites prove to be more complex and less understood. Although composites offer higher specific strength and stiffness, they are regulated to a higher degree than metals usually designed to about 33% of the failure load compared to 60% for metals [2]. In addition, design with composites is not governed by fatigue and corrosion, making composites more desirable for use [15].

Composite materials are increasingly being used in aircraft structures [1] [2] as shown in Figure 2.4. Currently fiber-reinforced polymer composites account for 25% of the structural weight of Airbus 787 and 50% of the structural weight of a Boeing 747 Dreamliner, which had already moved up from 17% composite composition in the past Boeing 747 model [2]. Increase for demand in SHM in composite materials is further amplified by the fact that aging aircraft composed of composites are experiencing rising costs due to support and maintenance.

The steps toward composite failure are outlined by Baker [16]. The process begins with matrix cracking in transversely loaded plies, followed by matrix cracking in axial plies, local delamination at intersection of cracks, and ending with fiber breakage. Research has shown a possibility of "pre-crack fatigue failure" to occur before the

visible steps listed by Atodaria [17]. Detection of damage at the early stages like that of pre-crack fatigue occurring at the microscale can offer benefits to industry using composite structures through early alarms of possible catastrophic failure in critical areas for safety, alerts for maintenance necessity that can contribute to lifespan, and also to signal design flaws for enhancement of better future designs. It has been stated also that bonded repairs with composite patches in aircraft structures are becoming a preferred technique in the repair of localized damage [13]. Such patches offer minimal changes in contours, low weight expense, low cost, easy conformability, and retard crack growth. Patches also require maintenance and may be another critical area in need of monitoring.

2.1.4 Other Sensing Methods for SHM

Damage identification in large structures is mainly made up of vibration-based techniques where vibration signals identify anomalies in a system [18]. The identification of damage in these contexts can be quite complex; much work has been done to extract these damage features in frequency, time, and other domains. The current NDE industry consists greatly of ultrasonic technologies for damage identification [19]. Ultrasonic techniques are common in the aerospace industry due to the gravity of composites used, but have also been used in checking weld quality in steel structures [7]. This technique broadly consists of an acoustic signal being sent through a system to be received at other points throughout the system in order to sense irregularities. One version of this is C-scans, where surface measurements of sound intensity are taken [10].

Other acoustic methods in damage identification include AE sensors in which damage is detected by the acoustic signal that is produced upon the energy release from fracture [20]. In the case of AE, the sensitivity to energy is proportional to

the scale of damage. Due to low amounts of energy release, AE can encounter limitations in terms of its sensitivity resolution. In addition, AE surface techniques used for composite materials require a great deal of complex signal analysis and result in high uncertainty in terms of damage location and severity [21]. However, researchers have now shown how AE and piezoelectric sensors can be integrated into a network to identify damage locations [22]. Fiber optical and piezoelectric sensors have also been proposed to be sensitive to AE [23]. Networks of fiber optic sensors and piezoelectric sensors have also been considered in the literature to detect damage through embedment of the sensors in the surface or mounting the sensors onto the surface of the substrate [9]. Advances in micro-fabrication have paved the way for more sensitive devices due to less restriction in component sizes [24]. Micro-electro-mechanical systems (MEMS) and nano-electro-mechanical systems (NEMS) now show capability of creating devices in the nanometer range. More promising is the fact that Raleigh, shear, and lamb waves have recently been proposed to be more successful in damage detection than the previously mentioned sensing techniques [25].

An in-depth overview of sensing techniques up to the year 2002 is reviewed in the dissertation by Kessler [9]. A summary of limitations, strengths, and potential in the SHM realm of sensing methods is highlighted in Table 2.1 listing techniques as trivial as visual inspection to complex methods such as AE. Useful attributes of each sensing type is evaluated in terms of weight, conformability, portability, size, complexity, expense, sensing area, power draw, and other important qualities. The capabilities of each sensor type are shown in terms of sensor size (Fig 2.5) and sensor power draw (Fig 2.6) as of 2002.

Table 2.1: A comparative summary of strengths, limitations, and SHM potential among sensing methods [9]

Method	Strengths	Limitations	SHM Potential
Visual	Inexpensive equipment Inexpensive to implement No data analysis Portable Simple procedure	Only surface damage Only large damage Human interpretation Can be time consuming	Currently none
X-radiography	Penetrates surface Small defects with penetrant No data analysis Permanent record of results Simple procedure	Expensive equipment Expensive to implement Human interpretation Can be time consuming Require access to both sides Safety hazard	Currently none
Strain gauge	Portable Embeddable Surface mountable Simple procedure Low data rates	Expensive equipment Expensive to implement Data analysis required Localized results	Lightweight Conformable Can be deposited Very low power draw Results for small area
Optical fibers	Inexpensive equipment Embeddable Quick scan of large area	Expensive to implement Data analysis required High data rates Accuracy in question	Lightweight Large area coverage Must be embedded Requires laser
Ultrasonic	Inexpensive to implement Portable Sensitive to small damage Quick scan of large area	Very expensive equipment Complex results Specialized software High data rates Couplant required Require access to both sides	Currently none
Eddy current	Inexpensive to implement Portable Surface mountable Sensitive to small damage	Expensive equipment Very complex results Specialized software Safety hazard Conductive material only	Lightweight Conformable Can be deposited Very high power draw Results for small area
Acoustic emission	Inexpensive equipment Inexpensive to implement Surface mountable Portable Quick scan of large area Sensitive to small events	Very complex results Very high data rates Specialized software	Lightweight Conformable Can be deposited No power required Results for large area Triangulation capable
Modal analysis	Inexpensive equipment Inexpensive to implement Surface mountable Portable Simple procedure Quick scan of large area	Complex results High data rates Specialized software Results are global	Lightweight Conformable Can be deposited Multi-purpose sensors Low power required Results for large area
Lamb waves	Inexpensive equipment Inexpensive to implement Surface mountable Portable Sensitive to small damage Quick scan of linear space	Very complex results Very high data rates Specialized software	Lightweight Conformable Can be deposited Medium power draw Linear scan results Triangulation possible

2.1.5 Summary

Structural health monitoring is a major undertaking for complete robust and reliable use in future applications, especially in preparation for a move from time based

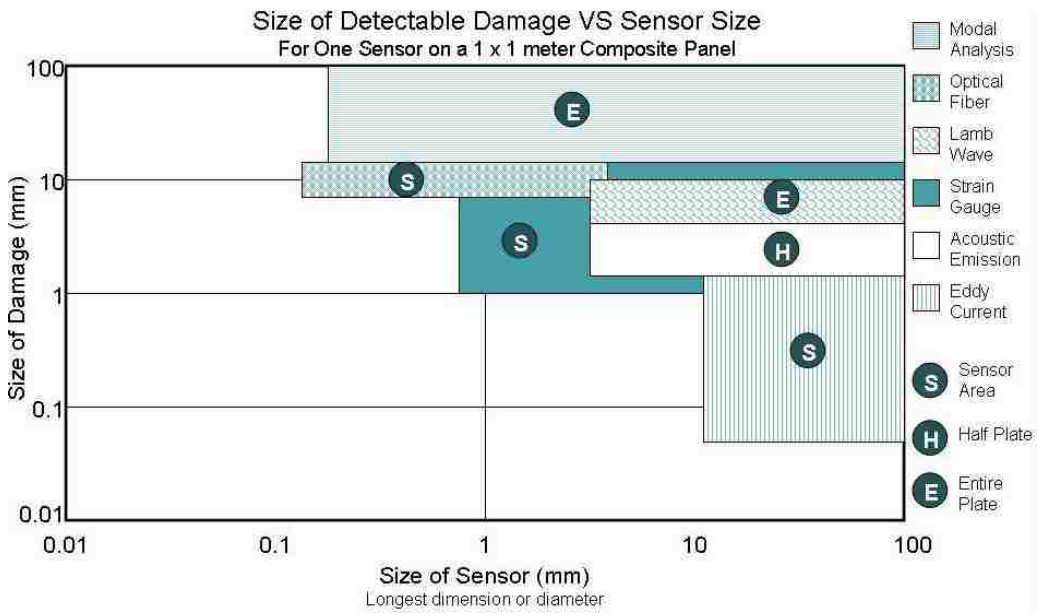

Figure 2.5: Detectable damage vs. sensor size [9]

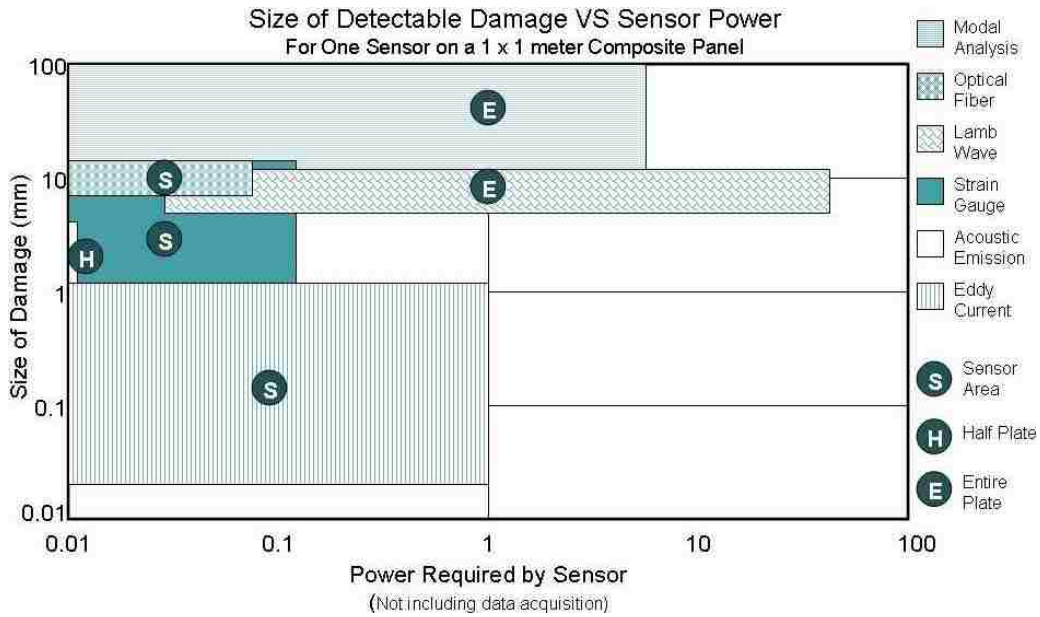

Figure 2.6: Detectable damage vs sensor power [9]

monitoring (TBM) to condition based monitoring (CBM). The aerospace industry may have the most significant need for smart structures applications. With such a high percentage of composites used in this industry, there is a great need for CBM systems capable of monitoring such materials. Financially, such a system can have great impact on the aerospace industry by efficiently monitoring old composite aircraft, extending the lifespan of new aircraft, and contributing to better designs for future aircraft. Current sensing methods show noticeable technology gaps in fulfilling the requirements necessary to bring SHM forward. New sensing techniques are needed to fill these gaps and contribute to the spectrum of sensing methods that can meet the various sensing needs. The composite patches used for composite repair may be an application where high sensitivity monitoring is useful.

2.2 Acoustic Bandgap Materials

2.2.1 Introduction

Acoustic bandgap materials have created a large spark in the research community since their emergence in 1993 by Kushwaha et. al. [26] with the first full band-structure simulation for periodic, elastic composites. Kushwaha et. al. credit their inspiration to Yablonovitch's work with macroscopic 'photonic crystals' that cause electromagnetic bandgaps in which electromagnetic waves are forbidden [27]. The propagation of elastic waves in periodic and random media, however, is an old topic that had been addressed much earlier [28].

Acoustic bandgap formation is attributed to Bragg reflections that can be caused by passing acoustic signal through a periodic composite material [29]. The gaps resulting from Bragg reflections in a square lattice occur at frequencies dependent on lattice constant a, the periodic spacing and are proportional to $1/a$ and $0.707/a$

corresponding to the period in the direction parallel to the wave propagation ([100] or ΓX in reciprocal space) and the diagonal direction ([110] or ΓM in reciprocal space) respectively and must be wide enough to overlap. However, surface reflections on the scatterer or wave propagation in the scatterer can help the gaps to overlap causing a full gap extending throughout the Brillouin zone (independent of polarization). Most interesting is the fact that the frequencies at which ABGs occur are scalable due to the proportionality with lattice constant 'a', a trait that is not shared by the photonic counterpart.

ABG crystal research has paralleled the ideas of photonic bandgap materials with great hopes for novel applications. Such applications for ABG devices are listed in the literature for uses in more efficient antennas [30], elastic wave filters [30], [31], vibrationless environments [26], better transducers for sonar/depth finding systems and medical ultrasonic imaging, noise control [32], waveguides [33], [34], and acoustic mirrors [35]. This topic of research has thus produced a great interest made evident by it's appearance in over 1000 published journal articles [36].

This section discusses work in the literature that pertains to obtaining and optimizing bandgaps analytically and experimentally. The full elastic plane wave equation for a homogeneous material is described by Equation 2.1.

$$(\lambda + 2\mu)\nabla(\nabla \cdot \overrightarrow{U}) - \mu\nabla \times (\nabla \times \overrightarrow{U}) - \rho\partial\overrightarrow{U} = 0 \tag{2.1}$$

$\overrightarrow{U}(\overrightarrow{r}, t)$, is the displacement vector as a function of position $\overrightarrow{r}$ and time t, λ and μ are the Lamè coefficients, ∇ is the Laplacian operator and ρ is the density of the material. Analytical methods used in the literature include the plane-wave expansion method (PWE), the finite-difference time-domain method (FDTD), the finite element method, and the variational method (VM). Experiments have shown acoustic bandgaps in one-dimension [37], two-dimensions [38], [39], [40], [41], [42], [43], [44], and three-dimensions [35]. There has been some confutation as some reported

experimental gaps represent only pseudogaps and not complete gaps [45]. Complete gaps are defined by a gap which exists independent of polarization of the wave and its propagation direction [46]. Much of the work cited above pertains to liquid-liquid or liquid-solid ABG composite materials, which is distinguished as 'sonic crystals' [29]. There is little work done for solid-solid or solid-liquid composite crystals, which has also been classified with the name 'phononic crystals' [29].

2.2.2 ABG Analytical Methods

The analogy between materials with the inhibition of spontaneous emissions and materials that disallowed vibrations was made leading to the first full band-structure calculations for such materials [26]. There exists a strong analogy in behavior and characteristics among phononic crystals, photonic crystals, and their electronic counterpart (Table 2.2). Kushwaha et. al. [26] showed computational results for the band structure of a periodic array of Nickel in Aluminum and vice-versa. The results are shown in Fig 2.7 with the vibrational gap found in the hatched area. It was found that Aluminum in Nickel produced a larger gap, although it was pointed out that the calculations did not consider the mixed longitudinal-transverse mode and was therefore not complete because the gaps were not independent of polarization. The authors considered the complete calculations for phononic gaps to be of comparable importance to the work in photonics. Sigalas and Economou [47] answered promptly with calculations showing a narrow, but complete bandgap for Gold (Au) cylinders in Beryllium (Be) using the transverse polarization mode as Kushwaha and Halevi had but also the mixed, longitudinal-transverse polarization mode using the plane wave expansion (PWE) method.

Another analytical method for simulating the band structures in two-dimensional phononic crystals is the variational method (VM) [48]. The variational method was

Table 2.2: Comparison among electronic, photonic, and phononic crystals [26]

Property	"Electronic" crystal	"Photonic" crystal	"Phononic" crystal
Materials	Crystalline (natural or grown)	Constructed of two dielectric materials	Constructed of two elastic materials
Parameters	Universal constants, atomic numbers	Dielectric constants if constituents	Mass densities, sound speeds c_l, c_t of constituents
Lattice constant	1-5Å (Microscopic)	0.1 mm – 1 cm (mesoscopic or macroscopic)	Mesoscopic or macroscopic
Waves	de Broglie (electrons) ψ	Electromagnetic or light (photons) **E, B**	Vibrational or sound (phonons) **u**
Polarization	Spin $\uparrow, \downarrow$	Transverse: $\nabla \bullet D = 0$ $(\nabla \bullet E \neq 0)$	Coupled trans-longit. $(\nabla \bullet u \neq 0, \nabla \times u \neq 0)$
Differential equation	$-\frac{\hbar^2}{2m}\nabla^2\psi + V(r)\psi = i\hbar\frac{\partial\psi}{\partial t}$	$\nabla^2 E - \nabla(\nabla \bullet E) = \frac{\varepsilon(r)}{c^2}\frac{\partial^2 E}{\partial t^2}$	(See Refs [27,28])
Free particle limit	$W = \frac{\hbar^2 k^2}{2m}$ (electrons)	$\omega = \frac{c}{\sqrt{\varepsilon}}k$ (photons)	$\omega = c_{l,t}k$ (phonons)
Band gap	Increases with crystal potential; no electron states	Increase with $\lvert\varepsilon_a$-$\varepsilon_b\rvert$ no photons, no light	Increases with $\lvert\rho_a$-$\rho_b\rvert$ etc. no vibration, no sounds
Spectral region	Radio wave, microwave, optical, x-ray	Microwave, optical	$\omega < 1$ GHz

first used by Sanchez-Perez et. al [41] and shows improvement over PWE in terms of convergence time [49]. It was determined that the VM works well at high frequencies for two-dimensional periodicity and converges faster than the PWE method.

The finite-difference time-domain (FDTD) method was used for the first time in

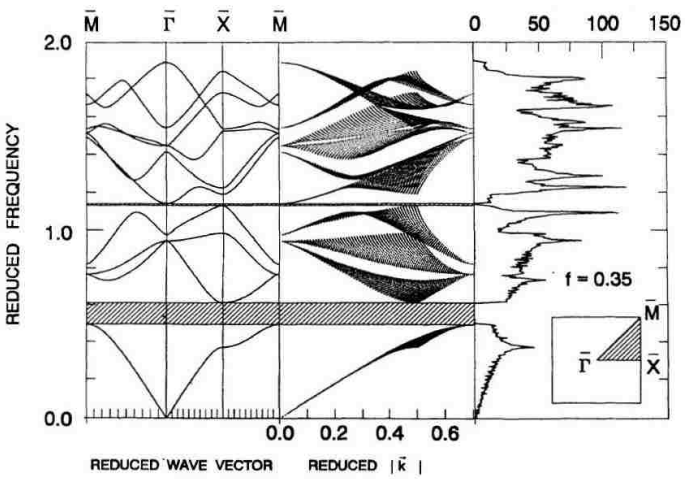

Figure 2.7: Acoustic band structure and density of states for Ni cylinders in Al forming a square lattice with a filling fraction of 0.35. The principal symmetry directions making up the Brillouin zone are shown on the lower right. [26]

the analysis of ABG materials with experimental validation [50]. FDTD was employed as an improvement upon the previously used plane wave expansion (PWE) method [47], [30] or the variational method (VM) [41] which endured setbacks due to convergence problems when dealing with solid-fluid composite ABG structures. Specifically, problems were encountered when using liquid materials and also finite systems. The lack of transverse velocity in liquids caused the Finite Fourier Transform of the Lam*é* coefficient μ not to converge in the PWE. This problem was traditionally side-stepped by using an imaginary μ, in which unrealistic effects may or may not reside. Also, FDTD can be used for simulating finite-sized structures [29]. FDTD was therefore employed to better simulate reality and along with this, more realistic boundary conditions were applied for a homogeneous surrounding environment.

The FDTD method discretizes the wave equations in both space and time in which the variables are then interlaced by a half a grid cell and approximated by center differences in both domains. This method was tested against experimental results that considered mercury (Hg), oil, and air in an aluminum (Al) host in separate tests for filling fractions of 0.22, 0.28, 0.35, 0.40, and 0.42 for each material combination. The experimental results matched up with the FDTD analytical results showing the importance of realistic transverse field components that were modified in PWE to allow for convergence. Vasseur et. al. [51] produced an in-depth overview of the PWE method and the FDTD method along with a study to use these two methods for comparison to experimental results consisting of filled and hollow Cu cylinders in air as well as other experimental results consisting of water instead of air. The experimental setup included Cu tubes with an inner radius of 13 mm and thickness of 1 mm and were 450 mm long. The lattice constant was 30 mm. A speaker connected to a low frequency generator was located 40 mm away from the sample face (first set of inclusions). The difference between the Fourier transforms of the test with the sample was subtracted from the test with run with no sample thereby removing

the background effect. It was demonstrated that that the FDTD and PWE methods agree below 10 kHz, where the assumption of rigid cylinders holds. Although, above 10kHz, only the FDTD method matched experimental results. When water was used instead of air, FDTD matched only up until 40 kHz when there was dependence based on cylinder wall thickness.

The FDTD method is used again for Mercury (Hg) spheres in an Aluminum (Al) host and for Aluminum (Al) cylinders embedded in a Mercury (Hg) host [52]. Sigalas et. al. compared two analysis using the FDTD method in a three-dimensional periodic system. The importance of transverse components in solids are discussed, as results for a case where transverse elements of the Aluminum (Al) scatterers are turned off and compared to the normal case in which the transverse components are not ignored [52]. Only very narrow gaps if any at all existed for the case where the transverse sound velocity in Aluminum (Al) was set to zero while normal conditions showed that gaps occurred for a wide range of filling ratios. Therefore, the transverse components in solid scatterers in a fluid host are of significance to bandgap occurrence.

In a similar test, two modes of FDTD algorithm were compared: a sonic version which deals only with longitudinal waves, and a phononic version which considers both longitudinal and transverse components [53]. The FDTD method had now been established in many publications [52], [50], [54]. It was demonstrated that the sonic FDTD had suitable agreement with the phononic version for methacrylic cylinders in air and Aluminum (Al) cylinders in air, however for the case of steel in water, there was a significant difference in the results. The correspondence of the phononic FDTD was confirmed over the sonic FDTD as predicted using an earlier experimental verification [55]. This could hint at the use of the sonic code for certain materials, although it could also be due to the frequency range at which the simulations were performed as the results for the PWE method were shown before [51].

2.2.3 Variational Studies

In attempts to create and optimize acoustic bandgaps, research investigations studied the effects of varying material parameters such as wave speed and impedance via density and modulus of elasticity in addition to geometrical parameters such as Bravais lattice type and filling fraction (FF) within each ABG material. Bravais lattice types are made up of a periodic arrangement repeated at each lattice point oriented in such arrangements as a square lattice, oblique lattice, rectangular lattice, monoclinic lattice to name a few [53], [56]. Filling fraction (FF) is a quantity to summarize the portion of cross-sectional area of the unit cell occupied by the scatterer material. For a a square lattice with circular inclusions of radius r, the relation is provided by Equation 2.2 below.

$$FF = \pi[\frac{r}{a}]^2 \tag{2.2}$$

An overview of all the material properties cited in this chapter is given in Table 2.3 at the end of the chapter.

Once obtaining the ability to calculate coupled longitudinal and transverse modes, Kushwaha et. al. [32] presented the band structure for Nickel (Ni) in Aluminum (Al) (and vice-versa) with the mixed-mode calculations. A complete bandgap extending throughout the Brillouin zone was shown. The Brillouin zone is the irreducible zone in which symmetry occurs [57]. An outline of the general equation of motion for an inhomogeneous system that supports the coupled longitudinal and transverse modes was also given. The equation is isolated down to a special case of a binary composite material with two-dimensional periodicity on a plane perpendicular to the plane of wave propagation. The band structure for the square lattice with a filling fraction of 0.35 can be seen in Figure 2.7. A maximum at a filling fraction of about 0.3 is found for this material type and lattice type based on a curve representing gap width

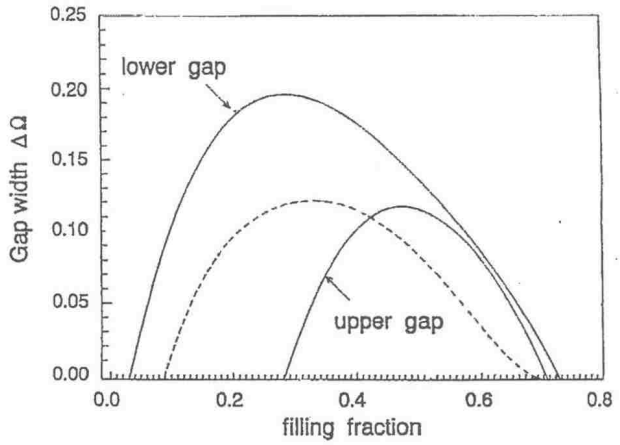

Figure 2.8: The normalized gap width vs filling fraction to find maxima for hexagonal lattice. The first gap for the hexagonal lattice is indicated 'lower gap', the second gap by 'upper gap' and the dotted line represents the first gap for the square lattice. [58]

against filling fraction (Fig 2.8). Kushwaha and Halevi [58] soon after presented acoustic bandgaps in the band structures for nickel (Ni) cylinders in an aluminum (Al) matrix arranged in a hexagonal lattice with the mixed-mode calculations. The plot of gap width vs. filling fraction can also be seen in Figure 2.8 along with the result from the square matrix. Since the gap did not vary for a constant structure with a variable filling fraction on the reduced frequency plot, it was thus illustrated that the gap occurrence in the frequency domain was inversely proportional to lattice constant 'a'.

A simple one-dimensional simulation was conducted [30] to find an ABG using materials consisting of thin and thick plates using molybdenum (Mo) in lucite, iron (Fe) in lucite, steel in lucite, Al_2O_2 in Lucite, Al_2O_2 in aluminum (Al), and iron (Fe) in aluminum (Al). Bandgaps were presented in terms of a ratio factor where the gap width is divided by the center frequency of the gap to provide an objective measure of the gap quality and are shown here in Figure 2.9. It was found that the thin and thick plates produced very similar results with the Mo in Lucite yielding the best

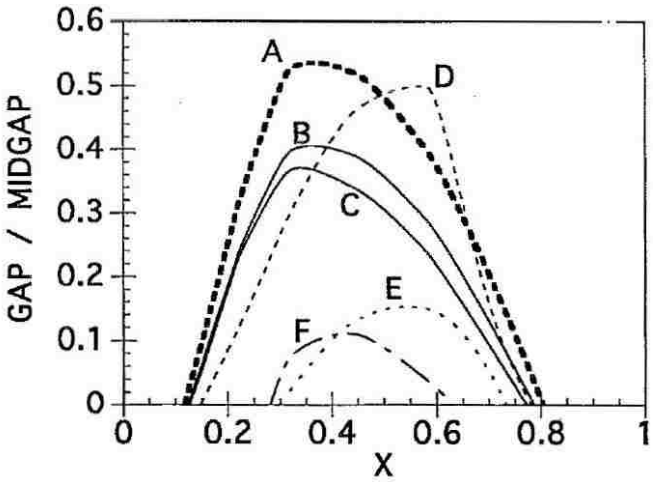

Figure 2.9: Gap-to-midgap ratio of scattering component for x in x-y polarization: (A) Mo in lucite, (B) Fe in lucite, (C) steel in lucite, (D) Al_2O_2 in lucite, (E) Al_2O_2 in Al, and (F) Fe in Al [30]

results with a gap to midgap ratio of 0.54 at a filling fraction of about 0.3 as shown.

The band structure results for two-dimensional and three-dimensional periodic composites made from spheres, cubes, and rods consisting of Steel, Nickel (Ni), Lead (Pb), and Copper (Cu) in a homogeneous polymer matrix was shown by Kafesaki et. al [59]. It was re-established that the geometrical conditions responsible for the formation of bandgaps are dependent upon the volume filling fraction and the lattice structure as previously shown [47], [32], [58]. The materials used are also considered to have strong influence on gap production as expectations for high contrast density between the two materials involved were verified [59]. These results showed that high density scatterers in a low density background was more important than velocity mismatch. Their investigation also showed the advantage of using a polymer, specifically citing epoxy, due to it's low density and its ease for fabrication as a ABG material.

The importance of density has been alluded to already [59], although another investigation tests which specific parameter contrast has a greater affect. The acoustic

impedance contrast versus the velocity contrast between the host and inclusion materials is compared among varying filling fraction [60]. Here, the results for fictitious solid materials showed that the ABG becomes wider for high variation in impedance than for varying velocity, and a maximum is found at an intermediate filling fraction for the parameters given.

Material parameters were tested again in an investigation where large bandgaps were presented originating from a three-dimensional sonic crystal made of spherical water balloons in a Mercury (Hg) host [31]. Face-centered cubic (fcc), body-centered cubic (bcc) and simple cubic (sc) arrays were all considered. The face-centered cubic yielded the largest gaps at a gap/midgap ratio of 0.83, the biggest gap shown in the literature in any dimension. Each array type had a gap maxima occurring at a filling fraction of 0.24. These results had opposed a previous conclusion that a low-density, high velocity material in a high-density, low-velocity material could not produce a bandgap [61]. Kushwaha and Djafari-Rouhani [31] again emphasized that the density contrast is what should be attributed to the gaps formation, an instance that is not analogous to photonics.

Geometrical changes were also tested for constant material types to see the effects. Kushwaha and Djarfari-Rouhani [46] tested a honeycomb lattice (hexagonal) structure of infinitely rigid metal inclusions against a simple square array. Not only did the hexagonal lattice produce a wide gap, but gaps were also found for a wider range of filling fractions. Kushwaha and Djarfari-Rouhani also introduced an interesting concept for the creation of a super bandgap by initiating simultaneous gaps through a tandem structure of multiple lattice constants and radius values (Figure 2.10). It was pointed out that the stop bands can be raised (lowered) in the frequency domain by decreasing (increasing) the lattice constant 'a' as noted previously [31]. The idea opens the door to gap widths never before encountered through the idea of gap superposition.

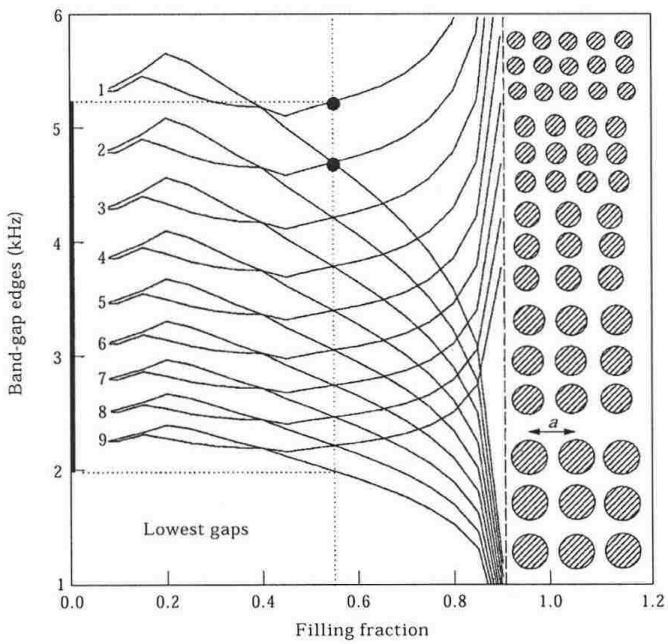

Figure 2.10: Proposal of a super-wide acoustic bandgap signified by the dark line on the left. The gap extends from the low frequency gap to the high frequency gap through stacked lattice structures [46]

Like the original of ABG, some research investigation paralleled photonic bandgap findings. Caballero et. al [56] tested the idea that a reduction in symmetry in the unit cell can widen the bandgap. The reduction in symmetry was proposed for a simple square lattice of cylinders by placing a smaller sized cylinder at the center of the unit cell. Not only did the bandgap widen for the cases with an additional inclusion, but also allowed for a higher filling fraction as the additional inclusion in the open space pushed the close-packing condition from 0.78 to 0.92. The enlargement of the gap was based on the idea of creating more scattering modes.

Goffaux and Vigneron [62] examined the concept of bandgap adjustment or 'tuning' using long square rigid inclusions in a square host matrix and showing the effect of their rotation as seen in Fig 2.11. Filling fraction and rotation angle of the square scatterers (with respect to the square host) is illustrated in Fig 2.12 using PWE and

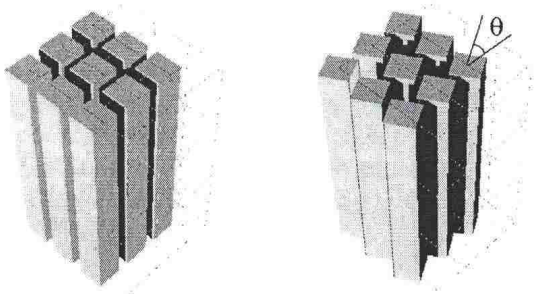

Figure 2.11: Square inclusions in square lattice formation showing rotation [62]

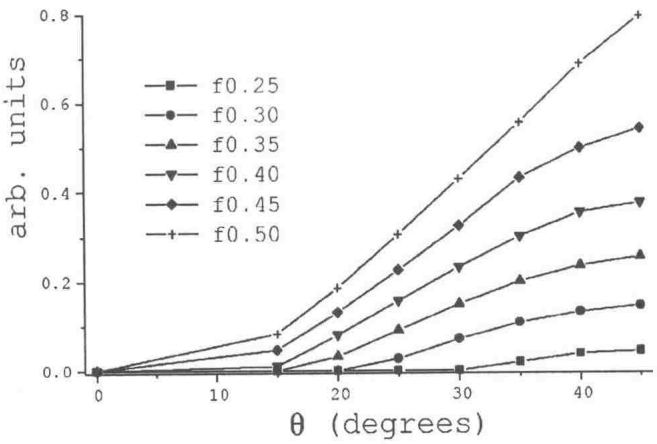

Figure 2.12: Square inclusions in square lattice formation showing rotation [62]

FDTD. It was found that the rotation angle of the inclusions in conjunction with the filling fraction can act as a tuning mechanism for isolating desired gap widths. This concept can enhance the manipulation and control of bandgap production for applications with specific bandgap width requirements. Another type of adjustment in the frequency domain was shown by introducing a polymer coating to the scatterers [62]. The coated cylinders lowered the midgap frequency by two orders of magnitude.

In a different type of research, the finite element (FEM) method was coupled with optimization to find the optimal topology for a two-dimensional crystal with scatter-

ers [63]. A matrix of epoxy with aluminum inclusions was considered. Optimization for an initial case of diamond-shaped inclusions and square-shaped inclusions converged to a circular-like inclusion. It was found that a mass-damping coefficient of 75,000 in the finite element model was optimal to reduce resonant peaks, but would not hinder the gap. In addition, the removal of small resonance peaks assured the bandgap location. This research showed that FEM can be used analytically determine gap locations for given materials and geometries.

While some research focuses on constructing the bandgap, other research measures bandgap resistivity based on induced changes, such as waveguides. The arena of waveguides has become more populated with the introduction of ABG [33], [34]. Sigalas analytically constructs such a device by introducing defect states into an ABG material [33]. In addition to waveguides, Miyashita also played with the notion of defect modes [53]. Defects in the periodic structure of the lattice such as the image shown in Fig 2.13 were introduced to determine the consequent effects. A defect, such as one shown in Figure 2.13 can in turn cause a passband, thus disrupting the bandgap as seen in Fig 2.14. In a similar case Psarobas et. al. [64] examines a three-dimensional fcc lattice structure with lead spheres to illustrate how introducing impurities can affect the gap. Such impurities as planes of spheres with small diameters cause deterioration in the bandgaps.

2.2.4 ABG Experimental Investigations

James et. al. [37] conducted a study for a one-dimensional sonic bandgap consisting of a theoretical calculation and an experiment. The experiment consisted of two scenarios of perspex plates of thickness d = 0.4 mm in one case and d = 2 mm in the other both held by a frame. The frame was placed in a glass tank (300 x 300 x 600 mm) and filled with water. Two transducers with diameters of 38 and

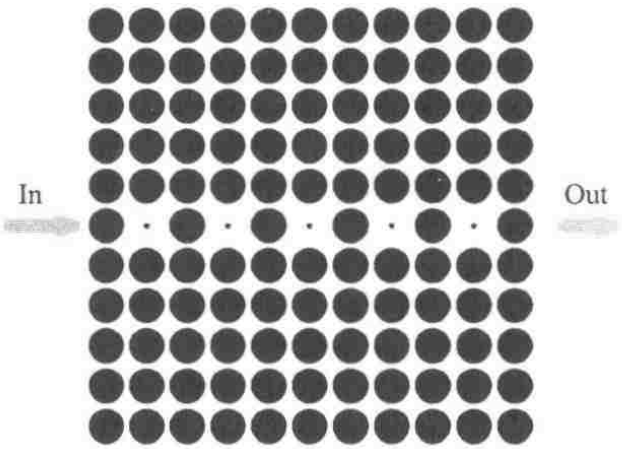

Figure 2.13: Image of defect mode (waveguide) along line of wave propagation [53]

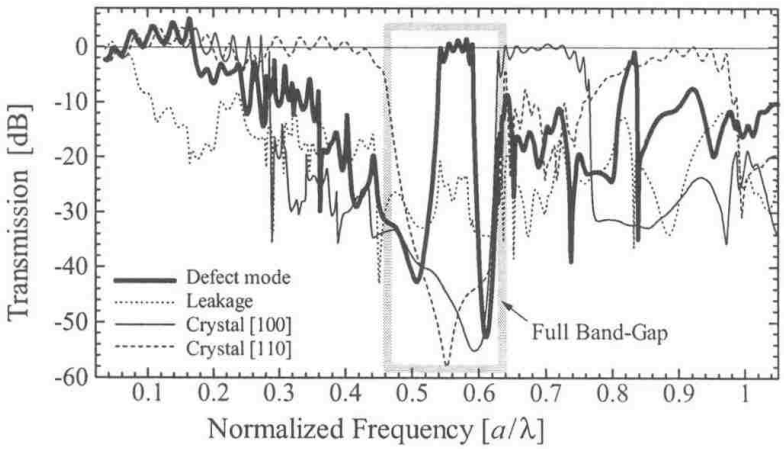

Figure 2.14: Passband formed within acoustic bandgap by defect mode for methacrylic resin cylinders in air [53]

29 mm with resonant frequencies of 2.25 and 0.5 MHz (respectively) were used at frequencies below resonance. A function generator was used and setup to trigger the digital oscilloscope. Ten signals were averaged to reduce noise in the data. The sampling interval was set to 0.5 μs resulting in a Nyquist frequency of 1 MHz, well above the maximum interest frequency of 600 kHz. The total window used 1024 points for a resolution of about 2 kHz. The theoretical results using the casual

surface Green's function method (CSGFM) for nontrivial geometries matched up with the experimental results for periodicities numbering between 2 and 10 plates ; more plates show deteriorated matching due to slight variations in periodicity. Defect states were produced such as modification in plate composition, thickness of plates, and plate spacing (where a plate is removed) exhibited narrow transmission bands in the gap. This study showed the ease in creating a one-dimensional sonic crystal and stated how the position and width of the stop bands (and passbands) can be modified through changes made in dimensions and materials of the unit cell.

The first ultrasonic bandgap was shown using an aluminum (Al) host with a square configuration of cylindrical holes filled with Mercury (Hg) [38]. The outline was to use inclusions with a low propagation velocity, but higher density with relation to the surrounding host medium. The experimental setup makes use of broadband ultrasonic transducers with a diameter of 20 mm and is processed with a digital oscilloscope. It was found that the maximum signal-to-noise ratio (SNR) was about 50 dB for the oscilloscope. A second experimental setup used a gain-phase analyzer to study the dispersion relations. The lattice constants used were 3.25 mm, 2.58 mm, and 2.8 mm, resulting in bandgaps at center frequencies of about 750 kHz, 800 kHz, and 850 kHz.

The first experimental support for two-dimensional ABG material capable of full phononic bandgap was shown by Vasseur et. al. [39]. This group alluded to the previous experimental two-dimensional acoustic bandgap done before this, however it was done using Mercury cylinders in an Al host making it a sonic crystal due to the liquid inclusions [38] and lacked analytical prediction. Vassuer et. al [39] used an analytical model developed by Kushwaha [32], [58], [31] with their experiments, emphasizing the necessity of a prediction model with reliability to adequately use the term 'engineered bandgap'. The samples tested consisted of two composite binary materials with dimensions 100 x 100 x 100 mm made of Duralumin cylindrical

inclusions in an epoxy host. One specimen was made with a square lattice structure with a lattice constant a = 20 mm and the other specimen made of a centered rectangle lattice of periodicity a = 20 mm and b = 2a = 40 mm, both containing cylinders of diameter of 16 mm (Fig 2.15). The experiment used a broad-band 500 kHz P-transducer as the emission source and the measurement of the signals was performed with a TDS 540 oscilloscope with a TD100 Data Manager. The transducers' diameters were 31.75 mm. The results for transmitted power can be seen in Figure 2.16. The experimental results gave strong evidence of an absolute bandgap and coincided with the theoretical results at a center frequency of 90 kHz, although some portions of the gap has transmission slightly above the noise floor. A possible second gap may be considered at 110 kHz, but is shown extremely narrow. This could be attributed to the finite nature of the specimen's lattice in x,y and z directions, the small dimensions of the transducers, which were on the same order as the lattice constant, or the measurement equipment. Although one of the gaps was in question of being a pseudogap, the first major experimental gap was in good agreement with the prediction from the theoretical model.

Experimental results for a sculpture made of metallic rods in air gained great attention in the scientific community once published [65]. Kushwaha and Djarfari-Rouhani [46] immediately discussed the recent sculpture that was used to test for acoustic bandgap finding that it was only a pseudogap that was found. A pseudogap is a gap present in limited directions [45] and not throughout the entire Brillouin zone. Soon after, others mimicked the structure with slight variation in an attempt to create the gap that was almost present.

Robertson and Rudy [40] commented on the previous test using a sculpture to show an ABG [65] using a recommendation to increase the filling ratio based on calculations finding that the full bandgap was not achieved due to the low filling ratio [45]. Robertson and Rudy created a two-dimensional array of metal cylinders

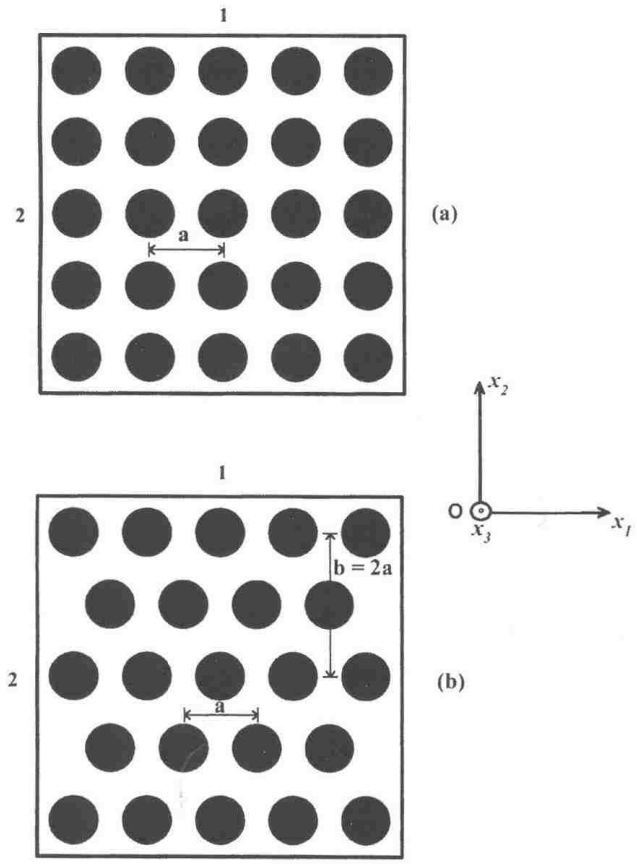

Figure 2.15: Geometry layout for square lattice (a) and centered rectangular (b) [39]

in air (similar to Martinez-Sala et. al. [65]). A lattice constant of 3.7 cm with inclusions of 2.34 cm diameters was used to achieve a filling fraction of 0.31, barely greater than the recommended filling fraction to produce a complete bandgap. An impulse signal generated by the second derivative of a gaussian pulse was fed into a computer and then to a speaker which in turn was directed first through air with no sample. This was done in succession between 200 and 500 times and then repeated with the sample of six rows of rods. Frequency steps at about 166 Hz at a total time window of 6 ms was chosen for the Fourier analysis into the frequency domain. Anomalous dispersion in phase data was also used in this case to determine gap formation. The relation discussed in this paper to locate the center frequency gap

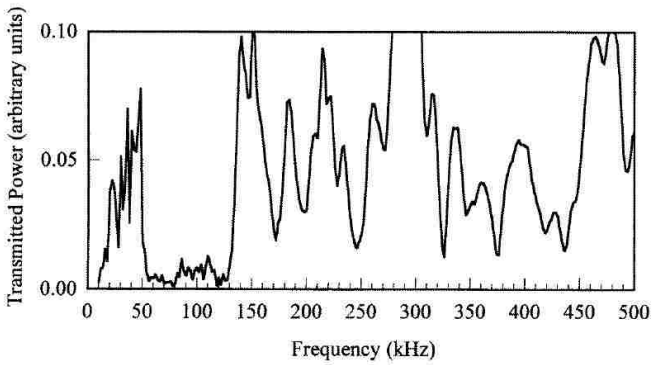

Figure 2.16: Transmitted power spectrum for a square array of Al cylinders in epoxy measured at the opposite end of specimen from the transmitted signal [39]

in the [110] direction is incorrect. Robertson and Rudy give the inter-lattice spacing between the diagonal Bragg mode as Equation 2.3 rather than Equation 2.4.

$$f = \frac{a}{\sqrt{2}} \tag{2.3}$$

$$f = a\sqrt{2} \tag{2.4}$$

Therefore the incorrect reported expected value of 6498 Hz is actually twice the true analytical prediction and actual gap location of 3249 Hz, which matches the results.

Rubio et. al. [42] also performed experiments inspired on the initial sculpture by Matinez-Sala et. al [65] although consisting of more variations such as using steel and wood as scatterers instead of aluminum (Al). The plane wave expansion (PWE) method was used to test against the experimental results. Configurations with geometrical parameters include a lattice constants of 5.5 and 11 cm for square lattices and 6.35 and 12.7 cm for triangular lattice with inclusion diameters of 1, 2, 3, and

4 cm. A speaker and microphones were used to send and detect white signal in the audible frequency. The interest here is that hollow and full aluminum cylinders as well as wood cylinders are used in the same configuration (both square and triangular) to produce the same results (same center bandgap frequency). The results show gaps in terms of attenuation to demonstrate the independence of inclusion material type for the formation of a bandgap in sonic crystals concerning rigid materials in air.

2.2.5 Scalability for Micro-sized ABGs

The scalable nature of ABG allows for micro-scale devices that have corresponding center frequencies above the kilohertz regime. For example, phononic bandgaps have traversed into the surface acoustic wave (SAW) dominion at the gigahertz range [66]. A picosecond transient photoacoustic technique, also known as impulsive stimulated thermal scattering (ISTS) was used to characterize the surface acoustic waves. Many SAW devices may have relevancy with the results shown here such as microelectronic structures and electromechanical and microfluidic devices. The simplicity of the gap creation was based on one-dimensional gratings using conventional lithography methods [67].

In addition, the true scalability of phononic crystals is looked at on the atomic level using calculations for nanoscale HFO_2 in ZrO_2 [68]. The investigation looks at the range of validity for continuum assumptions. The results suggested that the wave propagation using continuum description become invalid as dimensions approach nanometer scales. A thickness dimension of $10\mathring{A}$ and upward was distinguished as the threshold for continuum description to start showing validity. It was pointed out, as ABG devices materialize in the nano-scale (THz region), other methods will need to be used to simulate their behavior. Small scale ABG devices have also been

proposed and tested as biosensors [69]. The goal was to compare the ability of the phononic crystal to the current biosensing technique using surface acoustic wave (SAW) devices.

Actual designs of microscale ABG devices using micron-scale geometries were verified experimentally in recent reports [70], [71]. The MEMS device in this project was designed for a phononic gap ending at 67 MHz and realized through microfabrication methods to achieve a lattice constant of 45 μm and a diameter of 28.8 μm for one device and values with double for another device. The matrix material consisted of SiO_2 and contained nine rows of Tungsten (W) cylinders. A pure matrix device was tested using a network and an electo-acoustic coupler. The process was repeated for the device containing the Tungsten (W) cylinders. The pure matrix device was tested for comparison with the Tungsten inclusion device and also for data normalization. The results for the first device show a noticeable transmission drop between 59 MHZ and 76 MHz and coincide with FDTD simulations exhibiting only a slightly wider and less significant transmission drop. The second device exhibited slightly greater attenuation with a gap located between 27 and 39 MHz. The small discrepancies are attributed to an ideal simulation case with no imperfections, losses due to material, and infinite periodicity which is not achieved experimentally. It was concluded that the achieved gaps were successful due to high impedance and high density inclusions in a low-density, low impedance matrix. It was also noted that slanted couplers minimized length-dependent resonance effects. Such devices were cited to have applications in communications, ultrasound, and even non-destructive testing. This research is carried forward by optimizing the gap width and depth using the same materials [70]. It was shown that an optimal gap width and depth can be found at a filling fraction of about 0.32 (Figure 2.18). A high peak for gap depth is achieved at a greater filling fraction, yet at the expense of gap width. This can be attributed to easy navigation of elastic waves around the scatterers through the matrix for low filling fractions and the occasion where the waves bounce from

scatterer to scatterer due to the close proximity of the scatterer centers in high filling fractions (supported earlier [59]).

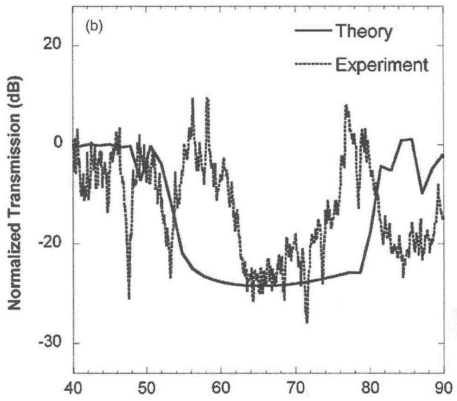

Figure 2.17: Experimental and theoretical results for Tungsten in SiO_2 [70]

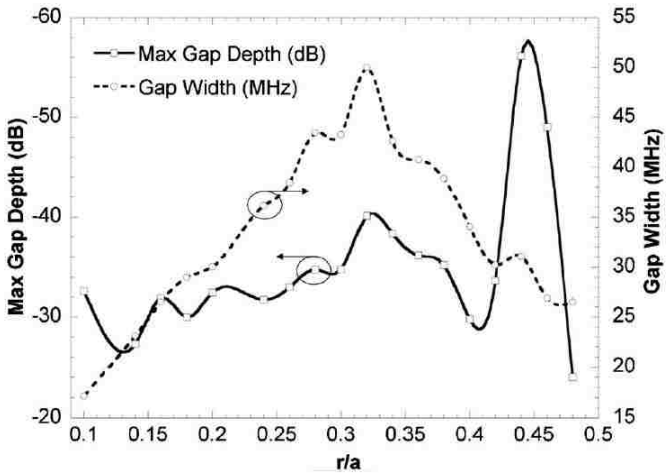

Figure 2.18: Optimal gap depth and gap width for Tungsten in SiO_2 in terms of filling fraction [70]

2.2.6 Summary

Acoustic bandgaps have been studied thoroughly now for about almost two decades [26] and have shown progress in theoretical simulations from PWE method [33] to

FDTD [50] and FEM [63] and experimentally [37], [39]. Many applications have also been listed such as noise filters [32], vibrationless environments [26], and even sensors [69], [70]. Different approaches for creating and optimizing acoustic bandgaps up to present time have been presented including geometrical variations and material variations. Table 2.3 gives a summary of the materials and material properties used in the various analysis. Values in bold represent properties reported explicitly in the literature and references are provided for each material used. It is obvious that there has been a great deal of work in this area, although there is still progress to be made for more understanding in exploiting the possible variational combinations to achieve the desired outcome for various applications in ABG.

Table 2.3: Materials and their properties used in the literature

Material	ρ **(g/cm³)**	$\mathbf{E_{11}}$ **orK (GPa)**	ν	$\mathbf{C_l}$ **(km/s)**	$\mathbf{C_t}$ **(km/s)**	**Z Mrayls**	**Reference**
Nickel (alloy)	**8.936**	*180.000*	*0.310*	*4.488*	*2.916*	*40.106*	[26]
Aluminum (alloy)	**2.697**	*70.000*	*0.350*	*5.095*	*3.105*	*13.740*	[32]
Distilled Water	**1.000**	*2.190*		**1.480**		*1.480*	[37], [35], [51]
Gold (Au)	**19.488**	*78.000*	**0.421**	*2.001*	*1.177*	*38.988*	[30]
Beryllium (Be)	**1.855**	*287.000*	**0.042**	*12.439*	*8.436*	*23.073*	[30]
Aluminum Oxide (Al2O2)	**3.986**	*300.000*	**0.233**	*8.675*	*5.578*	*34.580*	[30]
Copper (Cu)	**8.960**	*200.122*	**0.345**	**4.726**	**2.298**	*42.345*	[30], [59]
Iron (Fe)	**7.860**	*289.029*	**0.285**	**6.064**	**3.325**	*47.663*	[30], [59]
Aluminum (Al)	**2.734**	*68.000*	**0.353**	*4.987*	*3.024*	*13.635*	[30]
Lead (Pb)	**11.357**	*52.889*	**0.405**	**2.158**	**0.860**	*24.508*	[30], [72], [64]
Molybdenum (Mo)	**10.200**	*329.000*	**0.304**	*5.679*	*3.515*	*57.929*	[30]
Steel	**7.890**	*278.388*	**0.300**	**5.940**	**3.220**	*46.867*	[30]
Lucite/Perspex	**1.180**	*8.602*	**0.400**	*2.700*	*1.614*	*3.186*	[30], [37]
Steel	**7.900**	*256.671*	*0.300*	*5.700*	*3.535*	*45.030*	[37]
Tungsten (W)	**18.700**	*512.086*	*0.280*	**5.233**	**2.860**	*97.857*	[59]
Nickel (Ni)	**8.968**	*311.541*	*0.310*	**5.894**	**3.219**	*52.857*	[59]
Steel	**7.800**	*275.212*	*0.270*	**5.940**	**3.220**	*46.332*	[59], [72]
Silver (Ag)	**10.635**	*152.682*	*0.370*	**3.789**	**1.950**	*40.296*	[59]
Epoxy	**1.180**	*7.613*	*0.450*	**2.540**	**1.160**	*2.997*	[59], [72], [64]
Water	**0.998**	*2.237*		**1.497**		*1.494*	[31], [72]
Mercury (Hg)	**13.500**	*28.384*		**1.450**		*19.575*	[31]
Water 2	**1.025**	*2.403*		**1.531**		*1.569*	[72]
Duralumin	**2.799**	**112.600**	*0.320*	**6.342**	**3.095**	*17.751*	[39]
Epoxy 2	**1.142**	**7.540**	*0.450*	**2.569**	**1.139**	*2.934*	[39]
Glass	**2.459**	*78.776*		**5.660**		*13.918*	[35]
Glass 2	**2.767**	*92.569*		**5.784**		*16.004*	[35]
Gold (Au)	**19.500**	*220.147*	*0.420*	**3.360**	**1.239**	*65.520*	[48]
Epoxy 3	**1.180**	*7.583*	*0.450*	**2.535**	**1.157**	*2.991*	[48]
Air	**0.001**	*0.000*		**0.340**		*0.000*	[51]
Copper (Cu)	**8.950**	*167.803*	*0.310*	**4.330**	**2.900**	*38.754*	[51]
Silicon (Si)	**2.330**	*186.639*	*0.278*	**8.950**	**5.360**	*20.854*	[73]
Polymer (SU-8)	**1.190**	*4.029*	*0.450*	**1.840**	*1.080*	*2.190*	[74]
AlN	**3.230**	*308.313*	*0.240*	**9.770**	*6.204*	*31.557*	[74]
Silicon (Si)	**2.330**	*169.136*	*0.278*	**8.520**	*5.329*	*19.852*	[74]
Silicon Oxide SiO2	**2.200**	*75.032*	*0.170*	**5.840**	**3.764**	*12.848*	[74]
Tungsten (W)	**19.250**	*409.298*	*0.280*	**4.611**	**2.980**	*88.764*	[70]

Chapter 3

Experimental Methods

3.1 Introduction

This chapter presents the experimental methods for producing and testing an acoustic bandgap (ABG) material. This chapter also provides the pertinent experimental observations and results along with a discussion on the findings. The goals of these experiments are to examine the possible use of ABG materials as sensors for damage detection. Two sets of binary composite ABG materials were fabricated using a simple cubic array of cylinders in a host material. The two sets differ in host material, but contain the same material for the cylindrical inclusions. Each ABG material set included a short and long sample with filling ratios 0.18, 0.28, 0.40, and 0.50, totaling 16 samples. This was done to allow for variability in the size dimension thereby removing biases due to dimensionality of sample size and enhancing true repetitive behavior such as a bandgap. In addition, each material sample set was accompanied by a short and long sample of pure matrix material without inclusions to serve as a control and was used for normalized the data output.

The outlined goal of the experiments was to demonstrate two fundamental prop-

erties:

1) Demonstrate the ability to engineer an acoustic bandgap material

2) Demonstrate and examine the change in the bandgap profile exposed to uniform and non-uniform strains initiated with damage in the substrate adhered to the ABG sensor

The sample materials cover the probable range of filling fractions (0.20-0.50) in which bandgaps occur. The materials utilized in these experiments also constitute the physical characteristics of bandgap materials noted in the literature: large impedance mismatch between scatterer and matrix, density difference, and consequently a velocity imbalance. The host material dictated the design since a material had to be selected with relatively low stiffness to enable tension or compression during testing to achieve noticeable strains. A uniform strain can represent environmental changes and their effect on the substrate. Such instances as temperature, humidity , and pressure changes can therefore be differentiated. On the other hand non-uniform strains are representative of localized effects in the substrate such as damage or possibly delaminations that are common to composite materials. Non-uniform strains such as damage or delaminations cause more concern and consequently require a different feature response than uniform strains. The conceptual idea behind the use of ABG materials as sensors is that ABG sensor response will effectively encounter a deteriorated acoustic bandgap indicating non-uniform strain due to the variation in the highly critical periodicity of the inclusions as described in Figure 3.1.

The first section of this chapter defines the materials used and outlines their corresponding material properties that show relevance in this research. The following section describes the preparation of the samples and the experimental setup that was used during testing. The results are then presented and proceeded by a discussion of the experimental findings.

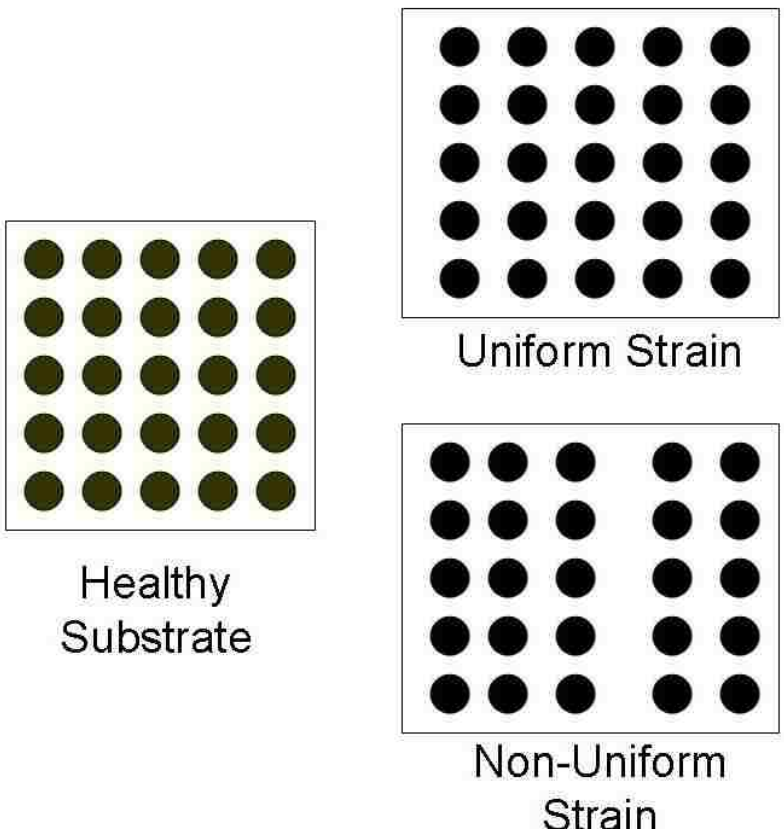

Figure 3.1: Schematic representation of ABG sensor adhered to a healthy substrate experiencing no strain, a uniformly tensioned substrate, and a non-uniformly tensioned substrate

3.2 Materials Overview

The ABG specimens are composed of three main materials: a polymer host, aluminum inclusions, and piezoelectric ceramic elements. The acoustic bandgap specimen is shown in Figure 3.2, where the polymer is used as the host material for each specimen type, the aluminum is used for the cylindrical inclusions making up the scatterers, and the piezoelectric ceramics are used as the transducer and actuator for each specimen. The functional material properties are given in Table 3.1.

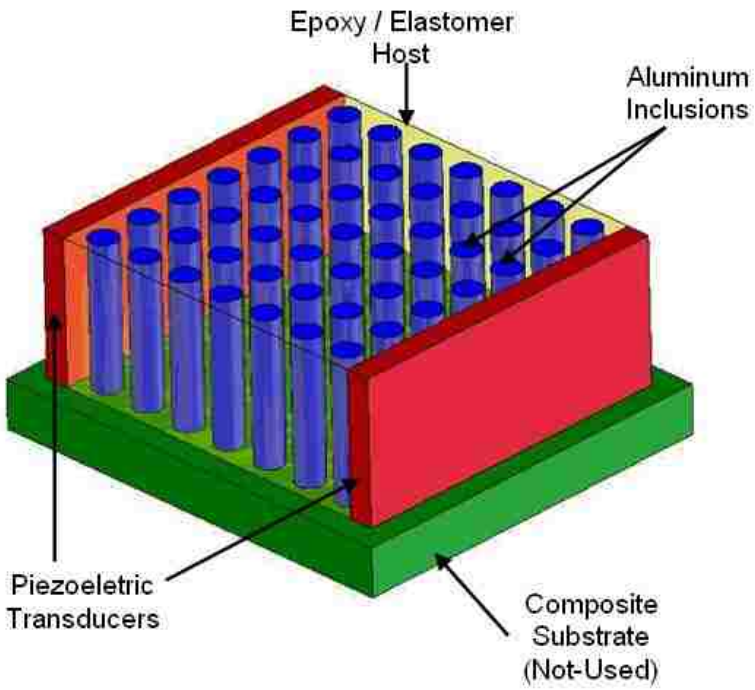

Figure 3.2: Pictorial of Fabricated ABG with Materials: Piezoelectric Ceramic (Red) on sides, Polymer host (Transparent Yellow), Aluminum (Al) (Blue) inclusions, and Composite substrate (Green)-not fabricated in experiments

3.2.1 Host Materials

The selection of the host material was based on the functional theory of the acoustic bandgap device for the proposed use as a sensor. Successful bandgap crystals reported in the literature review required significant difference in acoustic impedance between the matrix and inclusion materials. However, there exists practical limitations. For example, choosing liquid as a host material would introduce foreseeable difficulties in fabrication to isolate/package the liquid and couple the transducers in addition to proving the feasibility of the proposed sensing technique. On the other hand, a stiff solid material would also obstruct the sensing concept which requires the ability of the sensor to magnify the response of the substrate. Therefore a solid ma-

Table 3.1: Material Properties of materials used to fabricate ABG specimens

Material	ρ (kg/m^3)	**E (GPa)**	c_l **(km/s)**
Piezoelectric Ceramic	7700	63.00	2860.4
Elastomer	1119	0.00	21.1
Epoxy	1110	2.89	1613.6
Aluminum 1100	2710	68.90	5042.3

terial with a stiffness significantly lower than that of potential composite substrates is desired.

Two polymer host materials were examined in these experiments. Polymers are classified as hydrocarbons and are made up mainly of covalent bonds. Polymers are strongly linked to their molecular makeup in terms of the types of elements and structure by which they are made. Polymers are characterized greatly by the formation of long flexible chains and their large molecules in comparison to other hydrocarbons. The chains are made up of stable molecules called monomers, which link up leading to the term *polymer*. Polymers are composed of a wide variety of materials from polyester to polyisoprene (rubber) based on the different molecular weights and interaction of the polymer chains [14]. Cross linking occurs in many polymers through synthesis or nonreversible chemical reactions which occurs when chains that have been formed become bonded. The isotropic behavior of polymers is attributed to the randomness of the bonded polymer chains in all three dimensions effectively causing similar behavior in any direction.

Silicone elastomer is a type of polymer that easily deforms. This is indicated by the low elastic modulus and high failure strain. The specific elastomer used was Sylgard 186®, which was chosen as a representative elastomer for ABG testing as it provided a middle-range level of stiffness for elastomers. In addition, Sylgard 186 is a clear elastomer and thus allowed for visual inspection of air bubble formation during fabrication. Relatively large (visual) air bubbles would hinder uniform transmission

of the elastic wave that travel through the polymer during testing. Elastomer polymerization is achieved by mixing two components, a base and a curing agent, in which a chemical reaction occurs causing the formation of three-dimensional chains. Cross linking in elastomers is called vulcanization which takes place during the curing process. Elastomers are isotropic, exhibiting the same material properties in all directions.

The other host material that was considered for the makeup of the ABG sensor is a simple Epoxy with stiffness relatively lower than composite substrates. Aeropoxy®(Aeropoxy®PR2032-Resin PH3660-Hardener) was selected due to its midrange stiffness and the fact that it is translucent, making it possible to control air bubbles. Epoxies also offer string adhesion which can be of great advantage during fabrication to attach the piezoelctric crystals as transducers. Epoxies generally range in Elastic Modulus from about 2 GPa (290 ksi) to 8 GPa (1160 ksi) and up if reinforced.

3.2.2 Inclusions

A high tolerance periodicity among the scatterers is desired in order to show a bandgap in this investigation. Heat sinks made of Aluminum 1100 with periodic cylinders held by a flat square base were used. Aluminum 1100 is a low alloy aluminum made up of around 99 percent aluminum, 0.05-0.2 percent copper, 0.05 percent manganese, 0.95 percent silicon and iron, and less than 0.1 percent zinc. Initially two heat sink types were used to produce long and short specimens with filling fractions (FF) of 0.18 ($r/a = 0.24$) and 0.40 ($r/a = 0.36$). One heat sink is shown in Figure 3.3.

The selection of experimental FFs were guided by successful tests from the literature [39], [70]. Therefore heat sinks with fractions of 0.28 to 0.50 were also used.

Figure 3.3: Picture of example heat sink in square array with lattice constant a = 4.44 mm

Table 3.2 outlines the geometric properties of all the heat sinks used in the experimental investigation. All samples are denoted using HS_1 to HS_4 representing the four different filling fractions with subscripts S for short sized and L for long sizes. All samples had a height values of 12 mm.

Table 3.2: Heat Sink Geometries

Heat Sink	Sink Length (L) mm	Sink Width (W) mm	Inclusion Diameter (d) mm	Lattice Constant (a) mm	Radius Ratio (r/a) mm	Filling Fraction (FF) mm	Number of Periods
HS1S	25.4	25.4	1.69	3.51	0.24	0.18	5
HS1L	30.5	25.4	1.69	3.51	0.24	0.18	9
HS2S	25.4	25.4	3.17	5.28	0.30	0.28	4
HS2L	38.1	25.4	3.17	5.28	0.30	0.28	8
HS3S	25.4	25.4	3.17	4.44	0.36	0.40	5
HS3L	38.1	25.4	3.17	4.44	0.36	0.40	8
HS4S	25.4	25.4	3.17	3.96	0.40	0.50	5
HS4L	38.1	25.4	3.17	3.96	0.40	0.50	8

3.2.3 Piezoelectric Ceramics

With knowledge about the materials to be used for the formation of the bandgap, the desired frequency range can now be estimated for given dimensions.

The desired frequency range can now be estimated for given dimensions with

knowledge about the materials to be used for the formation of the bandgap. For a hand-held specimen in the low centimeter dimension range, calculations showed the range of operation to be in the low to mid kilohertz frequency range (further explained in Chapter 4). A suitable transducer that was capable of this frequency range and comparable in length dimensions to the specimen face was then selected. Example research from the literature that conducted similar experiments used circular transducers that were within the magnitude of the experimental lattice constant and signals were averaged over different transducer positions on the ABG material face [39]. Rectangular transducers were selected for this research to induce displacement waves throughout the entire face of the bulk specimen.

Plate transducers with dimensions of 25.40 mm in length, 12.20 mm in width, and 3.05 mm in thickness were used. The material of the transducer is made of a synthetic quartz, known as Zirconate Titanate (PZT). The specific PZT (commercially known as APC 850) is typically used for low power resonance devices when high coupling and/or high sensitivity is needed (e.g. pressure sensors, microphones) [75]. A thin film of silver on the polarity sides of the crystal allowed for soldering connections. The mode of vibration in the thickness direction was used in this investigation. The equation representing the total change in the thickness direction of the ceramic element Δh is shown in Equation 3.1 as a function of the piezoelectric charge constant, d_{33}, and the applied voltage, V. The voltage limit for the ceramic element used is 8 V/mil for yielding an output voltage of about 20 $watts/in^2$ [75].

More material properties of the type of PZT used are listed in Table 3.3. The Curie point designates twice the maximum operating temperature, the piezoelectric charge constant relates the strain to applied voltage, the voltage constant is the electric field generated per stress applied, and the frequency constants are the resonant frequency multiplied by the respective mode dimensions. Subscripts indicate directional properties with respect to polarization. For example, d_{33} indicates induced

strain in direction 3 per unit electric field applied in direction 3 (direction 3 is parallel with the direction of polarization), d_{31} indicates the induced strain in direction 1 (perpendicular to polarization) per unit electric field applied in direction 3, and d_{15} is the induced strain in direction 2 (perpendicular to polarization) per unit electric field applied in direction 1 (See Figure 3.4). The relation to find the resonant mode in the thickness direction is given in Equation 3.2 where f_s is the series resonance, N_T is the frequency constant in the thickness direction and h is the height of the ceramic. The measuring frequency range should be below the series frequency to avoid resonant effects in the results readings. The same resonances can be found for the longitudinal and axial mode frequencies using their respective dimensions and frequency constants.

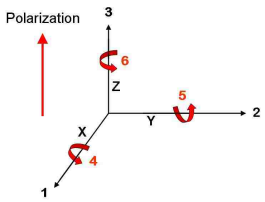

Figure 3.4: Orientation of PZT material properties from Table 3.3

$$\Delta h = d_{33} V \tag{3.1}$$

$$N_T = f_s h \tag{3.2}$$

Table 3.3: Piezoelectric properties of APC 850 PZT [75]

Relative Dielectric Constant	K_T			
	1750			
Dielectric Dissipation Factor (%)	$tan\delta$			
	1.4			
Curie Point (Deg C)	T_c			
	360			
Electromechanical Coupling Factor (%)	k_p	k_{33}	k_{31}	k_{15}
	0.63	0.72	0.36	0.68
Piezoelectric Charge Constant (10^{-12} C/N or m/V)	d_{33}	$-d_{31}$	d_{15}	
	400	175	590	
Piezoelectric Voltage Constant (10^{-3} Vm/N or m^2/V)	$-g_{31}$	g_{15}		
	12.4	36		
Young's Modulus (10^{10} N/m)	Y_{11}	Y_{33}		
	6.3	5.4		
Frequency Constants (Hz·m or m/s)	N_L	N_T	N_P	
	1500	2032	1980	
Density (10^3 kg/m^3)	ρ			
	7.7			
Mechanical Quality Factor	Qm			
	80			

3.3 Sample Preparation and Experimental Setup

3.3.1 Sample Preparation

The goal in fabricating the specimens was to create near geometrically-identical specimens by size with respect to inclusion specimens and pure matrix specimens with no inclusions in order to provide uniformity in testing methods. Three different sizes were fabricated out of the four different specimen filling fractions and the two host materials (elastomer and epoxy) summarized in Table 3.4. The fabrication process had slight variations for the two different host types to achieve uniform specimens. The fabrication process for the elastomer and epoxy specimens follow:

Table 3.4: Specimen Properties Overview

		Width (mm)	Length (mm)	Height (mm)	Mass (g)
Elastomer					
	HS1S	25.5	25.6	15.2	26.4
	HS2S	25.7	25.8	14.9	29.8
	HS3S	25.6	25.7	15.6	28.6
	HS4S	25.6	25.6	14.8	30.2
	HS1L	25.5	32.3	14.6	31.8
	HS2L	25.4	32.7	15.2	36.0
	HS3L	25.6	36.1	15.1	33.1
	HS4L	25.4	32.5	15.6	36.9
Epoxy					
	HS1S	24.5	24.5	11.0	24.5
	HS2S	24.0	24.5	11.2	26.2
	HS3S	23.9	24.0	11.3	25.2
	HS4S	23.8	24.0	11.2	26.1
	HS1L	24.7	31.3	11.6	28.3
	HS2L	23.4	35.1	12.4	31.7
	HS3L	23.4	35.6	11.5	29.4
	HS4L	23.8	35.6	11.2	31.6

Process for Fabrication of the Elastomer Specimens:

1. Prepare the L-clamps (Figure 3.5) on the Plexiglas plate (75 x 125 mm) at the desired length and clamp the L-clamps to the plate. (Ensure a tight connection between space where L-clamps meet)
2. Place the two transducers on each side of the void made by the inside of the L-clamps.

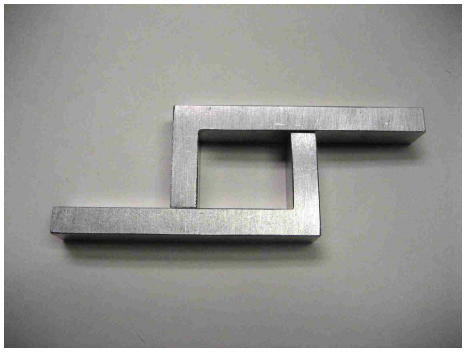

Figure 3.5: Picture of milled L-Clamp to be used as casing for sensor fabrication

3. Unscrew the cap by removing the metal top piece from the elastomer dispenser then remove the green stopper.

Fit the nozzle on the dispenser and screw the top cap back on (ensuring that the nozzle is properly fit).

4. Place elastomer dispenser in the dispensing gun and slowly fill the void within the L-clamps to about 2/3 of the volume with the mixed elastomer components.

5. Agitate the holder for about one minute and then place the assembly in the vacuum (Figure 3.6).

6. Repeatedly allow the vacuum state to be evacuated from the chamber (provides control by popping air bubbles

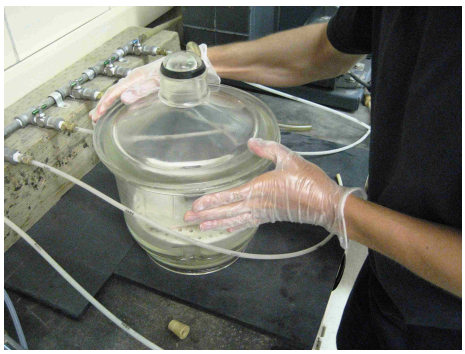

Figure 3.6: Picture of elastomer specimen in vacuum chamber

within and not allowing for overflow). Allow for evacuation more frequently (every 5 seconds) at beginning and less frequently over time (up to about 8 minutes).

7. After 30 minutes, remove the assembly from the vacuum chamber.

a. If making pure matrix fill remaining volume with elastomer and allow slight excess on top held by surface tension (to account for some volume loss). Return to vacuum.

b. If making an inclusion specimen, fill volume leaving 1-2 mm open. Then place heat sink with the inclusions facing downward into the elastomer volume (base on top) and return the assembly to the vacuum.

8. Leave elastomer in the vacuum for 3-4 hours or when all visible air bubbles are removed under normal pressure state. *Note: Non-visible air pockets become visible during vacuum phase.

9. Once removed from vacuum, allow to sit for 20 minutes then place in oven at 105 ^{o}C for 10 minutes.

10. Allow at least one day after removal from oven to ensure a full cure. If pure matrix skip to step 14, else place the specimen in the cutting frame. Adjust the specimen so that the transducers are planar with the inside edge of the blade void of the cutting frame and tighten the frame until there is no slip. Use foam if necessary. Over-tightening will cause bending of the specimen. Ensure that the inclusions are parallel with the top of the cutting frame(Figure 3.7).

11. Screw cutting frame in the Isometric saw. Check to see if the blade is in contact with the liquid coolant bath below. Adjust blade manually to be planar with the blade void of the cutting frame closest to the transducers.

12. Close saw lid and turn blade on to speed 100 rpm. Lower saw arm and begin cutting until the blade goes fully through the specimen(Figure 3.8).

13. Remove cutting frame and specimen from saw and remove specimen from cutting frame and allow specimen to dry for about 1 day. 14. Cut small slices of elastomer off the four inner corners of the specimen and remove any elastomer that may be on the outside upper corners of the transducers.

15. Scratch off the oxidized layer of the transducer to expose the silver layer of the crystal at one end on each of the inner sides of the transducer where the elastomer piece was removed and at the opposite side of other side of each

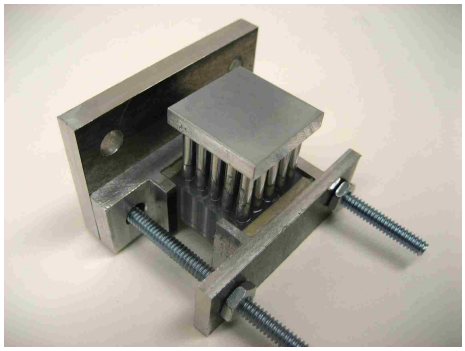

Figure 3.7: Picture of inclusion specimen being set-up in aluminum cutting frame

Figure 3.8: Isometric saw used to cut specimens

transducer.

16. Solder on a 1.5 lead to each of the scratched areas. Verify that the connection is good by checking with a voltmeter (aim 0.3 ohms).

Process for Fabrication of the Epoxy Specimens:

1. Prepare the L-clamps on the Plexiglas plate (75x 125 mm) at the desired length and clamp the L-clamps to the plate. (Ensure a tight connection between space where L-clamps meet)

2. Apply a 0.5 mm layer of vacuum grease throughout the void made by the inside of the L-clamps (for removal of specimen later).

3. Use 10 mL syringe to obtain proper volume of epoxy resin and place in small glass contained with wide opening. Using a different syringe, obtain 1/3 the amount of resin used of hardener and place in the same glass container. Mix the two components together slowly to minimize air bubbles introduced for 2 minutes or until there does not appear to be marbleized effects.

4. Using another syringe, transfer the epoxy to the greased open volume made by the L-clamps until full (leave 1-2 mm from top if inclusion specimen).

5. Agitate the holder for about one minute and then place the assembly in the vacuum.

6. Repeatedly allow the vacuum state to be evacuated from the chamber (provides control by popping air bubbles within and not allowing for overflow). Allow for evacuation more frequently (every minute) at beginning and less frequently over time (up to about 30 minutes).

7. After 30 minutes

a. If making pure matrix, ensure volume is still completely filled.

b. If making an inclusion specimen, place heat sink with the inclusions facing downward into the epoxy volume (base on top) and return the assembly to the vacuum(Figure 3.9).

8. Leave epoxy in the vacuum for 2-4 hours or when all visible air bubbles are removed under normal pressure state.

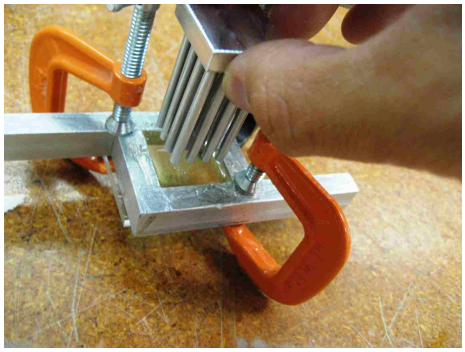

Figure 3.9: Picture of placing heat sink into epoxy mold

*Note: Non-visible air pockets become visible during vacuum phase.

10. Once removed from vacuum (Figure 3.10), allow to sit for 20 minutes then place in oven at 105 ^{o}C for 5 minutes (over-curing will cause redness to occur).

11. Allow at least one day after removal from oven to ensure a full cure. If pure matrix skip to step (15), else

Figure 3.10: Picture of epoxy specimen being removed from greased L-Clamps

place the specimen in the cutting frame. Adjust the specimen so that the top of the epoxy portion of the specimen is planar with the inside edge of the blade void of the cutting frame and tighten the frame until there is no slip. Use foam if necessary. Over-tightening may cause bending of the specimen. Ensure that the inclusions are parallel with the top of the cutting frame.

12. Screw cutting frame in the Isometric saw arm. Check to see if the blade is in contact with the liquid coolant bath below. Adjust blade manually to be planar with the blade void of the cutting frame closest to the transducers.

13. Close saw lid and turn blade on to speed 250 rpm. Lower saw arm and begin cutting until the blade goes fully through the specimen.

14. Remove cutting frame and specimen from saw and remove specimen from cutting frame and allow specimen to dry for about 1 day.

15. Using the wet sander, sand the specimens to designated sizes and intend for flat, perpendicular edges.

16. File the four corners of the specimen to remove about 1-2 mm of depth and width.

17. Scratch off the oxidized layer of the transducer to expose the silver layer of the crystal at one end on each of the one side of the transducers and at the opposite side of other side of each transducer.

18. Solder on a 1.5 lead to each of the scratched areas. Verify that the connection is good by checking with a voltmeter (aim 0.3 ohms).

19. Repeat step (3) and use epoxy to adhere transducers to epoxy specimen. Place heater nearby for faster curing

(2 days).

A great deal of care was taken to create the maximum amount of uniformity among the specimens. This included designing and implementing consistencies in dimensions, material makeup, and adhesion to the transducers. Uniformity among the specimens allow the controlled variables to emerge in the results therefore making it possible to draw direct correlations. It was also imperative that each transducer be placed on the specimen face perpendicular to the direction of propagation and parallel to the opposing transducer.

3.3.2 Test-Setup

The intention of the experiment is to evaluate the ability of the ABG specimen to hinder elastic wave propagation under a specific frequency range and the significance of periodicity disturbance on the ability. A schematic representation of the test set-up is shown in Figure 3.11. A test frame was constructed to provide uniformity in testing conditions and to optimize overall response of the ABG material. The test frame was made with the intention to provide support on both sides of the specimen with minimal obstruction to the transducer or received signal. It was later determined that the test frame enabled producing compressive and tensile strains in the ABG specimen as see in Figure 3.13.

The test frame was made of 1 mm thick Aluminum C-channels and a lead C-clamp (Figure 3.12). The C-clamp was suspended from the middle C-channel and four legs were glued to two lateral channels that supported the middle C-channel. Four round aluminum bases were attached to the legs for enhanced stability. All connections were initially glued, but nuts, bolts, and U-rings were added later to provide rigidity and cohesion among the components. An array of soft and non-conductive materials

were placed on each side of the C-clamp to reduce any possible current flow through the structure linking the transducers electrically rather than mechanically and also providing the soft support to the specimen. The array of soft materials was made up of a thin piece of cork board, insulating rubber, and fiberglass wool.

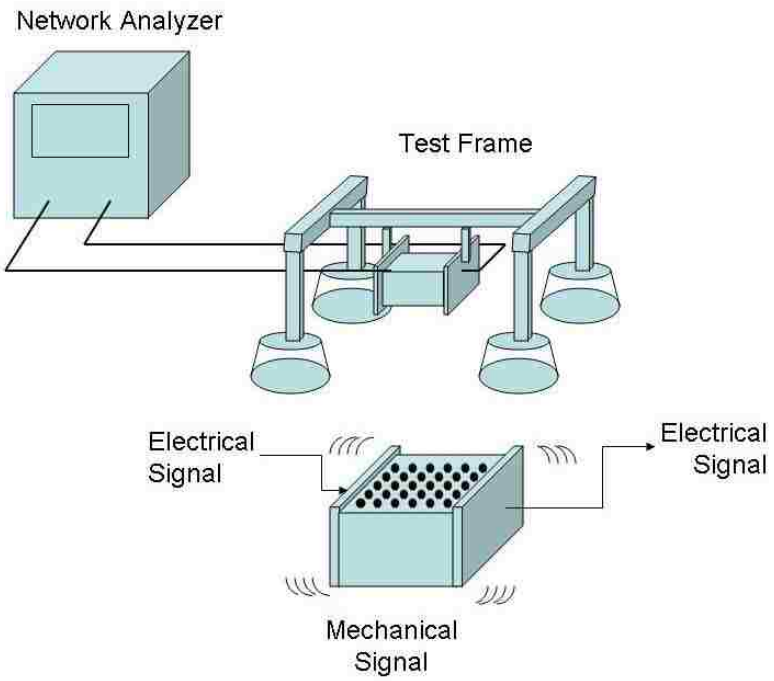

Figure 3.11: Schematic representation of test setup including the network analyzer and the ABG test frame

The equipment used to obtain the transmission data was an HP 8753D Option 011 network analyzer with a 85046A S-parameter test set seen in Figure 3.14. A network analyzer is used to measure the scattering parameters (S-parameters) of an electrical system. The type of network analyzer that was used in these experiments is called a vector network analyzer (VNA) or gain-phase analyzer which measures both amplitude and phase properties. The S-parameters represent the reflection and transmission of an electrical network. For example S_{12} and S_{21} is the transmission coefficient of a network in a 2-port system and the two quantities are equal for a

Figure 3.12: Picture of ABG Test-Bed Structure

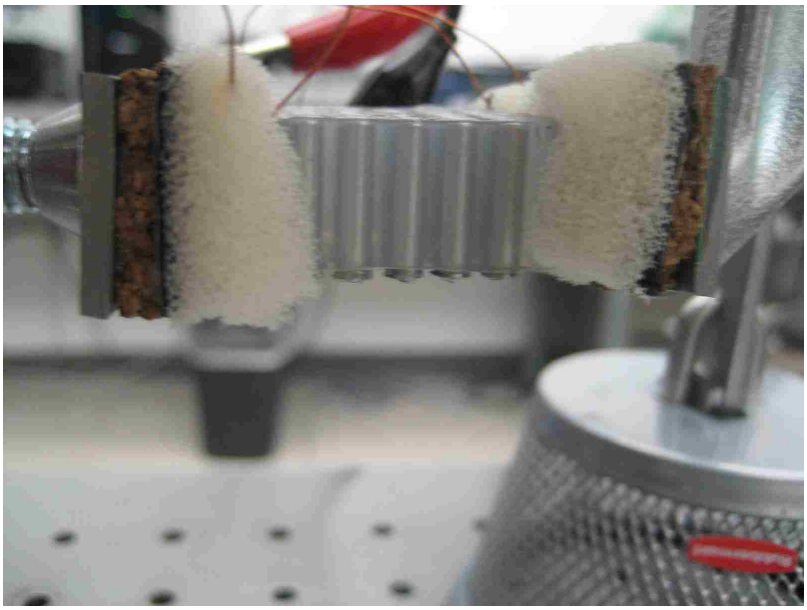

Figure 3.13: Picture of ABG sensor being compressed in Test-Bed Structure

reciprocal network. The transmission coefficient is the complex linear gain found by dividing the output voltage of the measured network by the input voltage.

Figure 3.14: Picture of network analyzer and S-parameter test set

The experiments here will involve the transmission coefficient, although our network is not electrical. The network was made up of dielectric materials and the intention was to evaluate the propagation of elastic waves in the dielectric material under various frequencies. The network analyzer used adaptors, coaxial cables and crocodile clips to connect to leads soldered onto the piezoelectric transducers. The transducers have the task of converting the electrical signal into an analogous mechanical displacement wave. This process is called the inverse piezoelectric effect. The transducer on the opposing side of the mechanical network (ABG material) is utilized through the piezoelectric effect where induced displacement (strains) generate voltages with opposite polarity [75]. With an electrical signal again, the scattering parameters can be measured.

Calibration was necessary to increase the measurement accuracy of the network analyzer results. Common errors in measurements include sources such as connector

repeatability, lossy cables, temperature and frequency drift and leakage. Calibration can effectively remove some of these errors, specifically the systematic errors that are repeated such as those caused by mismatch, leakage, and system frequency response [76]. This type of error correction is done through the use of measurement standards which mathematically updates the network analyzer system. The standards used for this experiment consisted of the 85032E N-Type calibration kit. A full two-port calibration was conducted for measurement of the transmission of the ABG material network.

Our experiments examined the transmission of the elastic wave through various frequencies by analysis of the electrical response. The network analyzer makes sweeps through the user-defined frequencies and a transmission response is determined for each frequency within this frequency band. Measurements were taken over two frequency ranges. First from 100 kHz to 350 kHz, the maximum of 1601 points was taken for a sweep to optimize accuracy. The second range, from 30 kHz (S-Parameter test set minimum) to 800 kHz, was wider than the first to capture any events that may occur after the targeted range such as second mode gaps. The high sampling rate is important to avoid aliasing, which can occur if sampling above the Nyquist Frequency. The Nyquist Frequency is a maximum frequency value dictated by sampling rate. If the sample rate is too low, aliasing may occur which hides true amplitude results by taking too few sample points from a sinusoidal output in the time domain.

The network analyzer sends and receives sinusoidal voltage pulses which are then converted to readings within the frequency domain. Sinusoidal displacement impulses are then created through the piezoelectric crystals and translated to the sample materials. The resulting frequencies create particle movement in a variable range of wavelengths through the materials. When the acoustic waves approach wavelengths with the same order of magnitude as the lattice constant, there exists a point of

maximum reflection due to the scatterers with high acoustic impedance contrast, thus causing the wave transmission response for the corresponding frequencies to drop.

3.4 Results

The following results are divided into two sections. The first section presents the results for the specimens with an elastomer host. The second section presents the results for the specimens with an epoxy host. The experiments conducted were done under three conditions. The first condition was tested to model an ABG sensor adhered to a substrate in a healthy state in which the specimens were under 'no-strain'. The test-frame was simply used to support the specimen with minimal pressure. Next, the ABG specimens were placed under uniform tension and compression using the test-frame. The uniform compression was achieved by simply tightening the C-clamp and creating a deformation in the length of the specimen. A similar process was carried out by compressing the side-faces (specimen rotated 90 degrees around inclusion axis) to create an indirect tensile strain through the elongation of the specimen. Lastly, non-uniform strain was achieved for the tension condition by making a cut of depth 15 percent of the height into the specimen along the inclusion axis and applying the same side pressure as for the uniform tension case.

Specimens with no inclusions were made of each host material with the same dimensions and tested in the same fashion as a control and to act as a normalization base for the inclusion-filled sample's results. Each inclusion specimen's transmission results was normalized by the transmission results for the pure matrix specimen with the corresponding host material and size dimensions. This procedure, which is referred to as normalization, effectively enabled removing amplitude biases that may occur and helped in locating the acoustic bandgap. This will be demonstrated in

the elastomer section of the results. In addition to normalization, each specimen's response is averaged over four tests for each condition state. By averaging responses over different testings for each specimen, environmental effects were eliminated minimizing the significance of noise, temperature, humidity effects, and test equipment variations.

3.4.1 Elastomer Host: Results and Discussion

For the experiments consisting of specimens with an elastomer host, the expected bandgaps dictated the frequency sweep range to be between 10 kHz (the network analyzer minimum) to 350 kHz. An intermediate frequency (IF) bandwidth of 30 kHz was used to reduce the noise floor in the receiver input. A maximum of 1601 points was used over the 240 kHz span. The data output from the network analyzer is given in terms of the transmission coefficient (unitless) for each frequency step as shown in Figure 3.15. This figure presents the transmission for a specimen with an elastomer host containing aluminum cylindrical inclusions in a square array with a filling fraction of 0.40 and the transmission response for the corresponding host matrix specimen which is made of the same dimensions and host material, but contains no inclusions.

It is evident that there is difficulty in quantifying the difference in the inclusions and matrix responses at low transmission values. Low transmission values prove meaningful in isolating a bandgap, therefore a logarithmic scale is used for the y-axis to provide more detail to these lower values. Decibels (dB) are assigned to the y-axis which are used as a measure of magnitude with respect to a reference quantity. In cases such as amplitude, voltage, and current, decibels are found using Equation 3.3

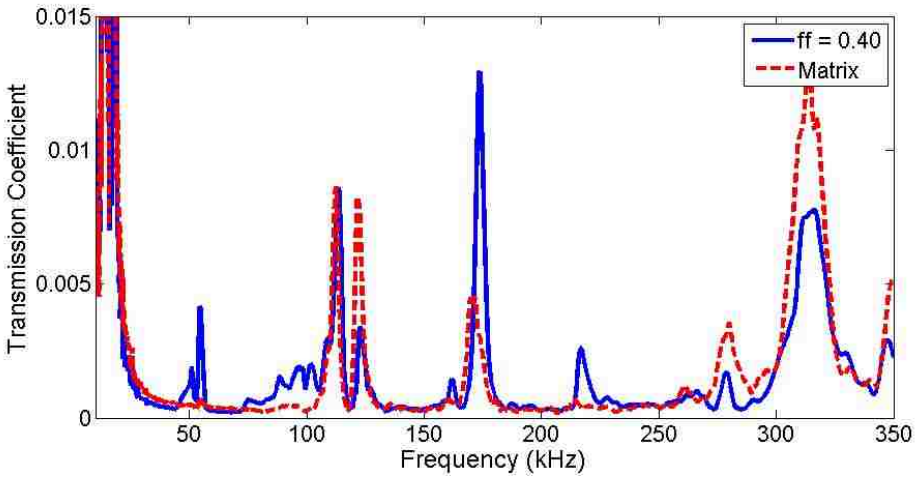

Figure 3.15: Averaged transmission coefficient for elastomer specimens with FF = 0.40 (Solid) and elastomer matrix (Dashed)

using a reference quantity A_0 where A is the measured value.

$$20 * log_{10}(\frac{A}{A_0}) \tag{3.3}$$

Here, decibels are used in the same way to express amplitude based on voltage input and output given as the transmission coefficient. Figure 3.16 uses the same data as in Figure 3.15 but using decibels to show a more descriptive representation of the lower transmission values.

Acoustic bandgaps appear as regions of low transmission representing the fact that elastic waves are prohibited within designated frequency zones. A bandgap, being indicative of the periodicity of the inclusions with differing impedance, is thus an attenuated region in transmission with respect to the matrix response. One more processing step can further enhance the representation of bandgaps by utilizing the idea that a bandgap a region of low transmission in reference to the signal that would be passed without the scatterers present. To improve the representation of relative transmission response of the inclusion specimens with respect to the matrix

specimens, a normalization of the data is performed. The normalization quantity is found by dividing the transmission coefficient function of the inclusion specimens by the transmission coefficient function of the matrix specimens as described above. The normalized transmission response of the cases above is shown in Figure 3.17. It can be seen that low transmission responses in the inclusion specimens with respect to the matrix response are more easily perceived. It appears as though there are two gaps present at about 120 kHz and 170 kHz, although these are not bandgaps for reasons that will be addressed shortly.

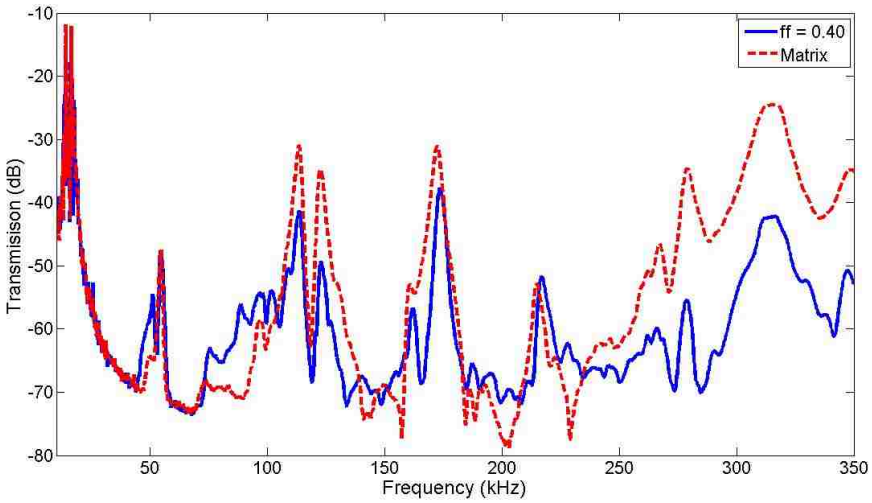

Figure 3.16: Averaged transmission in dB for elastomer specimens with FF = 0.40 (Solid) and elastomer matrix (Dashed)

Figure 3.18 shows the signal responses for an experimentally modeled healthy case substrate with the filling fractions 0.18, 0.28, and 0.50. The healthy case signifies no induced strain to the sensor. It can be seen that each filling fraction produces similar transmission drops around the same area as for FF = 0.40 at about 120 kHz and 170 kHz. For filling fractions with different lattice constants, bandgaps should occur at different frequencies where the center frequency is inversely proportional to lattice constant 'a'. More tests results are shown in Figures 3.19 and 3.20 for sensor

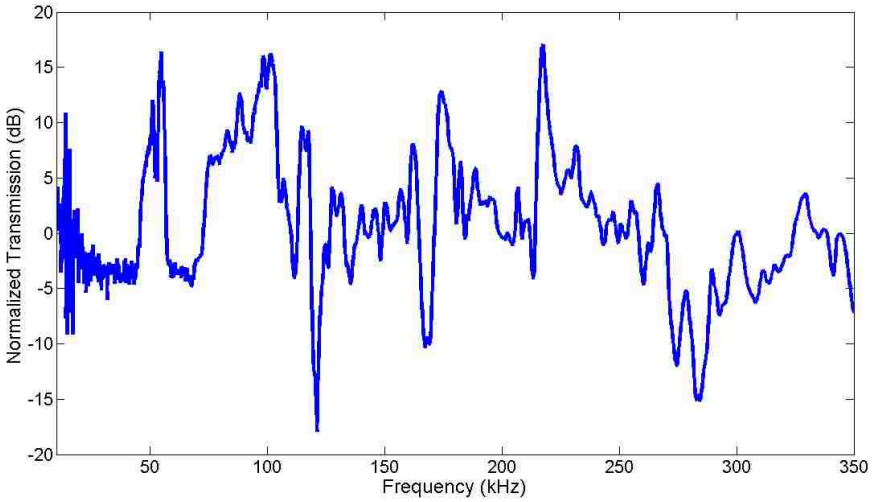

Figure 3.17: Averaged normalized transmission in dB for elastomer specimens with FF = 0.40

specimens subjected to compressive and tensile strains. In both figures, the gaps seem to widen for compressive strains and become slightly thinner for tensile strains. It can also be seen that the compressive strains produce a small shift leftward toward the lower frequencies. The higher attenuation for the compressive and tensile cases throughout the frequencies measured may be attributed to the tighter boundaries being applied to achieve these strains. The boundaries undoubtedly cause more damping throughout the system as the signals are more likely to travel through the now stiffer mediums.

Overall, a bandgap could not be pinpointed for the elastomer host for the test cases run. Although it does appear that bandgaps are present at 120 kHz and 170 kHz, this is the result of high peaks that occur for the matrix specimens thereby reducing the signal transmission when normalization takes place. The occurrence of the same bandgap frequency for each filling fraction displays the erroneous nature of the gap. In fact, the matrix specimens only had transmission at various high transmission regions and had very low transmission otherwise. The inclusion speci-

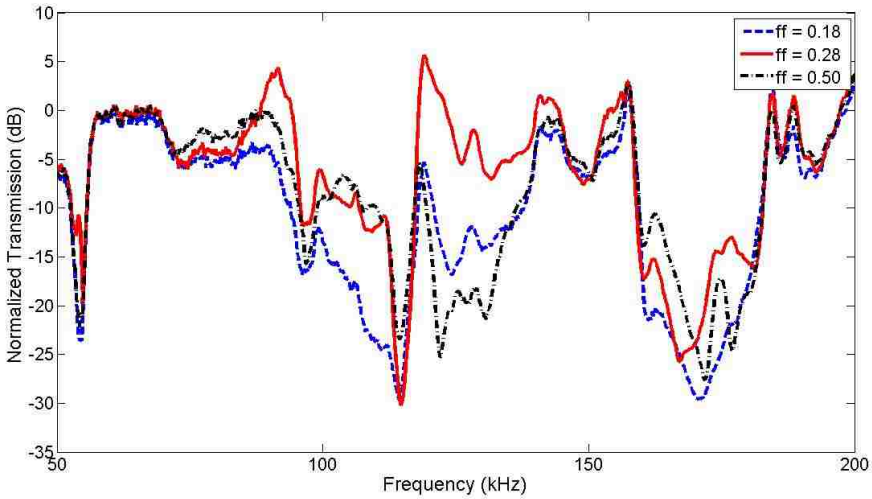

Figure 3.18: Averaged normalized transmission in dB for elastomer specimens with FF = 0.18 (Solid), FF = 0.28 (Dashed) and FF = 0.50 (Dot-Dashed)

mens naturally have more attenuated responses due the metal inclusions and higher scattering of waves, which has a greater effect as frequency increases. Therefore, all that could be detected was lack of transmission throughout the frequency region, and the dips were due to the matrix specimen peaks. For this reason, normalization can be misleading as the perceived gaps in normalized transmission seen in Figures 3.18 through 3.20 point to lack of transmission in the inclusion cases where the matrix specimens were able to have some transmission.

Although elastomers offer great advantages in terms of strain mobility to easily take on substrate behavior, they are also hindered with low transmissibility. This was a concern from the start as rubbers are well-known for their vibration absorbability and their many applications as dampers. In conclusion, the results do not necessarily show that bandgaps cannot be found for elastomers of filling fractions 0.18, 0.28, 0.40, and 0.50. Bandgaps may be present within the signal responses, yet the level of attenuation of the matrix and inclusions specimens is too high to depict a bandgap profile for the given experiments. In order to more accurately test elastomers as a

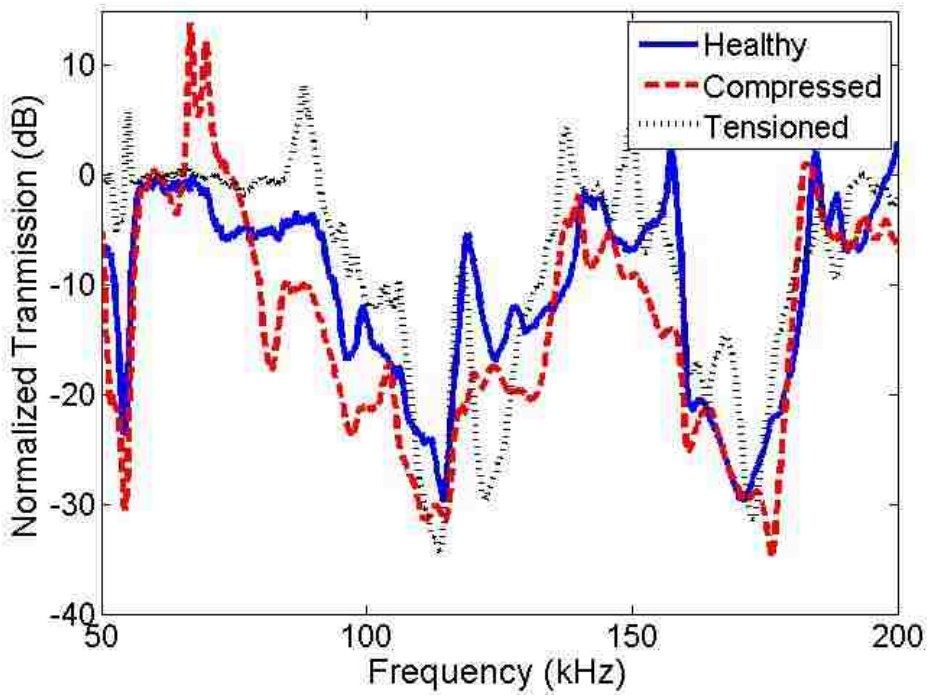

Figure 3.19: Averaged normalized transmission in dB for elastomer specimens with FF = 0.18 under healthy conditions (Solid), compressed conditions (Dashed) and tensile conditions (Dotted)

host material, the vibration amplitude to material size ratio needs to be higher to have less energy dissipation due to the viscoelastic effects of the elastomer matrix. A smaller specimen with the same displacement amplitude may allow for a stronger signal to propagate throughout the resulting lower frequency range to be used (due to lower lattice constant). Also, the same size specimen with greater displacement may also be easily implemented with the installation of different transducers.

3.4.2 Epoxy Host: Results and Discussion

The same process to achieve transmission in decibels and normalized transmission in decibels is carried out for the epoxy case. Figure 3.21 shows the difference between

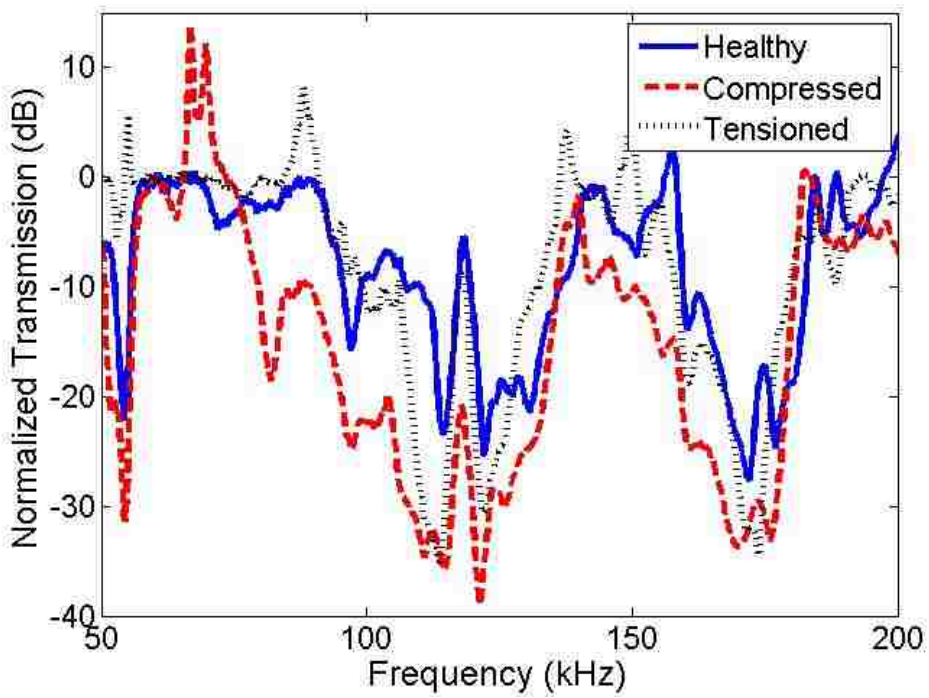

Figure 3.20: Averaged normalized transmission in dB for elastomer specimens with FF = 0.50 under healthy conditions (Solid), compressed conditions (Dashed) and tensile conditions (Dotted)

the minimal, no-transmission case in which the output channel is totally detached from the input channel in a scenario called 'Open' and the averaged long matrix specimen case. There is more transmission for the epoxy hosts and room for attenuation to be detected at most points throughout the search region than for the elastomer hosts.

Figure 3.22 and Figure 3.23 show the healthy-case transmission responses for specimens HS1L. Figure 3.22 is the wide view response for HS1L from 50 kHz to 700 kHz along with matrix specimen M2. Figure 3.23 shows a tighter view isolating the area of interest where the bandgap should be located. Arrow pointing downward spot two possible gaps in range of calculated values at slightly over 250 kHz and 290

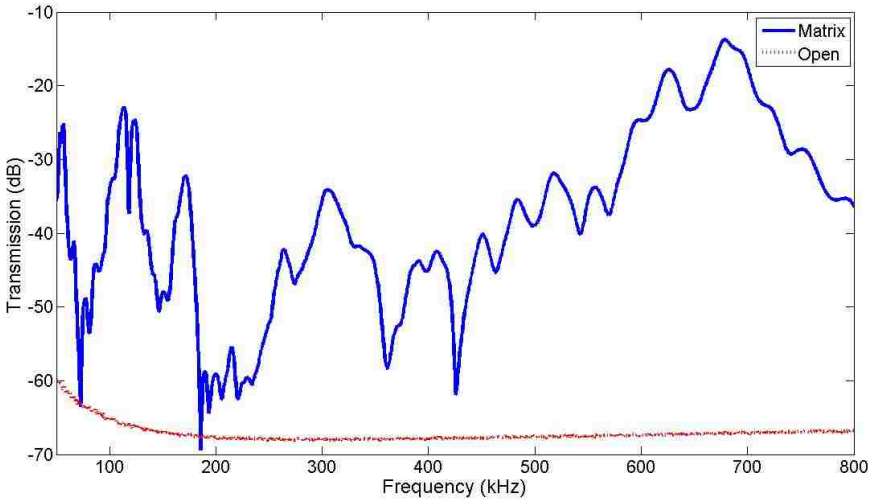

Figure 3.21: Averaged transmission in dB for long and short epoxy matrix (Solid) and open channel in which no transmission occurs (Dashed)

kHz. Because the Bragg resonance is capable of producing a gap for the inclusions parallel to the direction of wave propagation as well as in the diagonal (45 degrees) direction for a square lattice, two gaps are considered. Further investigation upon normalization can more objectively reveal attenuation gaps as seen in Figure 3.24. Although the response at the higher frequency range of Figure 3.23 seems to be heading upward, it can be seen in the normalized plot in Figure 3.24 that the same portion is lower with respect to the rest of the response. This is found in all of the cases upon normalization indicating a downward bias due to loss of transmission upon scattering of the waves. Since the matrix specimens by which the inclusion specimens are normalized do not contain scatterers, the response of the matrix stays consistent, therefore leaving the bias in the normalized responses of the inclusion specimens.

Another possible gap is shown in Figure 3.25. This example shows the normalized averaged response for specimen HS2S with respect to matrix M1. Although it is not as profound as the previous example, it still may be an indication of an ABG. An

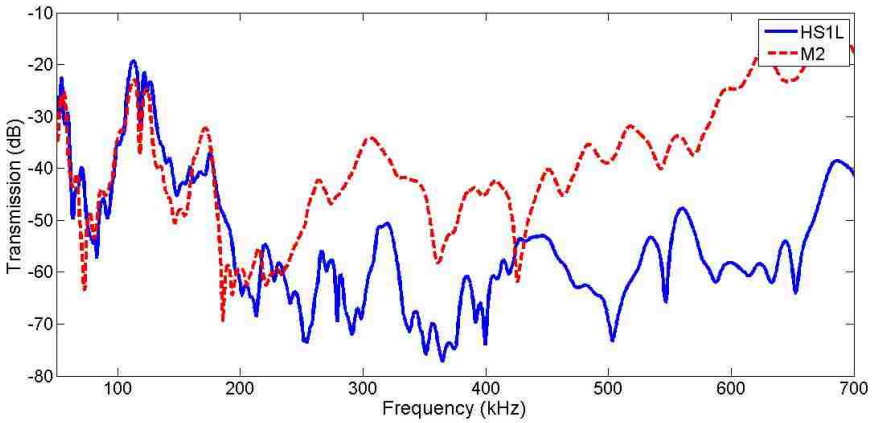

Figure 3.22: Wide view of average transmission response for HS1L specimen of FF = 0.18 (Solid) and M2 matrix (Dashed)

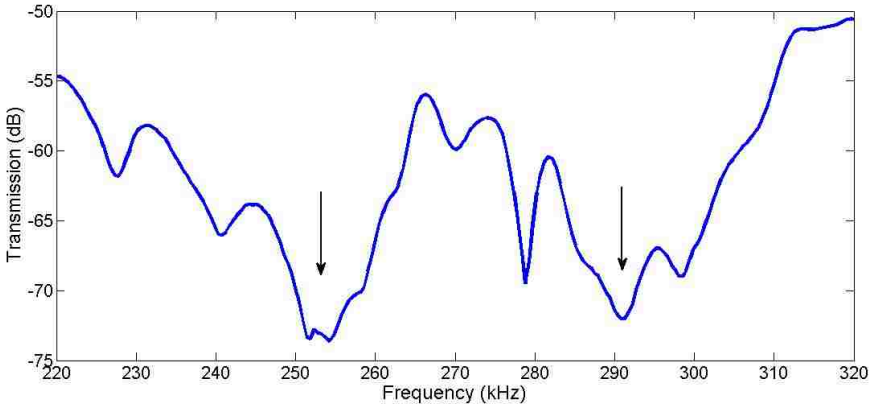

Figure 3.23: Tight view of average transmission response for HS1L specimen of FF = 0.18

accompanying gap for the diagonal Bragg resonance was not found in this case. Again due to scalability, a smaller lattice constant will produce a gap at a higher frequency. Therefore, a specimen with the same inclusion radii, but shorter periodicity than that of HS2S will show gaps at higher frequencies. Specimen HS3S has the same radius as HS2S, but has a 20 percent shorter periodicity yielding expected gaps at a higher frequency. The response for HS3S is shown in Figure 3.26. There appears to

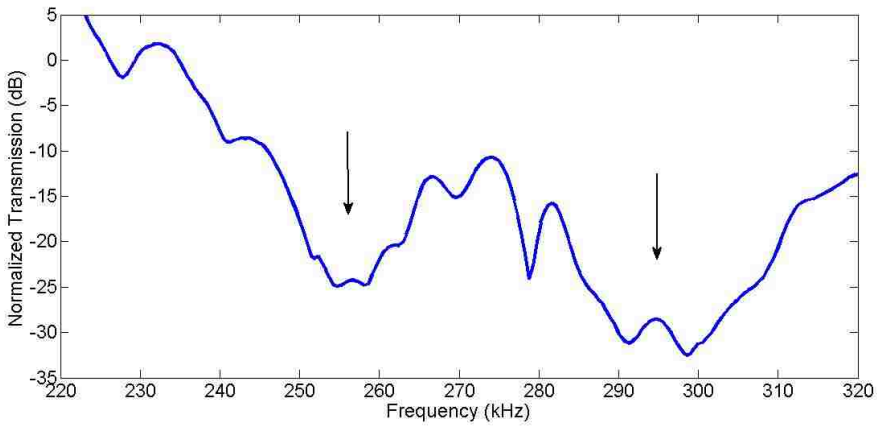

Figure 3.24: Average normalized transmission response for HS1L specimen of FF = 0.18

be two possible gaps around about 245 kHz and 320 kHz.

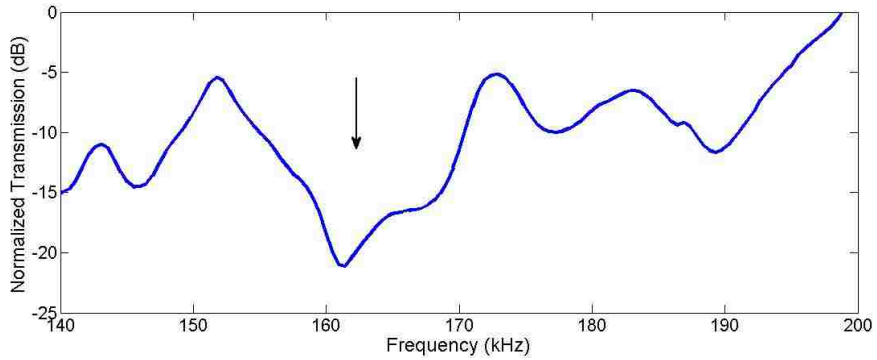

Figure 3.25: Average normalized transmission response for HS2S specimen of FF = 0.28

The last example for the specimens under no strain is for HS4L. A rather wide attenuation band is presented in Figure 3.27. It is expected that higher filling fractions show more pronounced gaps in terms of depth, although in this case, a great amount of attenuation has already occurred due to the high frequency at which the gap is expectedly located. This makes for some difficultly in locating a gap.

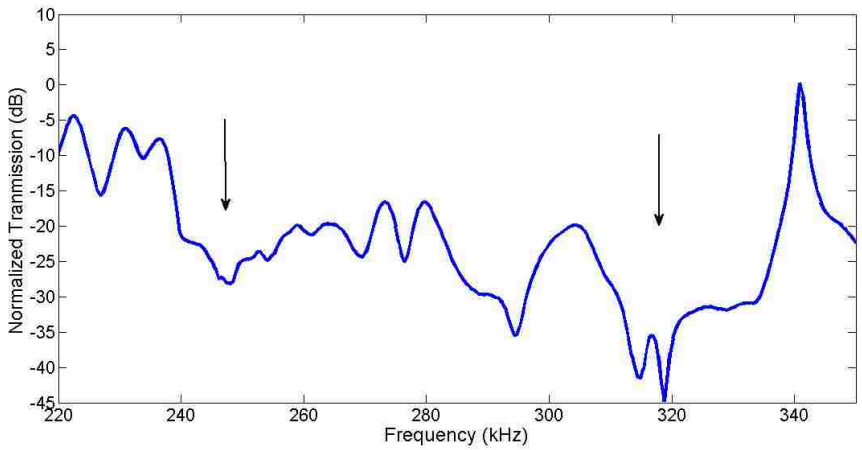

Figure 3.26: Average normalized transmission response for HS3S specimen of FF = 0.40

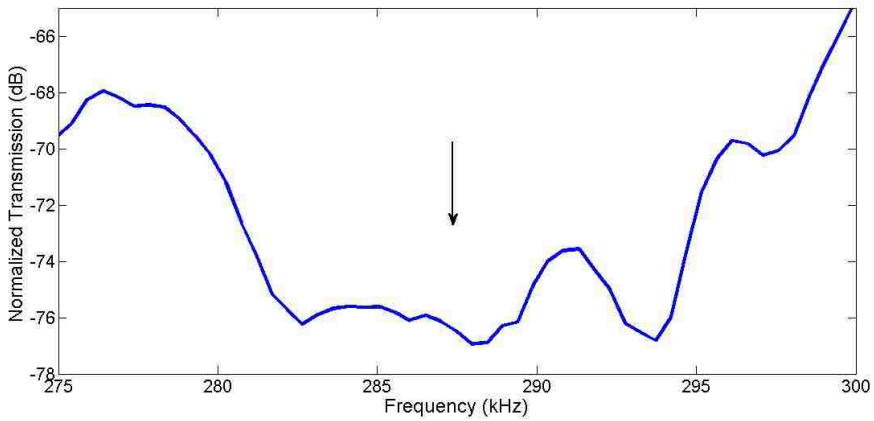

Figure 3.27: Average normalized transmission response for HS4L specimen of FF = 0.50

The specimens were then put under uniform and non-uniform strain conditions to simulate conditions of the underlying substrate. In each case, a strain value of 0.2 milli-strains was attempted and achieved to within 0.05 millistrains. The results for specimen HS1L under uniform compression is given in Figure 3.28. It can be seen that the first gap deepens and narrows, with a possible slight shift toward the

higher frequencies. The second gap experiences some thinning a more clear shift in the same direction. The same specimen under tension is shown in Figure 3.29. Here, a similar change occurs also exhibiting narrowing. The second gap seems to experience the same shift as the compression case, although the first gap may actually seem to show a shift in the opposite direction. For the circumstance that these attenuation bands are functions of the periodicity, a compressive strain would institute a shorter periodicity causing a gap to occur at a higher frequency, thus a shift upward. Inversely, a tensile strain causes an elongation of the periodicity, thus making a shift downward in frequency.

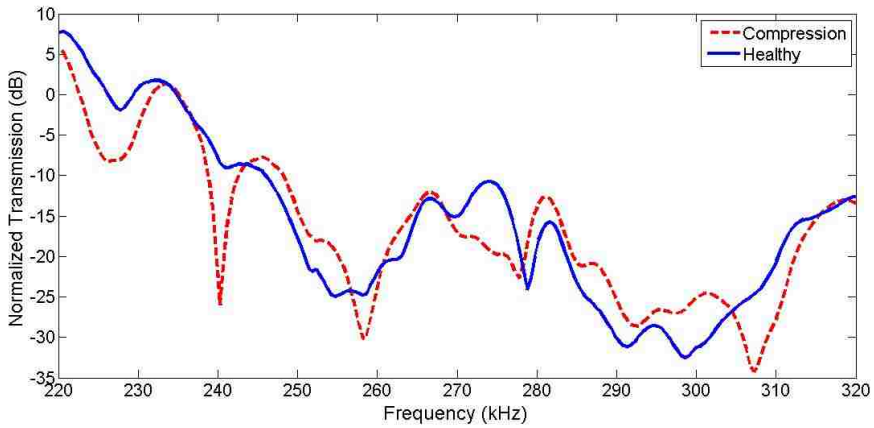

Figure 3.28: Average normalized transmission response for HS1L specimen of FF = 0.18 under healthy conditions of no strain (Solid) and uniform compressive strain of 0.2 milli-strains

Lastly, a non-uniform strain of HS1L is shown in Figure 3.30. Here, an isolated period between the second and third row of inclusions out of nine total rows along the direction of propagation is strained at 0.2 millistrains more than the surrounding rows. Thus, the period between the second and third row of inclusions is greater causing a non-uniform periodicity. The consequences of this occurrence on the normalized transmission response is shown. The first gap raises in transmission indicating less attenuation and widens slightly, while the second gap acts similarly to

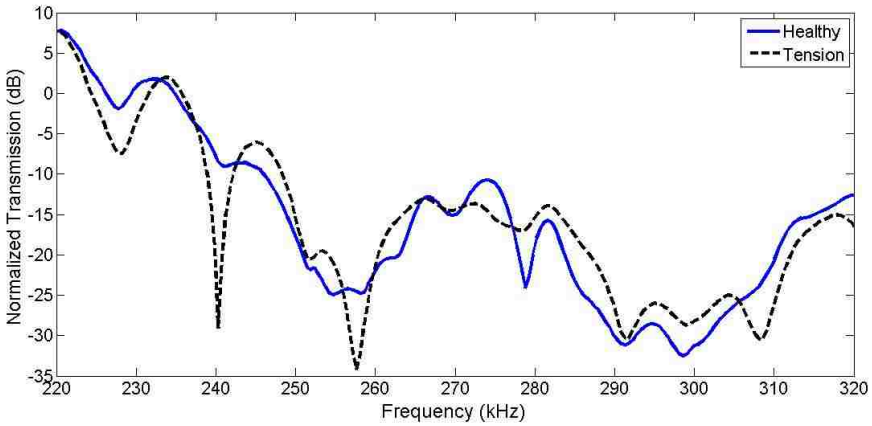

Figure 3.29: Average normalized transmission response for HS1L specimen of FF = 0.18 under healthy conditions of no strain (Solid) and uniform tensile strain of 0.2 milli-strains

the tension and compression cases showing a great value of attenuation at 296 kHz and 309 kHz and a small shift toward the higher frequencies.

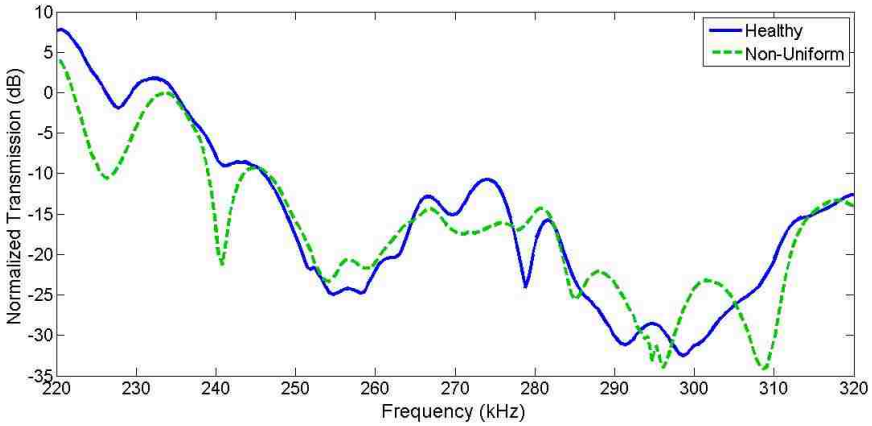

Figure 3.30: Average normalized transmission response for HS1L specimen of FF = 0.18 under healthy conditions of no strain (Solid) and non-uniform tensile strain of 0.2 milli-strains of variation

The is some difficulty in locating bandgaps in the experimental results. This is partly due to high variation in the response which can possibly be attributed to

reflections, although due to consistent profiles of upper and lower regions in various specimen results, the confusion is likely due to the piezoelectric crystal. Therefore there is a great deal of difficulty in determining which attenuation bands are actually the result of the designed periodicity. In spite of various efforts to maximize the emergence of the gaps through averaging and size reflection considerations, the piezoelectric profile is believed to have overridden the results. These results will be re-evaluated when the analytical results are shown and discussed in the next Chapter.

Chapter 4

Analytical Methods

4.1 Introduction

This chapter will cover the analytical methods used in this research that aid to better understand acoustic bandgap engineering. A theoretical method for bandgap prediction is introduced based on Bragg and Mie reflections. In addition, a finite element model was employed in four case studies to test the functionality of ABG materials as sensors. The first three case studies serve as benchmarks to validate the analysis through comparison with ABG experimental results published in the literature. The last case study considers the experiments conducted already addressed in Chapter 3 of this thesis. A parametric study of bandgap performance is shown with the validated model to exhibit bandgap engineering through variation of key material and geometrical parameters. The proposed functionality of ABG sensors is then examined by creating simulated induced uniform and non-uniform strains on an example ABG sensor.

4.1.1 Bragg and Mie Reflections

As discussed earlier, the occurrence of acoustic bandgaps can be attributed to destructive interference caused by reflections within the ABG material. These reflections are the result of elastic waves acting like a phonon, which bound back upon themselves causing a net change in displacement of nearly zero in the ABG material. Bragg reflections are the culprits of this phenomenon in which the scatterers are placed in such a way that the impedance difference causes a rebound between the scatterers primarily in the matrix material. Mie reflections can also play a role (although they are not always present in the literature) by allowing for reflections within the inclusion material. When these two types of reflections coexist at the same frequency range, gaps can be be amplified in strength. A visual explanation of this development is shown in Figure 4.1 by correlating wavelength to reflection occurrence. The reflections are created by destructive interference between the inclusions (Bragg) and within the inclusions (Mie) based on wavelength distance. Wavelength is defined by Equation 4.1

$$\lambda = \frac{C_l}{\omega} \tag{4.1}$$

where C_l is longitudinal speed of sound in a material and ω is frequency in Hz.

Since the reflections can be understood physically, they can also be located in the frequency domain. The frequency locations of the reflections depend on both material and geometrical parameters shown to have significance in the literature such as density, modulus of elasticity, filling fraction, lattice constant, and inclusion diameter. Bragg and Mie reflections center frequency locations (F_B and F_M) are predicted by the Equations 4.3 and 4.4 respectively where the Bragg Velocity (C_B) is calculated using Equation 4.2. The Bragg Velocity is a theoretical quantity calculated as a weighted average of material velocities to describe the behavior velocity of the phonons in the creation of Bragg reflections based on the material makeup of a

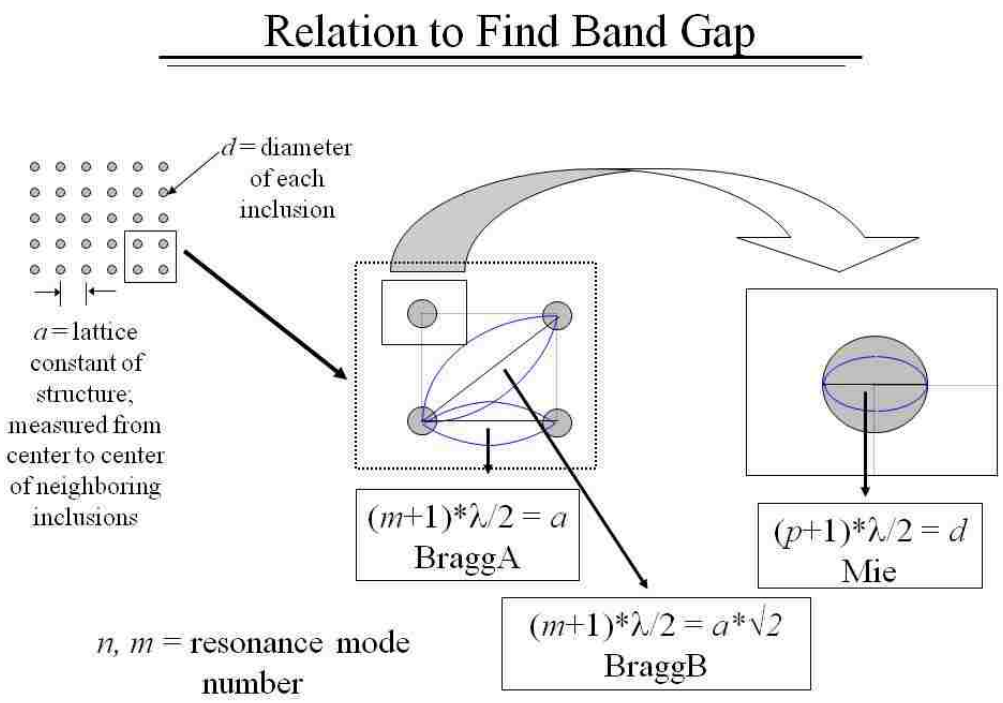

Figure 4.1: Relationship between wavelength, λ, and acoustic bandgap formation using an example square lattice to show reflection modes between inclusions (Bragg) and within inclusions (Mie)

structure, summarized by filling fraction. Constants for host material and scatterer material speeds of sound are C_H and C_S respectively.

$$C_B = C_H \times (1 - FF) + C_S \times FF \tag{4.2}$$

$$F_B = \frac{C_B}{2a} \tag{4.3}$$

$$F_M = \frac{C_S}{2d} \tag{4.4}$$

Design of an ABG crystal can then be structured using Equations 4.2 through 4.4 as a tool to place gap locations in the frequency domain shown in Figure 4.2. Although Bragg reflections A and B are always a fixed scalar multiple apart, there is a dependence on the material's characteristics of impedance mismatch for their corresponding reflection gaps to be wide enough to overlap and merge. For example in a square lattice, there exists a diagonal Bragg reflection mode at the lattice constant multiplied by the square root of two signified in Figure 4.2 by $Bragg_B$. More reflections can exist for different Bravais lattice types with more inclusions within the unit cell to increase the gap quality. Various modes can occur from second and further order reflections denoted as (m) for Bragg reflections and (n) for Mie reflections.

4.1.2 Finite Element Background

The finite element method (FEM) is used in many applications from structural problems that encompass stress analysis in elements such as trusses and frames, buckling analysis, and vibration analysis to non-structural problems such as heat transfer, fluid flow, and electric and magnetic potential distribution [77]. Finite element analysis has also appeared in the literature using harmonic analysis to simulate acoustic band gap materials [63], [78]. The principles of this method are constructed through the discretization of geometries into elements that are made up of nodes. There is an array of element types including linear elements for one-dimensional problems, quadrilateral and triangular elements for two-dimensions, and tetrahedral and hexagonal for three-dimensions. Element types are chosen based on the geometry and type of analysis of the intended model. Element size is also a variable that can be changed to enhance the results of the model. In essence, the finite element functions on the basis of equation 4.5, where $\underline{F}$ is the vector describing the global nodal forces, $\underline{K}$ is the total stiffness matrix, and $\underline{d}$ is the generalized displacement vector made up of known and unknown nodal degrees of freedom [77]. Equation 4.5 relates known

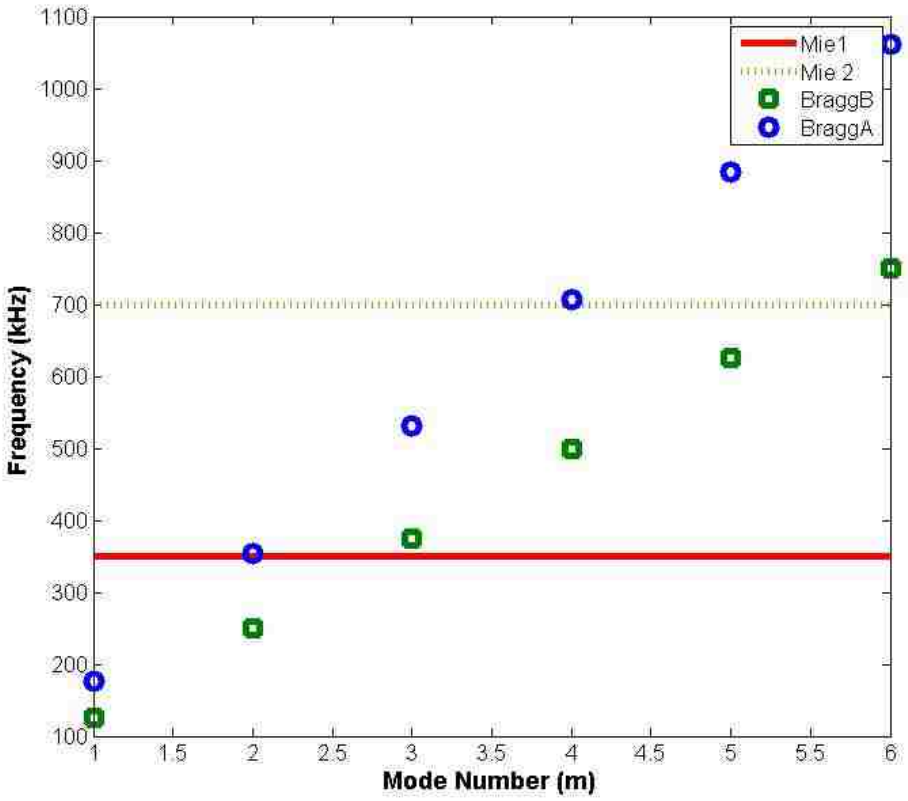

Figure 4.2: Example case for design in maximizing bandgaps based on mode locations of the Bragg reflections (m) and the Mie reflections (solid and dashed lines)

and unknown forces with known and unknown displacements through an assembled stiffness matrix. Commercial programs such as ANSYS ®and SAP 2000 ®utilize this concept in conjunction with a graphical user interface (GUI) to facilitate the design and understanding of models through visualization for the user.

$$\underline{F} = \underline{Kd} \tag{4.5}$$

Damping is implemented in this analysis to provide realistic effects in the presented results. The inclusion of damping can at times be complex in certain applica-

tions. The type of damping used in this analysis is frequency-independent material damping. The damping, thus, takes effect only on the materials for which the damping is specified. The effects of damping can sometimes have undesirable consequences on otherwise controlled parameters. For instance, damping can cause changes in the inherent material's properties such as impedance. The effects of impedance, as discussed earlier, are responsible for allowing or disallowing wave propagation (e.g. reflections). This parameter must therefore be checked in its use.

The free vibration equation is used in finite-element given by Equation 4.6

$$[F] = [M][\ddot{x}] + [C][\dot{x}] + [K][x] \tag{4.6}$$

for a harmonic analysis using the full method. The force matrix is given as $[F]$ which is equal to the mass matrix $[M]$ multiplied by the acceleration $[\ddot{x}]$ plus the damping matrix $[C]$ multiplied by the velocity $[\dot{x}]$ plus the stiffness $[K]$ multiplied by the displacement $[x]$. The plane wave equation discussed earlier for a homogeneous material, Equation refEq:wave, is for considering full-elastic isotropic materials used to detect flaws in materials, although when damping is considered, more terms are introduced. Therefore the inertial and stiffness terms from the vibration equation can be linked to the wave equation when damping is not considered.

The damping matrix for finite element is found through equation 4.7

$$[C] = \alpha[M] + \beta[K] + \frac{2\xi}{\Omega}[K] + \Sigma\beta_j[K_j] + \sum[C_K] + \sum\frac{2\xi_j}{\Omega}[K_j] + \sum\frac{g_j}{\Omega}[K_j] \tag{4.7}$$

in which α and β are the global constant stiffness and mass damping factors (respectively), ξ is the global constant damping ratio, which are all material independent and Ω is the excitation frequency [79]. In addition, each of the previously mentioned damping quantities can be specified as material dependent for materials 1:j along with g_j, the frequency-dependent structural damping coefficient for material j. An

element damping matrix $[C_k]$ can also be supported for certain element types.

Three types of damping are initiated through the use of the damping factors described above: viscous, structural, and Coulomb. Viscous damping is velocity-proportional damping which is characteristic of fluids and linear dependent with frequency. Structural damping is the internal resistance to movement within a material and can be related with solid damping, which accounts for energy loss between structural joints in a system. Structural damping becomes analogous to viscous damping in the full method (use of nodal coordinates). Coulomb damping has non-linear effects, as it opposed motion through effective static and kinetic frictional forces within elements [80].

The finite element analysis used in this work was conducted with ANSYS, a commercial finite element software. An acoustic analysis was performed to benchmark three case studies from the literature and one case study of the experimental observations from Chapter 3 of this thesis. In addition, simulations were also conducted for ABG sensor response to substrate strain found at the end of this chapter. Under acoustic investigations in the program, modal analysis and harmonic analysis can be implemented based on desired results. A modal analysis is generally a good starting point to find natural frequencies for a given model. A harmonic analysis also provides useful results such as material displacements in the frequency domain for a given range of frequencies. Harmonic analysis only accommodates steady state interests which suits the goals of this project. Transient results can be obtained through modal analysis and other types of acoustic investigations. There are a few methods to choose from in solving the harmonic analysis. The reduced or mode superposition methods are choices, but only the full method can handle asymmetric matrices [81]. Finally the sparse solver was chosen over the Jocobi Conjugate Gradient (JCG) solver and the Incomplete Cholesky Conjugate Gradient (ICCG) solver. Although the JCG is recommended for most analyses, it was found that the sparse solver saved

in run time and was sufficient in producing repeatable results.

Various models were tried including a recommended air layer surrounded by an infinite absorbing boundary in which no reflections are produced. This model used special absorbing line elements (FLUID129) that surrounded a fluid layer (FLUID29) produced especially for an acoustic analysis. Upon testing, it was determined that this condition provided a scenario that was isolated and did not allow for proper energy dissipation for benchmarking realistic cases. For this reason, a newer model was created to permit some necessary reflections and energy release through more rigid material surroundings in place of fluid. The model can be seen in Figure 4.3.

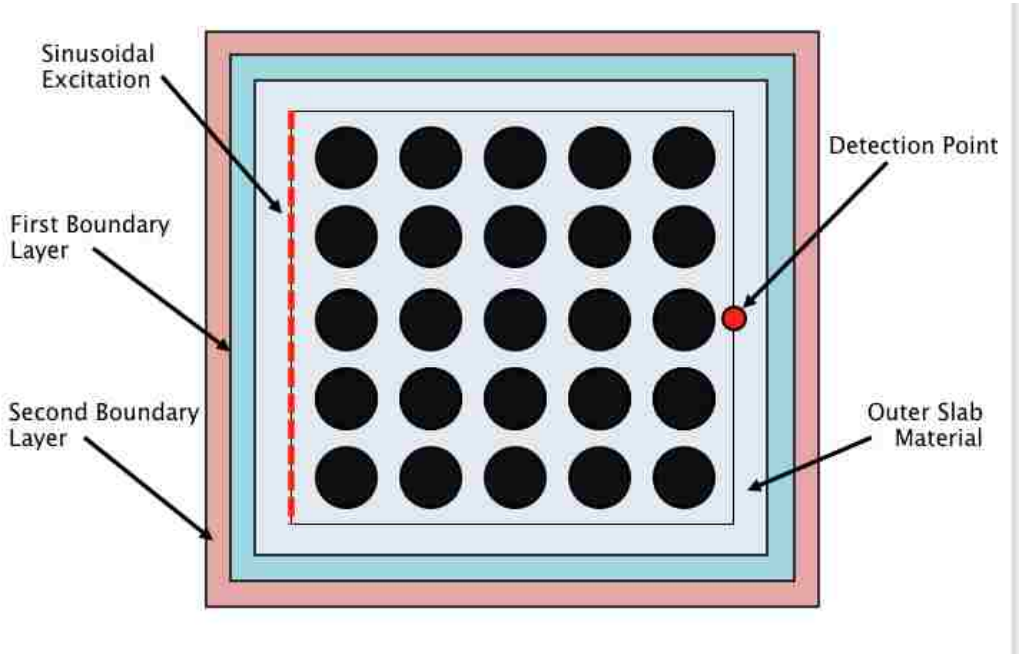

Figure 4.3: Pictorial of boundaries used in the FE model simulation to model case studies

Table 4.1: Materials and their properties used in Vasseur et. al [39]

Material	ρ (kg/m^3)	C_l (m/s)	C_t (m/s)	C_{11} $(10^{10}N/m)$	C_{44} $(10^{10}N/m)$
Duralumin	2799	6342	3095	11.26	2.681
Epoxy	1142	2569	1139	0.754	0.148

4.2 Case Studies

4.2.1 Case Study 1: Vasseur et al. [39]

An early example of experimental evidence for the presence of a bandgap was shown by Vasseur et. al [39] with their Epoxy and Duralumin crystal. This ABG material was made up of a square array of cylindrical Aluminum inclusions produced at a macroscale. The lattice constant here is 20 mm, leading to a filling fraction of 0.50 for an inclusion radius of 8 mm. There is a total of 25 scatterers lined up in a 5 x 5 array. The material properties can be found in Table 4.1. A P-transducer was used with a 500PR pulser/receiver. The measurements of displacements were taken using an oscilloscope. The transducers in the experiment were circular with a diameter of 31.75 mm, in the same dimension range as the lattice constant. For this reason, signals were averaged from the different transducer positions running along the receiving face of the specimen.

The finite element model that produced the results in 4.5 was built in two dimensions as seen in Figure 4.4. The center square cell represents the ABG sensor with the origin of the vibrational displacement beginning on the left edge and the detection point located on the right edge. A results-based model led to the formation of an additional slab of matrix material surrounding the center ABG cell with two outer boundaries. These boundaries were intended to act as a perfectly matched layer (PML), in which the boundary would have the ability to fully receive the displace-

ment wave with little or no loss to reflections and exhibit high energy absorption. However it was found that some reflection better reproduced the benchmark results. So the PML was carried out as a semi-absorbing boundary which acted as an energy dissipater, yet still provided enough impedance match to allow energy across the boundary with a reasonable amount of reflection toward the center cell.

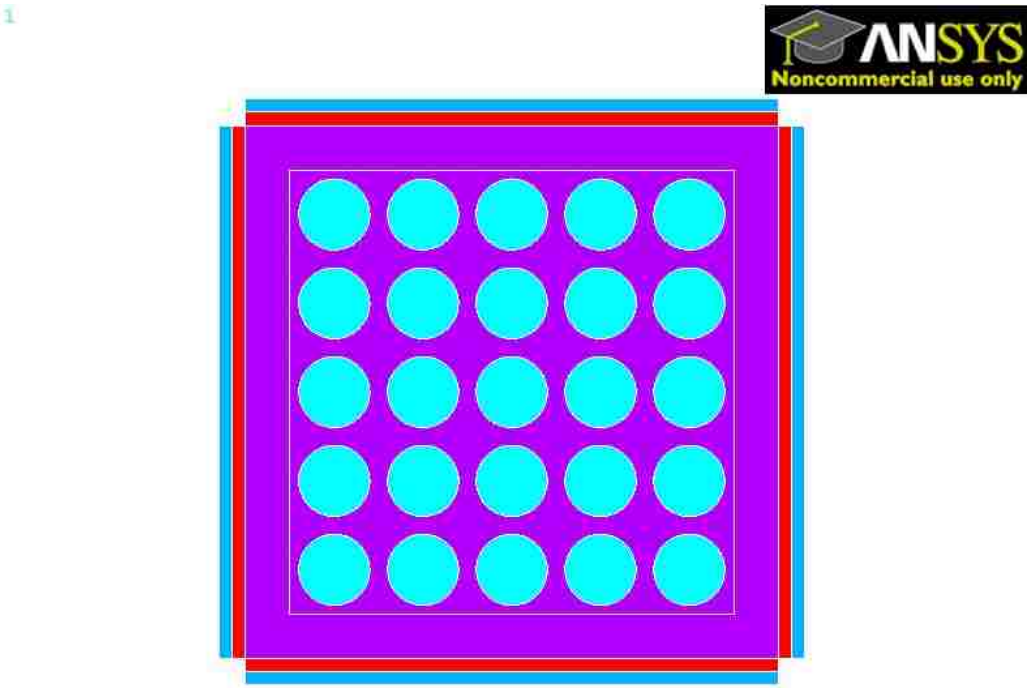

Figure 4.4: Computational model of Vasseur et al. [39] showing the circular Duralumin inclusions in Epoxy arranged in a square lattice with outer slab and two semi-reflective boundaries

For the model in Case Study 1, the ABG material (center cell) was 10.5 cm x 10.5 cm x 10.5 cm with the surrounding slab boundary thickness of 10 mm. The outer Epoxy boundary was followed by three 3 mm layers of damping material with similar properties as the Epoxy. The damping layers were defined with 70 percent frequency-independent damping with lower levels of stiffness from Epoxy-matching to less stiff

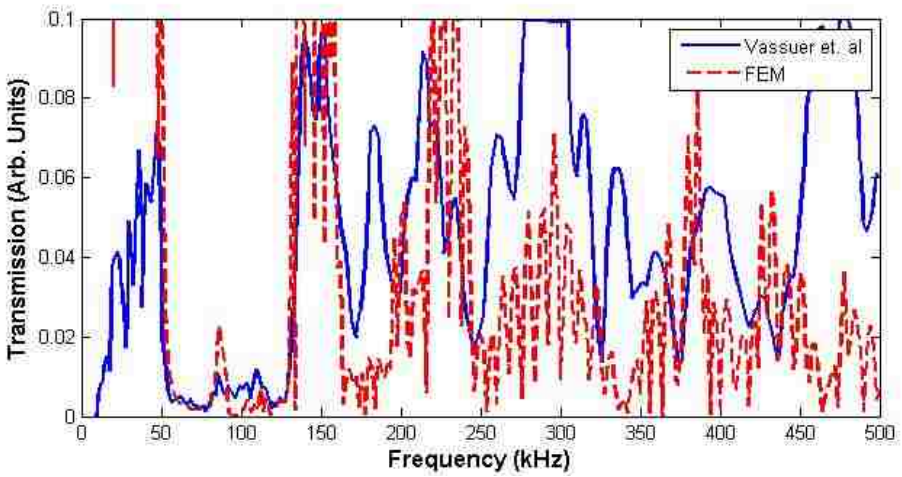

Figure 4.5: Comparison of experimental results (Solid) from Vasseur et al. and numerical simulations by the FE model (Dashed)

from inside to outside. A displacement amplitude of 6μm was selected based on literature also using Panametrics delta broadband 500 kHz P-transducer with 500PR pulser/receiver [82]. The experimental results are shown in 4.5 in comparison with the FE results obtained from this model. The Y-axis in this report was shown in terms of the transmission coefficient and was not normalized as a case was not run for a pure Epoxy matrix. The Y-axis, thus represents the power received divided by the power put in to the system. It can be observed that the FEM results match the experimental bandgap frequency range and both sides of the gap profile line up extremely well. Due to a truncated report of the experimental results the Y-axis only goes to 0.1 (10 percent of the input energy). The magnitude of the FEM is within 15 percent transmission of the experimental values within the given window with the exception of frequencies lower than the bandgap (50 kHz). The FEM model approached a value of 1.9 at these frequencies. The low transmission reported at these values for the experimental results most likely is due to the ramping up of the transducer power, although was not accounted for by the authors when dividing by the input power.

Table 4.2: Materials and their properties used in El-Kady et. al[70]

Material	Mass density (kg/m^3)	Longitudinal Wave Velocity (km/s)	Shear Wave Velocity (km/s)
Tungsten (W)	19250	4.611	2.980
SiO2	2200	5.840	3.764

4.2.2 Case Study 2: El-Kady et al. [70]

One example of experimental evidence for phononic crystals is given by El-Kady et. al [70]. More interesting is the fact that these results were produced using a phononic crystal with dimensions at the microscale. The geometric properties of the crystal consists of a simple square lattice of dimensions 405 μm x 405 m with a lattice constant a of 45 m and an inclusion diameter of 28.8 μm. The host material was made of SiO_2 with embedded Tungsten (W) inclusions. The material properties are given in Table 4.2.

Their study used integrated AlN (aluminum nitrate) electroacoustic couplers for sending and receiving displacement signals. The signals were sent to and received from a network analyzer which measured the longitudinal vibrations. The ABG crystals measurement was normalized by measurements from a bulk matrix specimen consisting of only the host SiO_2 material in a method similar to the experiments performed in this thesis. The difference in these experiments, however, was the necessity of placing small air holes in the center of the Tungsten (W) inclusions. The air holes were required for fabrication purposes to allow for an undercut. Therefore, the matrix specimen was also produced with air holes. A study of the effect of air holes and their size within the inclusions was conducted using a finite-difference time domain (FDTD) simulation. It was shown that as the diameter of the air hole was increased, the thinner the gap became by shrinking from the left (lower-frequency) side as the right side of the gap stayed mostly constant. A value of 5 μm was chosen

for air hole radius making up around 11 percent of the lattice constant value. An air hole radius of 20 percent of the lattice constant was determined to begin destruction of the bandgap profile. The model is shown in Figure 4.6.

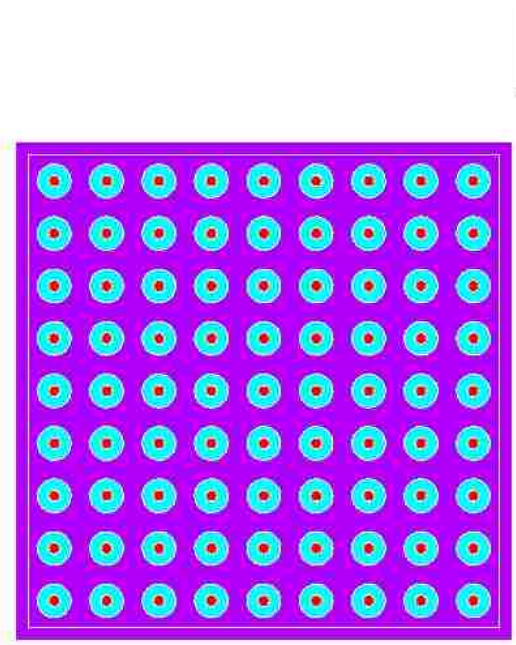

Figure 4.6: Computational model of El-Kady et al. [70] showing the circular Tungsten inclusions with small air-holes in SiO_2 arranged in a square lattice with outer slab and two semi-reflective boundaries

The finite element model is compared to the theoretical and experimental results given by El-Kady et al. for the case with no air holes. The results are shown in Figure 4.7. The finite element model to produce these results was constructed using a modulus of elasticity of 410 GPa (75 GPa), a density of 19250 kg/m^3 (1142 kg/m^3), and a Poisson's ratio of 0.27 (0.165) for the Tungsten (W) inclusions (SiO_2 matrix). A simulated wave front was produced by a sinusoidal displacement on the left-most line of the computation cell indicated by a blue dashed line in Figure 4.4.

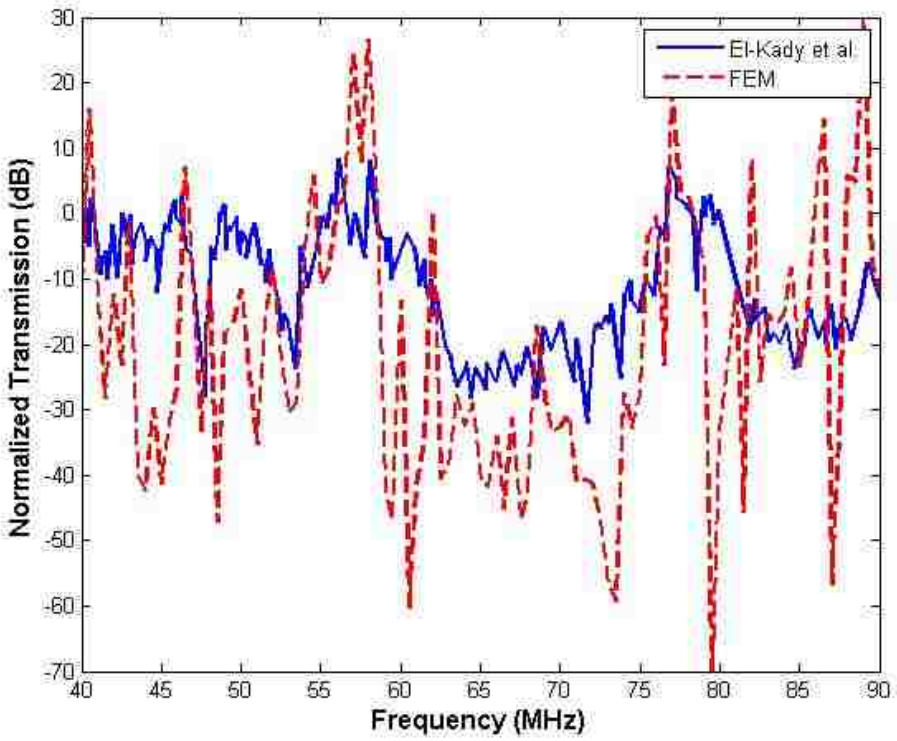

Figure 4.7: Comparison of experimental results (Solid) from Vasseur et. al and theoretical FEM results (Dashed)

Special boundaries were applied on the model which aided in the realistic dissipation of energy and allowed for appropriate reflections within the computation cell. The slab surrounding the cell was made up of 10 μm of SiO_2 (about a quarter of the lattice constant) followed by a two layers of 0.5 μm damping materials. The slab was made with the same material properties as SiO_2, but the two damping layers varied in elastic modulus and were assigned material damping of 70 percent as done in the previous case study analysis. Again a slight impedance mismatch was implemented for limited reflections yet allowed for energy movement across the boundary for energy absorption.

The amplitude of the displacement was based on an estimated value derived from

the piezoelectric equation 3.1. A table lookup value for a PZT ceramic piezoelectric material yields a piezoelectric charge constant of 400E-12 m/V for the thickness mode. A maximum estimated potential difference of 0.5 V gives around 0.2 nm which was used in the simulation.

4.2.3 Case Study 3: Mohammadi et al. [71]

Another micro-structured phononic crystal is considered here. The experimental evidence provided by Mohammadi et al. [71] was selected due to the more complicated lattice structure. A benchmark case such as this one will enhance the analytical models credibility by exemplifying robustness in its ability to simulate response.

A hexagonal Bravais lattice structure (minus the center) was experimentally verified at the micro-level using a lattice constant of 15 and a radius of 6.4 attempting a strong gap based on reducing symmetry in the Brillouin zone. The research encompasses the growing movement to plate structures over SAW devices or bulk structures in the creation of ABG materials. Several bridge-like plate structures were produced using a 14-step fabrication process on Silicon. The process included metal deposition for the creation of the electrical transducers along with zinc oxide sputtering for the piezoelectric effect and lithography and plasma etching for the hole removal. Due to the frequency limitations of the small size transducers, 18 devices had to be manufactured to excite various frequency intervals and were summed up and averaged over the frequency domain in question.

The same model layout was used for this analysis as done before with changes only in dimensionality and can be seen in Figure 4.8. The slab layer outside the center cell was 60 μm on both sides of the center cell and 20 μm on top and bottom of the center cell surrounded by two damping layers of 4 μm. Again 70 percent frequency-independent material damping was used in the damping layers of simi-

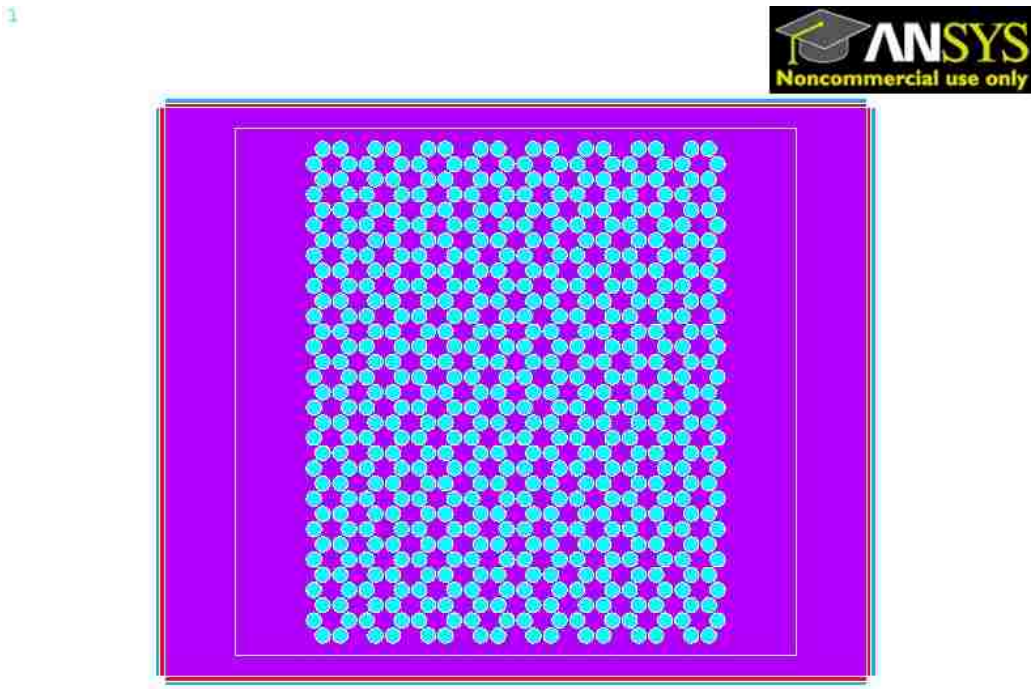

Figure 4.8: Computational model of Mohammadi et al. [71] showing the circular air inclusions in Silicone arranged in a square lattice with outer slab and two semi-reflective boundaries

lar characteristics. Again, the boundary conditions were selected based on results-matching. Although the boundaries of the samples were not provided, a picture indicates that the sample was created with long edges also outside of the center cell with some distance between the first rows of inclusions and the transducers. The analytical results can be compared to the experimental reporting in Figure 4.9.

4.2.4 Case Study 4: Experiments

The next case study is performed for the Epoxy specimens tested in this thesis. The theoretical results provide a guide that can demonstrate, firstly, if a bandgap exists

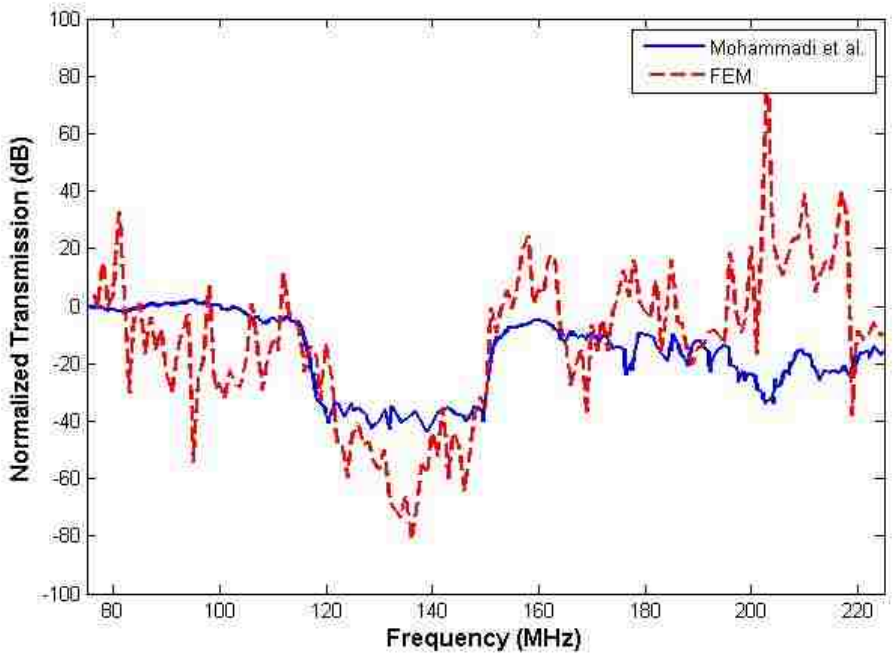

Figure 4.9: Comparison of experimental results (Solid) from Mohammadi et. al and theoretical FEM results (Dashed)

for the geometries and materials used. Second, the simulation results can serve as a guide to the frequency region where the bandgap should occur if one is found to be present.

The surrounding slab was again made with the same material as the host matrix: Epoxy. A slab thickness of 2 mm was used surrounding the inner cell for all cases. The two outer damper layers used 2 mm each of material-specified frequency-independent damping of 0.7. The first damping layer was made with an elastic modulus of 2.9 GPa to match the surrounding slab since it has been found that little impedence contrast should exist at the boundary. The next boundary, however, is made up of two-thirds of the first elastic modulus to account for the energy dissipation throughout the first damped boundary also allowing for some reflection based on small impedence difference.

Table 4.3: Bragg and Mie first mode reflection locations for experimental cases

Filling Fraction	**a (mm)**	**d (mm)**	**C_M (m/s)**	**C_S (m/s)**	**C_{Bragg} (m/s)**	**$Bragg_1$ (kHz)**	**$Bragg_2$ (kHz)**	**Mie (kHz)**
0.18	3.15	1.69	5009	1616	2234	318	225	1482
0.28	5.28	3.17	5009	1616	2577	244	173	790
0.40	4.44	3.17	5009	1616	2975	335	237	790
0.50	3.96	3.17	5009	1616	3324	420	297	790

The FE results are first presented in Figure 4.10 free of reflections from boundary conditions to maximize bandgap viewing ability. Based on this analysis, it is evident that gaps are present for these material types and geometries for filling fractions 0.28, 0.40, and 0.5. As previously described by the literature, the higher filling fractions shows the most significant gap. These results correlate well with the calculation approximations found in Table 4.3. The Bragg and Mie calculations listed in Table 4.3 match extremely well with the FE results. The simple calculations are broad approximations and do not account for such variables as transverse component interactions caused by transverse velocity (based on Shear Modulus) and exact wavelength representation due to the interaction between the matrix and inclusion materials.

Notice that the results for the 0.18 filling fraction case are not represented in Figure 4.10. This is because there was no gap present due to the low filling fraction. Although calculations show that a gap can occur at 318 and 225 kHz, it is dependent upon the physical interaction (impedance mismatch) for the gap to take place. It can be noted also that that Mie frequency is out of the domain for these gaps. A Mie reflection will not produce a gap by itself, yet can aid the quality of the gap when it is within reach. For example, a Mie reflection generally helps to bond the two Bragg modes.

The first gap and the largest, is of course produced by the highest filling fraction,

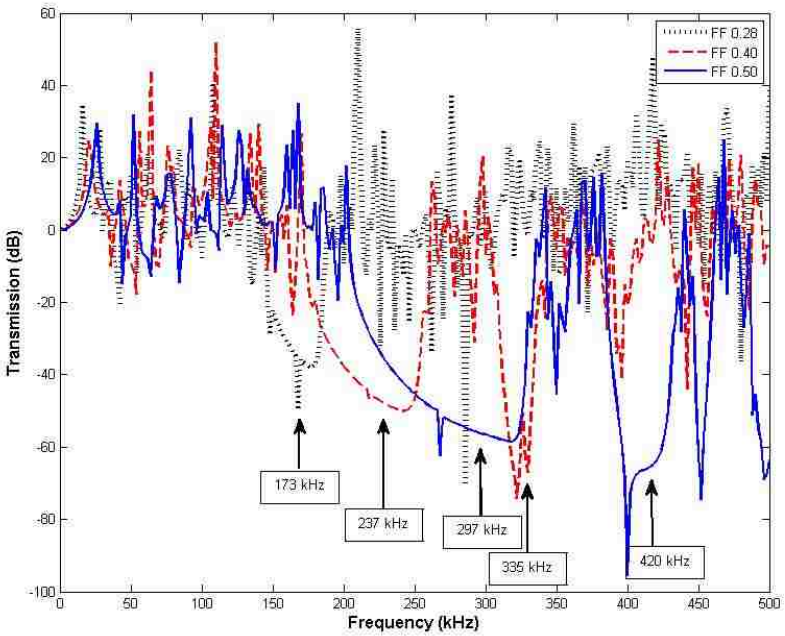

Figure 4.10: Analytical results in unbounded condition for filling fractions 0.50, 0.40, and 0.28

FF = 0.5 shown in Figure 4.11 normalized and with the boundary conditions stated above to simulate realistic conditions. The finite element results are plotted by a dashed line against the experimental results (solid) and show excellent gap boundary matching for the larger $Bragg_2$ first mode located between about 180 kHz to 300 kHz. There is a large jump afterwards in the experimental, where the computation results stay lower. This can be attributed to the piezoelectric transducers overpowering the profile of the experimental, yet it can be seen that the second gap ($Bragg_1$) is almost emerging around 410 kHz matching the anti-resonance in the computational results.

Another example of the FE results is shown alongside the experimental results in Figure 4.12 for the normalized averaged case of samples with filling fractions of 0.40. The results are found through normalization using an identical model with Epoxy in place of Aluminum inclusions. It can be seen that two gaps are predicted

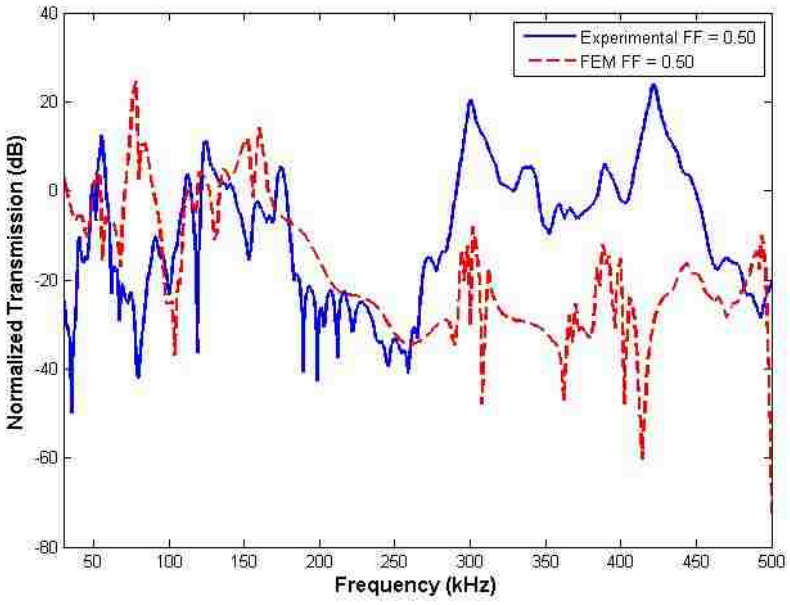

Figure 4.11: Comparison of normalized experimental (Solid) and finite element results for filling fraction of 0.50

by the FE model between about 200 and 280 kHz and again between 310 and 340 kHz signifying again $Bragg_1$ and $Bragg_2$. The fact that two gaps are present, as in the previous case, indicates that the two reflection modes did not merge.

Ways to couple these gaps include increasing the impedance difference between the matrix and host materials, increasing the filling fraction, or introducing the Mie reflection mode if not already present. The experimental results only show one main gap. The second gap is either not present or masked by the anti-resonance occurring at the same frequency (most likely due to the piezoelectric crystals). A small drop is shown around 350 kHz in the experimental results which could be evidence of that second gap. Nevertheless, material property or geometrical changes need to take place in order to merge the two gap modes for a strong bandgap.

The second experimental gap example shown in Figure 4.13 is not as noticeable

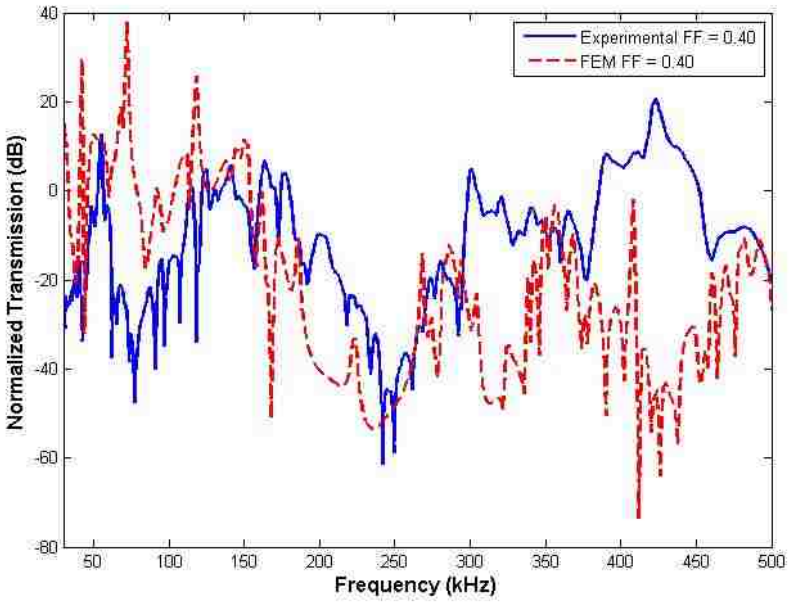

Figure 4.12: Comparison of normalized experimental (Solid) and finite element results for filling fraction of 0.40

as the first, although is strong enough to emerge through the transmission profile highly dictated by the piezoelectric transducers. Again we see the experimental gap about 50 kHz higher than the FE results as also seen with less severity in the first two cases (by 5 kHz and 10 kHz respectively). Because this is consistent, it can most likely be attributed to the material properties input in the FEM versus the actual properties. The elastic modulus can be affected by curing temperatures to become more brittle or ductile. This aspect is of course neglected in the finite element model.

4.2.5 Parametric Analysis

It has been shown that the major determinants in producing a bandgap are traced back to impedance differential between the host material and the scatterer material when the geometrical conditions are fit. Impedance Z, however, is dictated by two

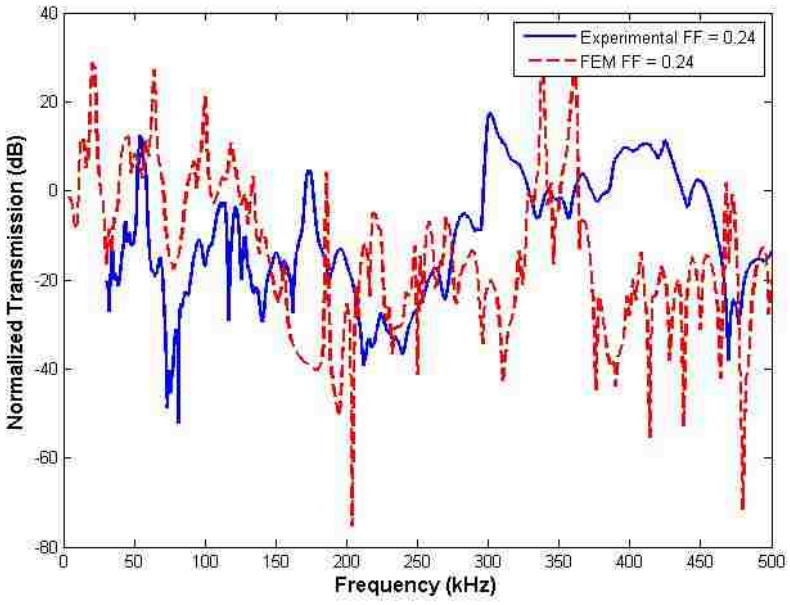

Figure 4.13: Comparison of normalized experimental (Solid) and finite element results for filling fraction of 0.28

other material characteristics as seen in Equation 1.1, density ρ and longitudinal speed of sound C_l. Also this condition also realizes a bandgap if periodicity exists and that periodicity contains the correct filling fraction based on its bravais lattice type. This section tests the resulting change in bandgap profile for given changes in material and geometrical parameters.

A given case similar to Case Study 1 is studied with a fuller gap achieved by decreasing the density from the reported value of 1200 kg/m^3 to 500 kg/m^3. Density and elastic modulus are then variated from the base case to show respective changes in the gap. Material 1 represents the inclusion material while material 2 is the matrix material. Since impedance is proportional to the square root of density and sound speed in a material, it is assumed that both parameters would have a similar effect on the gap. Considering Figure 4.14, it can be seen that for higher density in material 1, a shift to the lower frequency region occurs while a lower density endures a shift

upward in frequency with definite overall gap quality measured by the proportionality of gap width to mid-gap frequency. Also, a second gap appears for the low density. Inversely, a high density for material 2 causes a shift downward in frequency with diminished gap quality and also a second gap appearance.

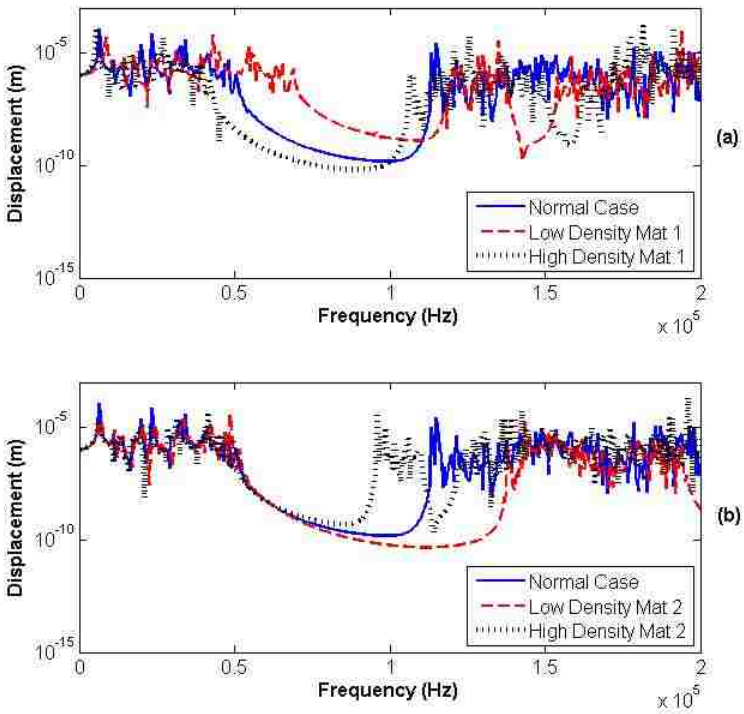

Figure 4.14: Parametric study for change in density in material 1 (a) and material 2 (b)

Figure 4.15 shows the results for changes in elastic modulus for material 1 (a) and material 2 (b). It is shown that a higher elastic modulus in material 1 also slightly increases gap quality, and causes the immersion of a second gap; the second mode gap. Interestingly, the shift occurs at the opposite side of the gap for the elastic modulus change than the density change. The same can be said for part (b) which shows the change in elastic modulus of material 2. Although lowering the elastic modulus of material 2 leads towards a larger gap, it is at the expense of decoupling

the gap's two modes. This could mean that the maximum impedance threshold is met, although higher filling fraction could remedy this.

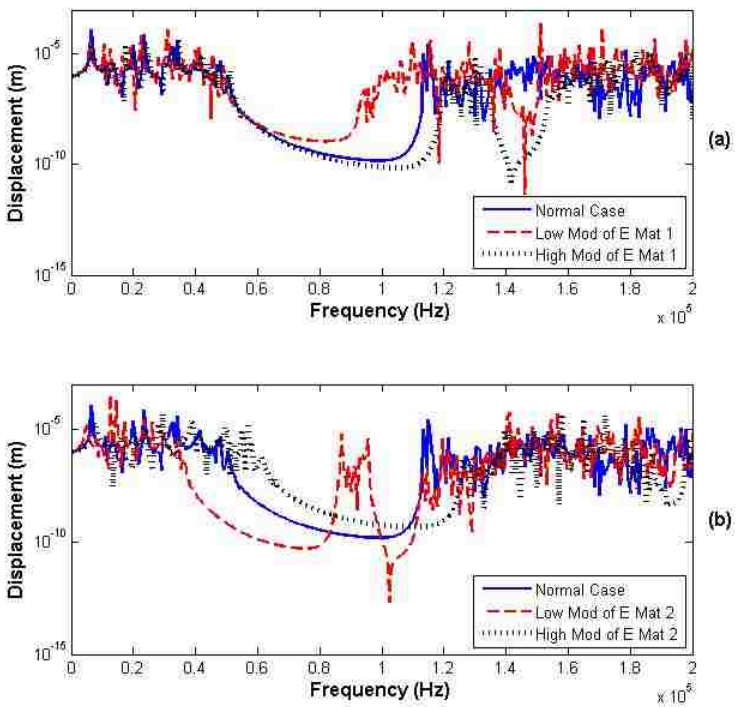

Figure 4.15: Parametric study for change in the elastic modulus in material 1 (a) and material 2 (b)

Lastly, Figure 4.16 addresses the geometrical dependency by considering the inclusion diameter in the material. A higher diameter makes a 10 kHz shift to the right with a neglible increase in width, yet at the expense of depth. A second gap appears, which is the second Bragg mode around 180 kHz (twice the frequency of the gap at 90 kHz). A lowering of the diameter has much higher consequences as the gap is reduced to half its width at the right side. It is important to point out that the diameter change is directly linked to filling fraction.

The explanation for these changes can be explained by the relations that have

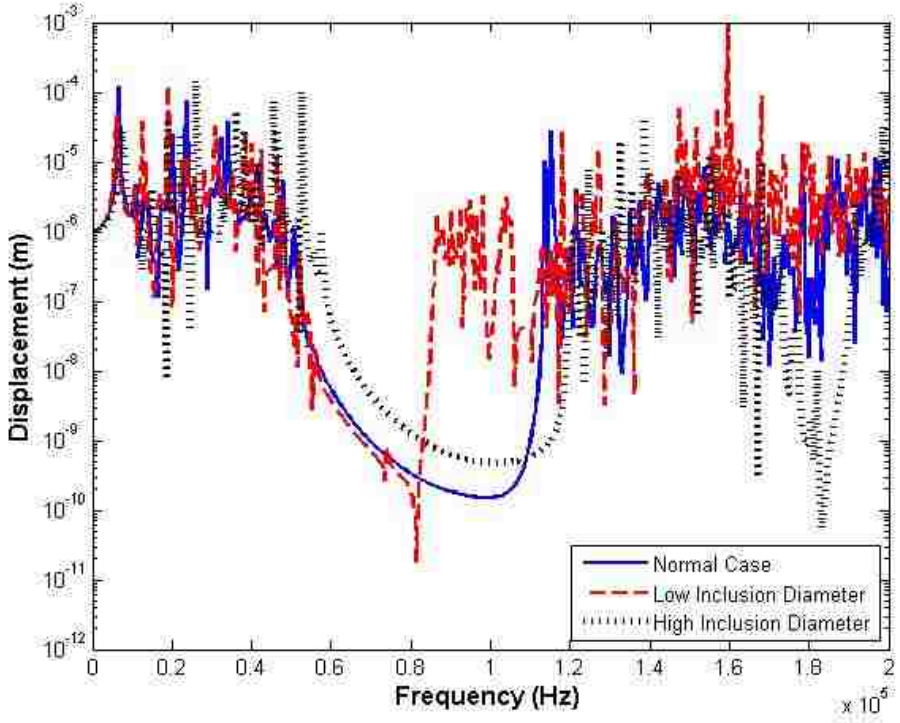

Figure 4.16: Parametric study for change in inclusion diameter

been discussed in this thesis. In many cases two gaps are present whether they are decoupled from one gap or appear. The second gaps can be the $Bragg_A$ of the same mode if separated by a scalar value of the $\sqrt{2}$ multiplied by the $Bragg_B$ reflection location or could be the coupled $Bragg_A/Bragg_B$ second mode if located at double the location frequency of the first. Although changing density and the elastic modulus are directly related to impedance, these parameters also contribute to the speed of sound in the material. Although a higher impedance for material 1 and lowed impedance for material 2 generally help to create better impedance mismatch for the ABG material, a higher density will decrease the speed of sound in the material and vice-versa for a higher modulus of elasticity.

4.2.6 Feasibility Study for Damage Monitoring

The study of defect modes in ABG materials has been studied before with regard to waveguides [33], [29], [64] where it has been shown that passbands, bands of transmission, can form, thus disrupting the band profile. Here, similar defect modes can occur with induced strain, as previously stated. By compromising the lattice constant dimension, the fundamental structure of ABG occurrence, a defect is thereby created by the induced strain which is then indicated by the bandgap profile. A delamination in a composite, for example, could show signs of debonding through a localized strain. Such a strain would translate into the less-stiff ABG matrix creating a wider lattice above the strained area. Similarly, uniform strains due to situations such as thermal effects should be addressed to avoid false positives. This section looks at the theory of concept proposed by ABG sensing. Figures 4.23 shows the models for the strain cases for the results shown further in the section which can simulate damage such as that shown in Figure 4.17.

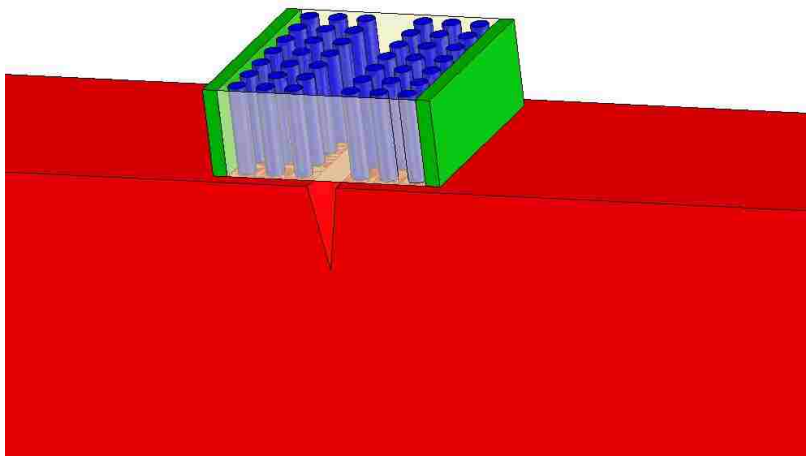

Figure 4.17: Visual representation of example damage and functionality of ABG sensor

The Vasseur et al. [39] case is revisited to be tested as a representative case for

functionality. This case was selected based on the simplicity of design and also to demonstrate the scalability of the proposed ABG sensing technique with respect to the lattice constant dimension and the center frequency of the gap. First it is shown in Figure 4.18 how scalability is achieved based on the lattice constant a. For given material properties, a dictates the location of the gap if one is to occur pending proper conditions such as FF and impedance mismatch. The two Bragg modes are slightly separated in the Vasseur et al. [39] case, so the gap quality was enhanced by merging the two modes which was done by lowering the density of the Epoxy matrix material by half to increase the impedance difference between the host and inclusion materials. Figure 4.18 part (a) shows the gap profile on the macroscale using an a of 20 mm. Part (b) shows an nearly identical gap profile created in finite element analysis using an a of 20 μm. Note the frequency range on the X-axis of both plots showing the kHz range for the macroscale model and the MHz range for the microscale model. Both models are un-normalized and created under ideal, low-reflection environments.

Figure 4.19 includes a two-part plot of non-uniform strains taking place in the ABG sensor to incite lattice disruption. Part (a) presents the transmission profile for a highly localized strain occurring at the beginning of the ABG structure in 5 percent and 10 percent localized tensile strain and part (b) presents the same information for localized strain at the end. The 5 percent strain case is shown by a dashed line in both cases while the 10 percent is represented by dotted lines. A small gap disruption is created for the 5 percent lattice constant increase with more visible change for the strain taking place at the end of the structure. The 10 percent change, however, begins to show more noticeable gap deterioration.

A case is also considered in Figure 4.20 for strain that is not localized within the ABG material and is distributed unevenly across several columns of the sensor. Case (a) gives the transmission results for non-localized strain at the beginning of

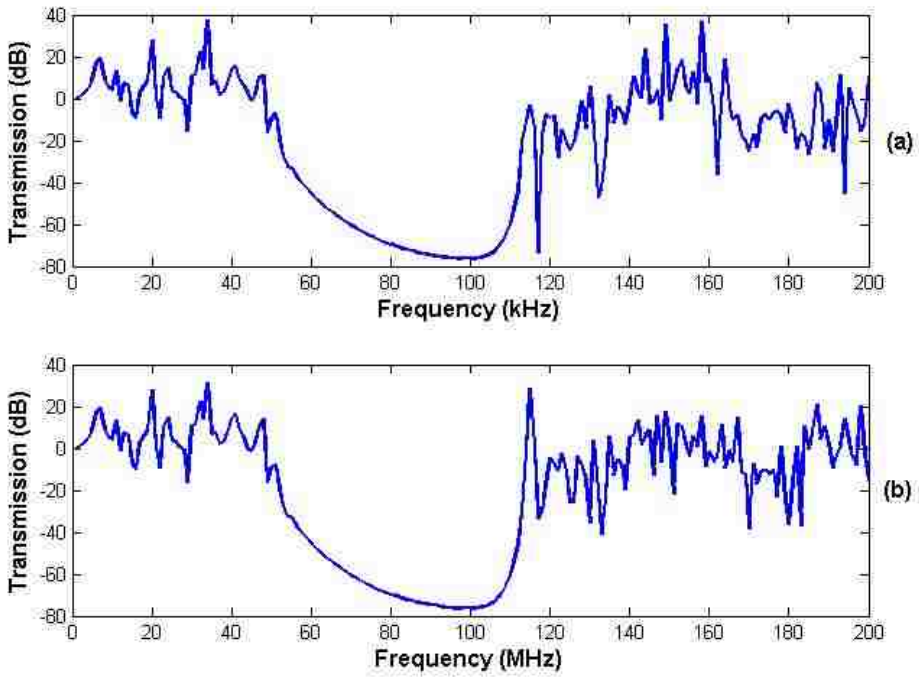

Figure 4.18: Comparison of macroscale ABG results in which a = 20 mm (a) with microscale ABG results in which a = 20 μm (b) to show scalability

the ABG structure distributed between the inclusions from left to right as a 5 μm change (10 μm), 3 μm change (6 μm) and 1.5 μm (3 μm) for a 10 percent overall strain. The same is done for case (b) but runs from the right-most inclusion spacing column inward. Results are similar with a slightly larger change in gap profiles for case (a). The gap profile shows more deterioration in this example of non-localized strain than for the previous case of localized strain with respect to total strain values. A slight shift downward in frequency also takes place attributed to the larger lattice spacings which are repeated here more than in the localized strain case.

Consideration for transversely strained cases is also taken into account. Figure 4.21 presents the results for strains in the range of 10 percent and 20 percent. In can be seen that a larger profile deformation occurs per strain value for this case over

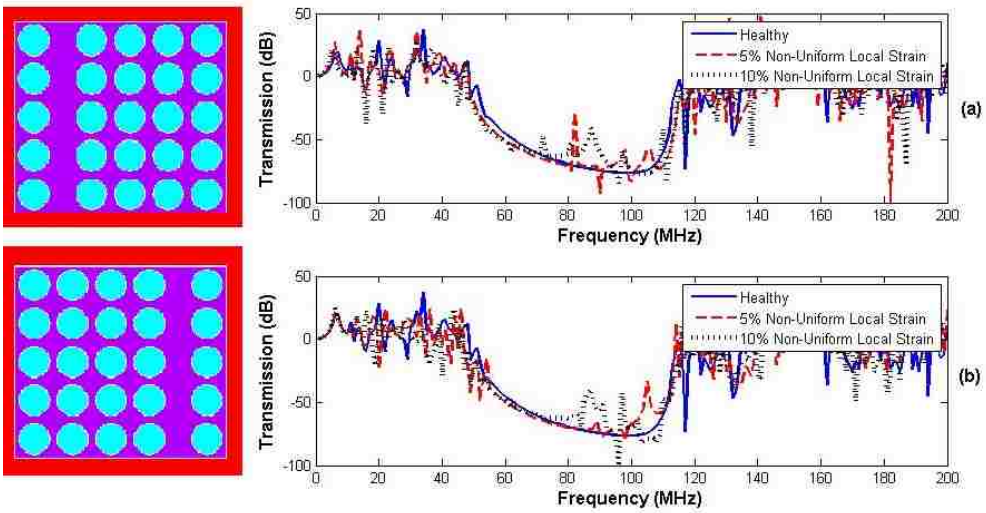

Figure 4.19: Progression of deterioration in band gap profiles for 5 percent and 10 percent localized strain at beginning of ABG (a) and end of ABG (b)

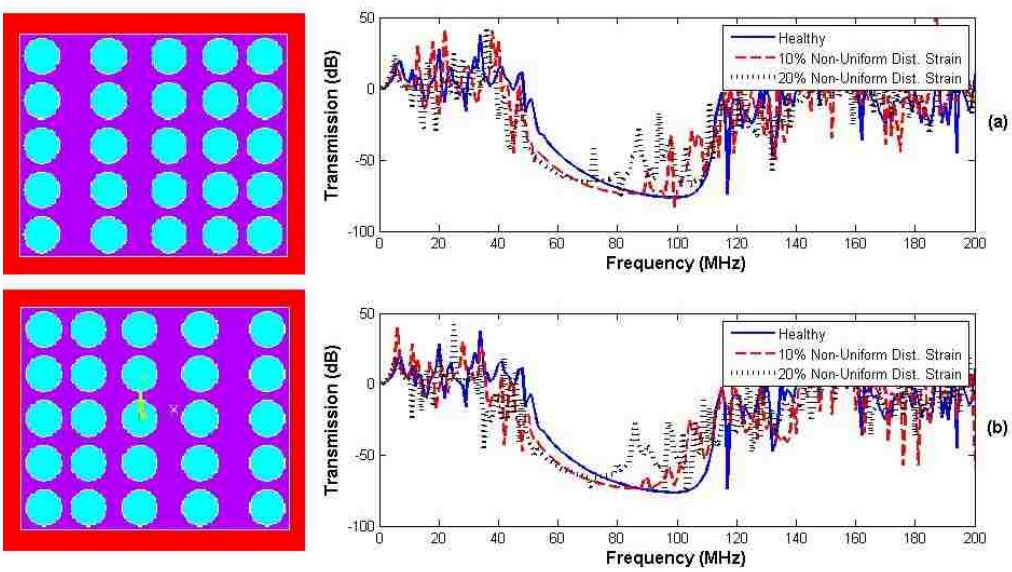

Figure 4.20: Progression of deterioration in band gap profiles for 5 percent and 10 percent distributed strain at beginning of ABG (a) and end of ABG (b)

the previously presented cases. It should be noted that the deformations of the gap profiles up to this point has mainly taken place on the right (upper frequency) side of the gap.

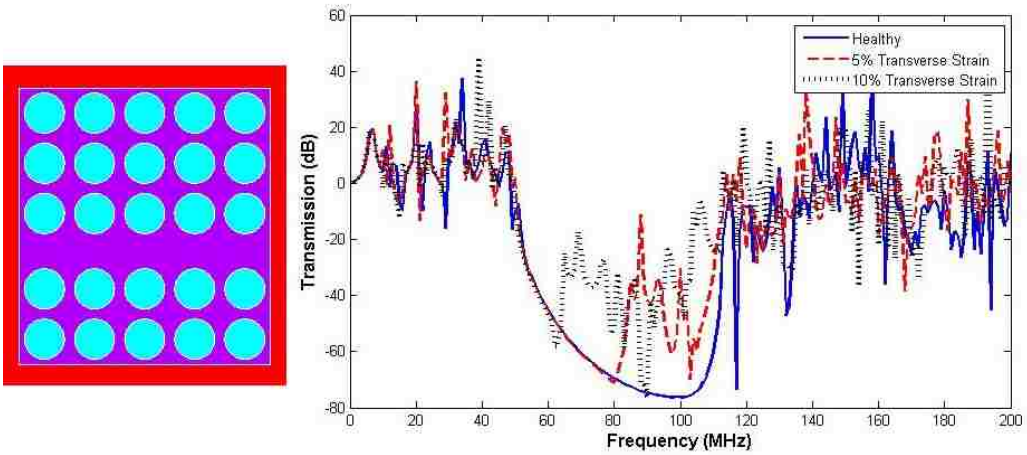

Figure 4.21: Progression of deterioration in band gap profiles for 10 percent and 20 percent localized transverse strain

Uniform strains are addressed in Figure 4.22 in both tensile and compressive instances. The effects of constant strain throughout the sensor adhere to the same rationality in the three instances shown here. For compressive strains (plot (a)), the gap profile shows a clear shift downward along the frequency axis with noticeable gap width reduction. The gap reduction will have consequences on the right side of the gap more than the left because the direct axial Bragg mode is located on this side and moves downward with respect to the lattice constant at a rate of 1.33 over the diagonal Bragg mode. Also the gap is reduced in width due to quality tolerances as the perpendicular geometry differs now from the axial spacings when before both directions were related by a common lattice constant. For compressive strain, only a 5 percent dimension change was possible due to geometrical limitations. The opposite held true in compression versus tension. There is a clear shift upward in frequency with some widening of the gap. The gap widening can also be attributed to the fact

that the effective filling fraction is increased.

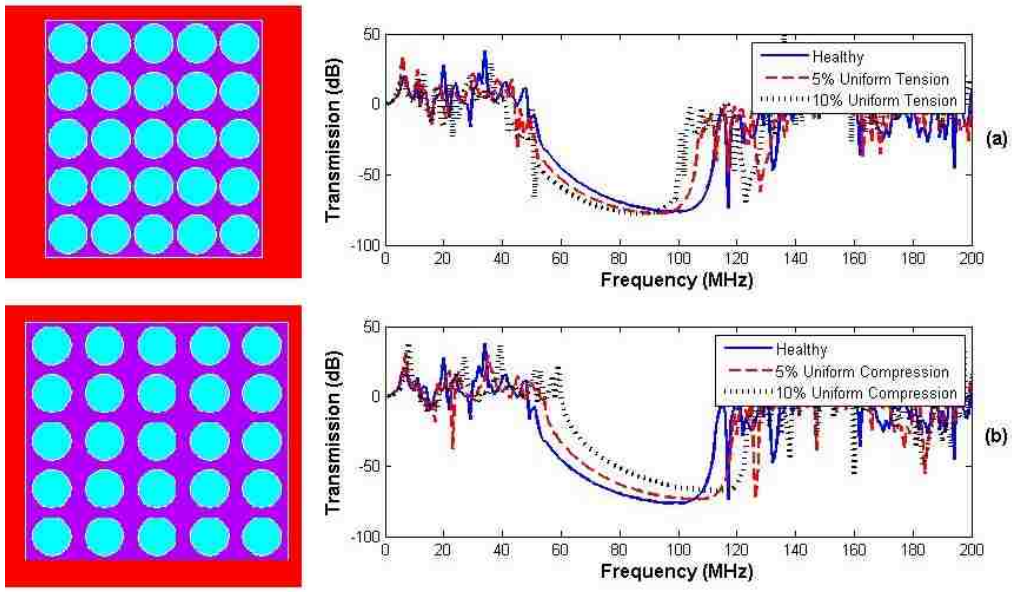

Figure 4.22: Shifted band gap profiles for 10 percent and 20 percent localized transverse strain

This chapter has validated a numerical model from three highly variable cases in the literature ranging in size-scale, geometry, material type, and experimental setup. The computational results match the benchmark cases extremely well in terms of gap location and energy dissipation level with impressive matching of small resonance occurrences outside the gap profile. Comparison with experimental results helped to validate two questionable band gaps and demonstrated changes necessary to merge the two Bragg reflections occurring with the respectively material types. Perhaps most useful employment of the numerical modeling tool was the feasibility study where the functionality of the proposed ABG technique was tested. The results are consistent with the proposed functionality. It should be noted that the scale of strain of the ABG material, based on the periodic disruption dimension based on damage size, translates to a much lower strain value for the substrate component due to the relativity of strain with respect to dimension. Therefore ABG material

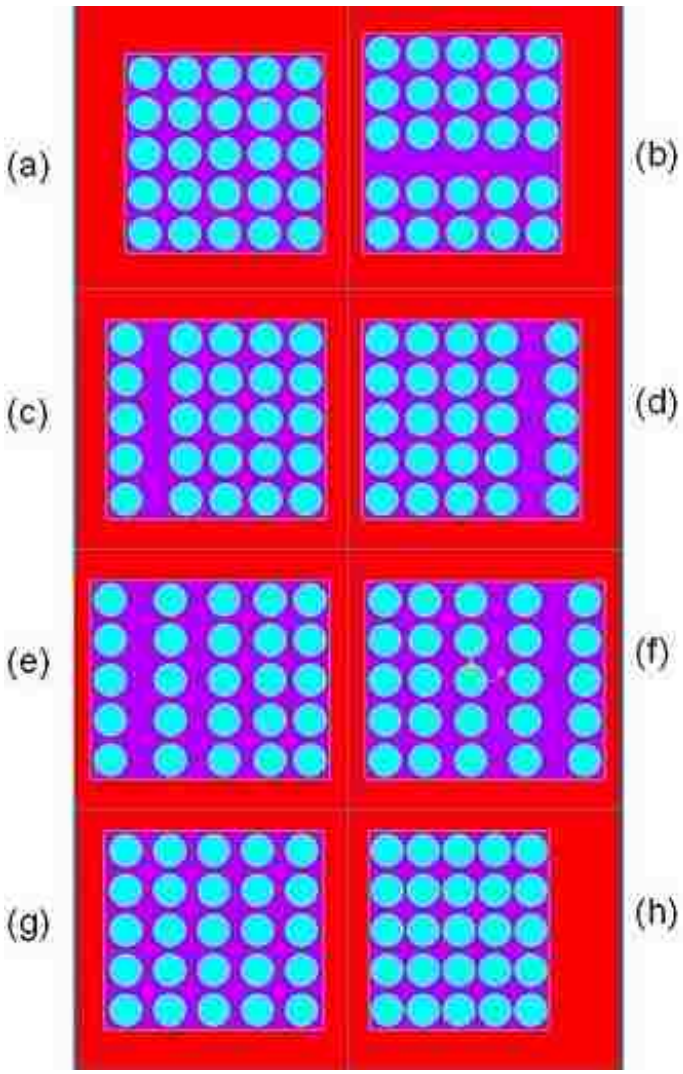

Figure 4.23: Strain cases conditions (a) Normal (b) 10 percent transverse strain (c) 10 percent local strain at front (d) 10 percent local strain at end (e) 20 percent total distributed strain at front from 10 percent to 7 percent to 3 percent (f) 20 percent total distributed strain at endfrom 10 percent to 7 percent to 3 percent (g) 10 percent total uniform tension (h) 10 percent total uniform compression

strain can correspond with lower strain values in the substrate material leading to highly sensitive sensing ability.

Chapter 5

Conclusion

This thesis has examined the use of acoustic bandgap (ABG) materials as sensors for damage detection for structural health monitoring (SHM). The need for new types of sensing techniques in has been discussed with the interest in hot spot monitoring. Specifically, it was demonstrated that there is a clear desire for the aerospace industry to move towards condition-based monitoring from the current time-based monitoring methods which can be realized with innovative and reliable sensing techniques. New sensing techniques are among the essential components in accomplishing the ability to create smart structures capable of condition-based monitoring. Although initial costs for research, transition, and implementation may be high, such investigations can have economical savings that can be realized by removing unnecessary maintenance and inspection time, early detection of damage, and through aiding in the design of new structures. Most importantly still, are the safety benefits.

In addition, past research looking at the phenomenon of acoustic bandgaps has also been reviewed. Both theoretical and experimental investigations were covered that aimed to create and investigate the performance of acoustic bandgaps. The governing geometric parameters and material properties were outlined discussing the

major contributors to attaining an ABG. These contributing factors were highlighted beginning with material property aspects such as high impedance contrast between inclusion and matrix materials and moved onto geometrical suggestions like the use of high filling fractions and the different lattice configurations. Small-scale ABG materials were also discussed to demonstrate the feasibility of ABG fabrication in the future where ABG devices can be exploited for different uses like ultrasonic transducers, waveguides, antennas, and for sensors as suggested here.

The experimental methods summarized the steps taken to fabricate a macrosized ABG material and the parameters for each of the material components that make up the ABG material. The experiments considered 16 total specimens aimed to span a range of possible acoustic gap forming elements. Eight specimens for two host materials were each tested for long and short specimens of four filling fractions ranging from 0.18 to 0.50. The results for the elastomer host cases proved mostly inconclusive as the response detected across the material was too low to show any representation of bandgap behavior. Smaller sized specimens, stronger transducers, or a combination of the two could help with this issue in future work. Such work could prove interesting, considering the large impedance contrast possible with such a low stiffness material. In addition, elastomers would seemingly perform very well considering their elongation ability to assume the strain characteristics of underlying substrate material and should be considered again with the above-mentioned recommendations.

On the other hand, the results for the epoxy-based ABG sensors provided three gap formations. Due to an overpowering response signal believed to be dictated by the piezoelectric crystal, bandgaps were difficult to isolate with certainty. Again, strong transduction of the signal could improve the representation of attenuation, especially at high frequencies. This attenuation was much more apparent in the response of specimens with high filling fractions and long dimensions, making the

response for the specimens that are more likely to have bandgaps more difficult to distinguish in that frequency range than the other specimens. Although great care was taken to choose an appropriate piezoelectric ceramic that worked for the necessary frequency range, it is the ceramic that is attributed to the difficulty in realizing the presentation of gaps. Furthermore, a higher impedance difference between the host and inclusion materials is necessary to merge the gap modes and/or the introduction of the Mie reflection could prove useful in creating a strong gap.

The analytical models, consisting of gap location calculations and the implementation of a finite element method, were very helpful in this investigation. The finite element model was benchmarked using three diverse case studies from the literature for validation. The first case study consisted of a macro-sized bulk ABG material and the analytical results matched the experimental findings very well showing both existence and gap placement agreement in the frequency range. The second and third benchmark cases consisted of much smaller dimensionality and were also validated with strong agreement. Benchmark case 3 was especially interesting in that the analytical model demonstrated its robust ability in matching the results for such a complex lattice structure at a very small scale. This proves the FE model to be an excellent tool for the design of ABG sensors.

The FE model was also tested against the experimental results presented in this thesis. Three experimental gaps were found in three of the four geometries tested, matching the numerical analysis. The gaps for each case were separated according to Bragg mode. It is therefore obvious that a greater impedance difference is necessary to strengthen the gap formation. Other alternatives including increasing the filling fraction and to change the material types to induce a Mie reflection which can also help to strengthen the gaps.

The feasibility study showed various strain cases to test the functionality of ABG materials as sensors. Two levels of induced strain were tested for various scenarios

of strain distributions including localized tensile non-uniform strain, non-localized non-uniform strain, transverse tensile non-uniform strain, tensile uniform strain and compressive uniform strain. Induced strain was considered occurring at the beginning of the sensor as well as at the end for comparison. It was shown that the level of gap deterioration is significantly affected by the non-uniformity in lattice disruption due to non-uniform strain (localized and non-localized). The non-localized cases tended to show more severe deterioration of the gap profile per strain level. Front-end strain and back-end strain gave surprisingly similar gap deterioration profiles, although back-end strain cases show a bit higher sensitivity than the front-end. The transverse non-uniform tensile case clearly showed deterioration as wave propagation was permitted through the open space when the lattice constant was separated along one row. Finally, the uniform strain cases performed as expected with small shifts downward in frequency for tension cases as the lattice constant was increased, and upward in frequency as the lattice constant increased. This was in line with theory as the lattice constant is scalable.

The use of ABG materials as sensors for specifically monitoring known damage on critical components has potential in the SHM realm and it has been shown that such sensors can be produced at small scales with scalable potential and amplified strain capability. As SHM is gaining momentum and condition-based monitoring becomes the norm, ABG sensors can fill in the voids for sensing demands for high sensitivity. ABG sensing also offers differentiation between non-uniform and uniformly strained instances, which has a definite role in the prognosis of damage. Further research is warranted before ABG can be used in field application.

This line of research can be continued in three recommended areas. Experimental evidence of gap formation at the nano-scale, which has already been shown in the literature, needs to include strain cases with gap deterioration tracking. The key efforts here will be in transmission of signal and material selection. Next, the prac-

ticality of use as sensors should be considered based on energy and data processing requirements and cost of production. In preparing for use in the field, the benefits will need to be clearly understood, therefore specific applications need to be considered along with attention to possible setbacks in its function to find its place within the workings of SHM and provide reliability, which is the backbone that makes SHM the advantageous and economic choice.

Appendix A

A1: Benchmark 1 ANSYS logfile

```
/config,NRES,5000

/PREP7
!/INPUT,INPUTad,txt

a=.02 !20 microns
d=.016
c= 0 !3e-3
WI = 2.5*a
WO = 3.0*a
HI = 2.5*a
HO = 3.0*a

numsteps=250

!R1=2.5*a*2

!CYL4,0,0,R1

RECTNG,-WO,WO,-HO,HO,
RECTNG,-WI,WI,-HI,HI,
ASBA,       1,       2

k,9,2.5*a+3*e,0

A,5,8,7,9,6

CYL4,-2*a-2*e,-2*a-2*f,d/2
CYL4,-a-e,-2*a-2*f,d/2
CYL4,0,-2*a-2*f,d/2
CYL4,a+e,-2*a-2*f,d/2
CYL4,2*a+2*e,-2*a-2*f,d/2

CYL4,-2*a-2*e,-1*a-f,d/2
CYL4,-a-e,-1*a-f,d/2
CYL4,0,-1*a-f,d/2
CYL4,a+e,-1*a-f,d/2
CYL4,2*a+2*e,-1*a-f,d/2

CYL4,-2*a-2*e,0,d/2
CYL4,-a-e,0,d/2
CYL4,0,0,d/2
CYL4,a+e,0,d/2
CYL4,2*a+2*e,0,d/2

CYL4,-2*a-2*e,a+f,d/2
CYL4,-a-e,a+f,d/2
CYL4,0,a+f,d/2
CYL4,a+e,a+f,d/2
CYL4,2*a+2*e,a+f,d/2

CYL4,-2*a-2*e,2*a+2*f,d/2
CYL4,-a-e,2*a+2*f,d/2
CYL4,0,2*a+2*f,d/2
CYL4,a+e,2*a+2*f,d/2
CYL4,2*a+2*e,2*a+2*f,d/2

FLST,3,25,5,ORDE,3
FITEM,3,2
FITEM,3,4
FITEM,3,-27
ASBA,       1,P51X

CYL4,-2*a,-2*a,d/2
CYL4,-a,-2*a,d/2
CYL4,0,-2*a,d/2
CYL4,a,-2*a,d/2
CYL4,2*a+e,-2*a,d/2

CYL4,-2*a,-1*a,d/2
CYL4,-a,-1*a,d/2
CYL4,0,-1*a,d/2
CYL4,a,-1*a,d/2
CYL4,2*a+e,-1*a,d/2

CYL4,-2*a,0,d/2
CYL4,-a,0,d/2
CYL4,0,0,d/2
CYL4,a,0,d/2
CYL4,2*a+e,0,d/2

CYL4,-2*a,a,d/2
CYL4,-a,a,d/2
CYL4,0,a,d/2
CYL4,a,a,d/2
CYL4,2*a+e,a,d/2

CYL4,-2*a,2*a,d/2
CYL4,-a,2*a,d/2
CYL4,0,2*a,d/2
CYL4,a,2*a,d/2
CYL4,2*a+e,2*a,d/2

RECTNG,-WO-c,-WO,-HO,HO,
RECTNG,-WO-2*c,-WO-c,-HO,HO,
RECTNG,WO,WO+c,-HO,HO,
RECTNG,WO+c,WO+2*c,-HO,HO,

RECTNG,-WO,WO,-HO-c,-HO,
RECTNG,-WO,WO,-HO-2*c,-HO-c,
RECTNG,-WO,WO,HO,HO+c,
RECTNG,-WO,WO,HO+c,HO+2*c,


ET,1,PLANE82
!*
KEYOPT,1,1,0
```

```
KEYOPT,1,2,0
KEYOPT,1,3,0
KEYOPT,1,5,0
KEYOPT,1,6,0
!*
!ET,2,FLUID29
!*
!KEYOPT,2,2,0
!KEYOPT,2,3,0
!*
!ET,3,FLUID129
!*
!KEYOPT,3,3,0

aglue, all

MPTEMP,,,,,,,,
MPTEMP,1,0
MPDATA,EX,1,,73e9
MPDATA,PRXY,1,,.34
MPTEMP,,,,,,,,
MPTEMP,1,0
MPDATA,DENS,1,,2799
MPTEMP,,,,,,,,
MPTEMP,1,0
MPDATA,EX,2,,4.4e9
MPDATA,PRXY,2,,.37
MPTEMP,,,,,,,,
MPTEMP,1,0
MPDATA,DENS,2,,1142
MPTEMP,,,,,,,,
MPTEMP,1,0
MPDATA,DMPR,2,,0.02
MPTEMP,,,,,,,,
MPTEMP,1,0
MPDATA,EX,3,,4.4e9
MPDATA,PRXY,3,,.37
MPTEMP,,,,,,,,
MPTEMP,1,0
MPDATA,DENS,3,,1142
MPTEMP,,,,,,,,
MPTEMP,1,0
MPDATA,DMPR,3,,0.7
MPTEMP,,,,,,,,
MPTEMP,1,0
MPDATA,EX,4,,3.3e9
MPDATA,PRXY,4,,.37
MPTEMP,,,,,,,,
MPTEMP,1,0
MPDATA,DENS,4,,1142
MPTEMP,,,,,,,,
MPTEMP,1,0
MPDATA,DMPR,4,,0.7



!MPTEMP,,,,,,,,
!MPTEMP,1,0
!MPDATA,MU,3,,100

!MPTEMP,,,,,,,,
!MPTEMP,1,0
!MPDATA,DMPR,2,,1e-1
!MPTEMP,,,,,,,,
!MPTEMP,1,0
!MPDATA,DAMP,2,,1e-6



FLST,5,25,5,ORDE,4
FITEM,5,1
FITEM,5,-2
FITEM,5,4
FITEM,5,-26
CM,_Y,AREA
ASEL, , , ,P51X
CM,_Y1,AREA
CMSEL,S,_Y
!*
CMSEL,S,_Y1
AATT,       1, ,   1,       0,
CMSEL,S,_Y
CMDELE,_Y
CMDELE,_Y1
!*
FLST,5,2,5,ORDE,2
FITEM,5,44
FITEM,5,-45
CM,_Y,AREA
ASEL, , , ,P51X
CM,_Y1,AREA
CMSEL,S,_Y
!*
CMSEL,S,_Y1
AATT,       2, ,   1,       0,
CMSEL,S,_Y
CMDELE,_Y
CMDELE,_Y1
!*
FLST,5,4,5,ORDE,2
FITEM,5,36
FITEM,5,-39
CM,_Y,AREA
ASEL, , , ,P51X
CM,_Y1,AREA
CMSEL,S,_Y
!*
CMSEL,S,_Y1
AATT,       3, ,   1,       0,
CMSEL,S,_Y
CMDELE,_Y
CMDELE,_Y1
!*
FLST,5,4,5,ORDE,2
FITEM,5,40
FITEM,5,-43
CM,_Y,AREA
ASEL, , , ,P51X
CM,_Y1,AREA
CMSEL,S,_Y
!*
CMSEL,S,_Y1
AATT,       4, ,   1,       0,
CMSEL,S,_Y
CMDELE,_Y
CMDELE,_Y1
!*
SMRT,6
SMRT,5
SMRT,4
SMRT,3
SMRT,2
SMRT,1

MSHAPE,0,2D
MSHKEY,0
!*
FLST,5,35,5,ORDE,6
FITEM,5,1
FITEM,5,-2
FITEM,5,4
FITEM,5,-26
FITEM,5,36
FITEM,5,-45
CM,_Y,AREA
ASEL, , , ,P51X
CM,_Y1,AREA
CHKMSH,'AREA'
CMSEL,S,_Y
!*
AMESH,_Y1
!*
CMDELE,_Y
CMDELE,_Y1
CMDELE,_Y2
!*

!Absorbing Boundary
!FLST,5,4,4,ORDE,2
!FITEM,5,1
!FITEM,5,-4
!LSEL,S, , ,P51X
!NSLL,S,1
!/REPLOT
!NPLOT
!NSLL,S,1
!TYPE,   3
!MAT,       1
!REAL,
!ESYS,       0
!SECNUM,
!*
!R,1, ,,,
!*
!ESURF
```

```
ALLSEL,ALL

!Fluid-Solid Boundary
!FLST,5,4,4,ORDE,2
!FITEM,5,9
!FITEM,5,-12
!LSEL,S, , ,P51X
!NSLL,S,1
!/REPLOT
!NPLOT
!NSLL,S,1
!sf,all,fsi
!ALLSEL,ALL
!APLOT
FINISH
/SOL
!!*
ANTYPE,3
!*
!*
HROPT,FULL
HROUT,ON
LUMPM,0
!*
EQSLV,ICCG,1e-008,
PSTRES,0
!*
FINISH
/PREP7
FLST,2,1,4,ORDE,1
FITEM,2,8
!*
/GO
DL,P51X, ,UX,1e-6,
FINISH
/SOL
HARFRQ,0,500e3,
NSUBST,numsteps,
KBC,1
!*
!ALPHAD,100000,
!BETAD,0,
!DMPRAT,0,
!*

FINISH
/PREP7
R,1,R1,0,0,
!*

FINISH
/SOL
/STATUS,SOLU
SOLVE

/POST1
*GET,STEPS,ACTIVE,0,SET,NSET
*DIM,NODE_RES,ARRAY,numsteps,1

FINISH
/POST26
/UI,COLL,1
NUMVAR,200
SOLU,191,NCMIT
STORE,MERGE
PLCPLX,0
PRCPLX,1
FILLDATA,191,,,,1,1
REALVAR,191,191
NUMVAR,200
PLCPLX,0
PRCPLX,1
FILLDATA,191,,,,1,1
REALVAR,191,191
!*
NSOL,2,9,U,X, UX_3
STORE,MERGE

vget,NODE_RES(1),2

*cfopen,amplitude4,txt,,
*vwrite, Node_Res(1)
(E12.5)
*cfclos
```

References

[1] Adams D. E. *Health Monitoring of Structural Materials and Components*. John Wiley & Sons Ltd., West Sussez PO19 8SQ, England, 2007.

[2] Scott M., Bannister M., Herszberg I., Li H., and Thomson R. Structural health monitoring-the future of advances composite structures. In *Proceedings of the 5th International Workshop on Structural Health Monitoring*, Keynote Presentations, pages 107–121, Stanford University, CA, USA, September 12-14, 2005.

[3] Sekhar B.V.S., Balasubramaniam K., and Krishnamurthy C.V. Structural health monitoring of fiber-reinforced composite plates for low-velocity impact damage using ultrasonic lamb wave tomography. *Structural Health Monitoring*, 39(5):243–253, 1991.

[4] Speckmann H. and Henrich R. Structural health monitoring (shm) -overview on technologies under developement. In *16th World Conference on NDT*, pages 326–332, Montreal, CA.

[5] Balageas (Editor) D. L. *Structural Health Monitoring*. Wiley, 2006.

[6] Marwala T. Damage identification using committee of neural networks. *Journal of Engineering Mechanics*, 129(1):43–50, 2000.

[7] Bar-Cohen Y. Nde of fiber reinforced composite materials a review. *Materials Evaluation*, 44(4):446–454, 1986.

[8] Derriso M. M., Olson S.E., DeSimio M. P., and Pratt D. M. In *Structural Health Monitoring*, pages 44–55, Stanford, CA, USA, September 11-13, 2007 2007.

[9] Kessler S. S. *Piezoelectric-Based In-Situ Damage Detection of Composite Materials for Structural Health Monitoring Systems*. Dissertation, Massachusetts Institute of Technology (MIT), Cambridge, MA, USA, 2002.

[10] Gros X.E., Ogi K., and Takahashi K. Eddy current, ultrasonic c-scan and scanning acoustic microscopy testing of delaminated quasi-isotropic cfrp materials. *Journal of Reinforced Plastics and Composites*, 17(5):389–405, 2004.

[11] Chang F. K. Forward. In *Structural Health Monitoring*, Forward, pages 1–27, Stanford, CA, USA, September 8-10, 1999.

[12] Chang F. K. A report on the first international workshop on structural health monitoring. In *Structural Health Monitoring*, pages 1–27, Stanford, CA, USA, September 8-10, 1999.

[13] Beard S. J., Kumar A., Qing P., Hannum R., and Ikegami. Hot-spot fatigue crack monitoring of inaccessible structural regions in aircraft subsystems using structural health monitoring. In *9th Joint FAA/DOD/NASA Conference on Aging Aircraft*, NDI - NDI For Crack Detection II, page NA, Atlanta, GA, USA, March 6-9, 2006 2006.

[14] Callister W. D. Jr. *Materials Science and Engineering An Introduction*. John Wiley & Sons Inc., 111 River Street, Hoboken, NJ 07030, 2003.

[15] Rakow J. F. and Pettinger A. M. Failure analysis of composite structures in aircraft accidents. In *ISASI 2006 Annual Air Safety Seminar*, pages 1–27, Cancun, Mexico, September 11-14, 2006.

[16] Baker A., Dutton S., and Kelly (ed) D. *Composite Materials for Aircraft Structures*. American Institute for Aeronautics, 2004.

[17] Atodaria D.R., Putantunda S.S, and Mallick P.K. Delamination growth behavior of a fabric reinforced laminated composite. *Journal of Engineering Materials and Technology*, 121(3):381–385, 1999.

[18] Doubling S.W., Ferrar C.R., and Prime M.B. A summary review of vibration-based damage identification methods. *The Shock and Vibration Digest*, 30(2):91–105, 1998.

[19] Ganga-Rao (Editor) H. V. S. *Nondestructive Testing Methods for Civil Infrastructure*. ASCE Publications, Reston, USA, 1995.

[20] Prosser W.H. Advanced ae techniques in composite material research. *Journal of Acoustic Emission*, 14(3-4):S1–S11, 1996.

[21] Okafor A. C., K. Chandrashekhara, and Y. P. Jiang. In *SPIE Proceedings*, 2718, pages 291–302, 1996.

[22] Zhou G. and Sim L. M. Damage detection and assesment in fibre-reinforced composite structures with embedded fibre optic sensors-review. *Smart Materials and Structures*, 11(6):925–939, 2002.

[23] Liang Y. and Ansari C. Sun, F. Acoustic emission characterization of damage in hybrid fiber-reinforced polymer rods. *Journal for Composites for Construction*, 8(1):70–78, 2004.

[24] Schoess J. N. and Zook J. D. In *SPIE Conference on Smart Electronics and MEMS*, pages 326–332. SPIE, 1998.

[25] Yuan F. G. and Wang L. Damage identification in a composite plate using prestack reverse-time migration technique. *Structural Health Monitoring*, 4(3):195–211, 2005.

[26] Kushwaha M.S., Halevi P., Dobrzynski L., and Djafari-Rouhani B. Acoustic band structure of periodic elastic composites. *Physical Review Letters*, 71(13):2022–2025, September 1993.

[27] Yablonovitch E. Inhibited spontaneous emission in solid-state physics and electronics. *Physical Review Letters*, 58(20):2059–2062, May 1987.

[28] Brillouin. *Wave Propagation in Periodic Structures*. American Institute for Aeronautics, 1946.

[29] Miyashita T. Sonic crystals and sonic wave-guides. *Measurement Science and Technology*, 16:R47–R63, 2005.

[30] Sigalas M.M. and Economou E.N. Elastic waves in plates with periodically placed inclusions. *Journal of Applied Physics*, 75(6):2845–2850, March 1994.

[31] Kushwaha M.S. and Djarfari-Rouhani B. Complete acoustic stop bands for cubic arrays of spherical liquid balloons. *Journal of Applied Physics*, 80(6):3191–3195, September 1996.

[32] Kushwaha M.S. and Halevi P. Band-gap engineering in periodic composites. *Applied Physics Letters*, 64(9):1085–1087, February 1994.

[33] Sigalas M.M. Defect states of acoustic waves in a two-dimensional lattice of solid cylinders. *Journal of Applied Physics*, 84(6):3026–3029, September 1998.

[34] Kafesaki M., Sigalas M.M., and Garcia N. Frequency modulation in the transmittivity of wave guides in elastic-wave band-gap materials. *Physical Review Letters*, 85(19):4044–4047, November 2000.

[35] Shen M. and Cao W. Acoustic band-gap engineering using finite-size layered strucures of multiple periodicity. *Applied Physics Letters*, 75(23):3713–3715, December 1999.

[36] National and Kapodistrian University of Athens. Publications on phononic crystals and directly related areas of physics. Online, 2008 March.

[37] James R., Woodley S.M., Dyer C.M., and Humphrey V.F. Sonic bands, bandgaps, and defect states in layered structures-theory and experiment. *Journal of the Acoustic Society of America*, 97(4):2041–2047, April 1995.

[38] Montero de Espinosa F. R., Jimenez E., and Torres M. Ultrasonic band gap in periodic two-dimensional composite. *Physical Review Letters*, 80(6):1208–1211, February 1998.

[39] Vasseur J. O., Deymier P.A., Frantziskonis G., G. Hong, Djafari-Rouhani B., and Dobryznski L. Experimental evidence for the existence of absolute acoustic band gaps in two-dimensional periodic composite media. *Journal of Physics: Condensed Matter*, 10:6051–6064, 1998.

[40] Robertson W.M. and Rudy J.F. Measurement of acoustic stop bands in two-dimensional periodic scattering arrays. *Journal of the Acoustic Society of America*, 104(2):694–699, August 1998.

[41] Sanchez-Perez J.V., Caballero D., Martinez-Sala R., Rubio C., Sanchez-Dehesa J., Meseguer F., Llinares J., and F. F., Galvez. Sound attenuation by a two-dimensional array of rigid cylinders. *Physical Review Letters*, 80(24):5325–5328, June 1998.

[42] Rubio C., Caballero D., Sanchez-Perez J.V., Martinez-Sala R., Sanchez-Dehesa J., Meseguer F., and Cervera F. The existence of full gaps and deaf bands in two-dimensional sonic crystals. *Journal of Lightwave Technology*, 17(11):2202–2207, November 1999.

[43] C. Miyashita, T. Inoue. Numerical investigations of transmission and waveguide properties of sonic crystals by finite-difference time-domain method. *Japan Journal of Applied Physics*, 40:3488–3492, 2001.

[44] Miyashita T., Tangiguchi R., and Sakamoto H. Experimental full band-gap of a sonic crystals slab made of a 2d lattice of aliminum rods in air. In *WCU Proceedings 2003*, Paris, 2003, September 7-10 2003. WCU.

[45] Kushwaha M. Stop-bands for periodic mettalic rods: Scultures that can filter noise. *Applied Physics Letters*, 70(24):3218–3220, June 1997.

[46] Kushwaha M.S. and Djafari-Rouhani B. Sonic stop-bands for periodic arrays of metallic rods: Honeycomb structure. *Journal of Sound and Vibration*, 218(4):697–709, 1998.

[47] Sigalas M.M. and Economou E.N. Band structure of elastic waves in two dimensional systems. *Solid State Communications*, 186(3):141–143, 1993.

[48] Goffaux C. and Sanchez-Dehesa J. Two-dimensional phononic crystals studied using a variational method: Application to lattices of locally resonant materials. *Physical Review B*, 67(14):1–10, 2003.

[49] Liu Z., Zhang X., Mao Y., Zhu Y.Y., Yang Z., Chan C.T., and Sheng P. Locally resonant sonic materials. *Science Magazine*, 289:1734–1736, September 2000.

[50] Garcia-Pablos D., Sigalas M.M., Montero de Espinosa F.R., Torres M., Kafesaki M., and Garcia N. Theory and experiments on elastic band gap. *Physical Review Letters*, 84(19):4349–4352, May 2000.

[51] Vasseur J. O., Deymier P.A., Khelif A., Lambin Ph., Djafari-Rouhani B., Akjouj A., Dobryznski L., Fettouhi N., and Zemmouri J. Phononic crystal with low filling fraction and absolute acoustic band gap in the audible frequency range: A theoretical and experimental study. *Physical Review Letters*, 65(5):1–6, 2002.

[52] Sigalas M.M. and Garcia N. Importance of coupling between longitundinal and transverse components for the creation of acoustic band gaps: The aluminum in mercury case. *Applied Physics Letters*, 76(16):2307–2309, April 2000.

[53] Miyashita T. Numerical studies on band-gap structures and resonant-mode wave-guides of typical sonic crystals made of rigid cylinders in fluid by means of elastic fdtd method. In *Proceedings of 2005 ASME-IMECE: ASME 2005 Mechanical Engineering Congress and Exposition*, Orlando Fl, USA, November 5-11, 2005 2005.

[54] Tanaka Y., Tomoyasu T., and Tamura S. Band structure of acoustic waves in phononic lattices: Two-dimensional composites with large acoustic mismatch. *Physical Review B*, 62(11):7387–7392, September 2000.

[55] Miyashita T. Full band gaps of sonic crystals made of acryllic cylinders in air -numerical and experimental investigations-. *Japan Journal of Applied Physics*, 41:3170–3175, 2002.

[56] Caballero D., Sanchez-Dehesa J., Rubio C., Martinez-Sala R., Sanchez-Perez J.V., Meseguer F., and Llinares J. Large two-dimension sonic gaps. *Physical Review E*, 60(6):R6316–R6319, December 1999.

[57] Joannopoulos J.D., Meade R.D., and Winn J.N. *Photonic Crystals: molding the flow of light*. Princeton University Press, 41 William Street, Princeton, New Jersey 08540, 1995.

[58] Kushwaha M.S., Halevi P., and Martinez G. Theory of acoustic band structure of periodic elastic composites. *Physical Review B*, 49(4):2313–2322, January 1994.

[59] Kafesaki M., Sigalas M.M., and Economou E.N. Elastic wave band gaps in 3-d periodic polymer matrix composites. *Solid State Communications*, 96(5):285–289, 1995.

[60] Kee C., Kim J., Park H.Y., and Chang K.J. Essential role of impedance in the formation of acoustic band gaps. *Journal of Applied Physics*, 87(4):1593–1596, February 2000.

[61] Sigalas M.M. and Economou E.N. Elastic and acoustic wave band structures. *Journal of Sound and Vibration*, 158(2):377–382, 1992.

[62] Goffaux C. and Vigneron J.P. Theoretical study of tunable phononic band gap system. *Physical Review B*, 64(7):1–5, 2001.

[63] Jensen J.S. and Sigmund O. Phononic band gap structures as optimal designs. *Proceedings of the IUTAM Symposium on Asymptotics, Singularities, and Homohenisation in Problems of Mechanics*, pages 73–83, 2003.

[64] Psarobas I.E. and Stefano N. Phononic crystals with planar defects. *Physical Review B*, 62(9):5536–5540, September 2000.

[65] Martinez-Sala R., Sancho J., Sanchez J.V., Gomez V., Llinares V., and Meseguer J.F. Sound attenuation by sculpture. *Nature*, 378:241, November 1995.

[66] Dhar L. and Rogers J.A. High frequency one-dimensional phononic crystal characterized with a picosecond transient grating photoacoustic technique. *Applied Physics Letters*, 77(9):1402–1404, August 2000.

[67] Madou M.J. *Fundamentals of Microfabrication The Science of Miniaturization*. CRC Press LLC, Washington DC, 2002.

[68] Ramprasad R. and Shi N. Scalability of phononic crystal heterostructures. *Applied Physics Letters*, 87(11):1–3, 2005.

[69] Zheng Y. Biosensors on surface acoustic wave phononic band gap structures. Reu research accomplishments, NNIN, Georgia Research Institute of Technology, Microelectronics Research Center, 2004.

[70] El-Kady I., Olsson III R.H., and Flemin J.G. Phononic band-gap crystals for rf communications. *Applied Physics Letters*, 92(23), 2007.

[71] Mohammadi S., Eftekhar A.A., Khelif A., Hunt W.D., and Adibi A. Evidence of large high frequency complete phononic band gaps in silicon phononic crystal plates. *Applied Physics Letters*, 92, 2008.

[72] Klironomos A.D. and Economou E.N. Elastic wave band gaps and single scattering. *Solid State Communications*, 105(5):327–332, 1998.

[73] Maldovan M. and Thomas E.L. Simultaneous localization of photons and phonons in two-dimensional periodic structures. *Applied Physics Letters*, 88(25):1–3, 2006.

[74] Olsson III R.H., Fleming J.G., El-Kady I., Tuck M.R., and McCormick F.B. Micromachined bulk wave acoustic bandgap devices. Actuators and Microsystems, 2007.

[75] *Piezoelectric Ceramics: Principles and Applications*. APC Products, Inc., Mackeyville, PA, USA, 2002.

[76] Hewlett-Packard Company, Santa, Rosa CA, USA. *User's Guide: HP 8753 Option 011 Network Analyzer*, 1997.

[77] Logan D.L. *A First Course in the Finite Element Method*. Nelson (Division of Thomson), Toronto, Ontario, CA, 2007.

[78] Axmann W. and Kuchment P. An efficient finite element method for computing spectra of photonic and acoustic band-gap materials. *Journal of Computational Physics*, 150:468–481, 1999.

[79] Imaoka S. Addedum to 'structural damping': Memo number sti0804a. Memo, ANSYS, April 2008. ANSYS Release.

[80] Imaoka S. Tips and tricks: Structural damping: Memo number sti:001021a. Memo, ANSYS, October 2000. ANSYS Release.

[81] Robinson D. Ansys acoutics introductory training. Training material, PADT Inc., August 2009. Training Manual.

[82] Merheb B., Deymier P.A., Jain M., Aloshyna-Lesuffleur M., Mohanty S., Berker A., and Greger R.W. Elastic and viscoelastic effects in rubber/air band gap structures: A theoretical and experimental study. *Journal of Applied Physics*, 104(5):064913–064917, 2008.